7-2-2013

Characterization of the mechanical properties of freestanding platinum thin films

Khawar Abbas

Khawar Abbas
Candidate

Mechanical Engineering Department
Department

This dissertation is approved, and it is acceptable in quality and form for publication:

Approved by the Dissertation Committee:

Dr. Zayd C. Leseman	Committee Chair
Dr. Yu-Lin Shen	Committee Member
Dr. Christopher D. Hall	Committee Member
Dr. Mani Hossein-Zadeh	Committee Member

CHARACTERIZATION OF THE MECHANICAL PROPERTIES OF FREESTANDING PLATINUM THIN FILMS

BY

KHAWAR ABBAS

B.E. Mechanical, National Univ. of Sc. & Tech., 2000
M.S., Mechanical Engineering, University of New Mexico, 2008

DISSERTATION

Submitted in Partial Fulfillment of the
Requirements for the Degree of

Doctor of Philosophy
Engineering

The University of New Mexico
Albuquerque, New Mexico

May, 2013

ACKNOWLEDGEMENTS

This dissertation would not have been possible without the countless contributions of so many people that I came across during my stay at the University of New Mexico. I would like to thank them and let them know that their contribution has not gone unnoticed and I appreciate their help from the bottom of my heart. I am grateful to my research advisor Dr. Zayd C. Leseman. He introduced me to this exciting field of MEMS and Micro-mechanics, provided technical guidance, necessary financial support and overlooked my mistakes. He has been a constant source of inspiration for me and this work would definitely not have been possible without his support, encouragement and suggestions.

It has been a great experience to be a student at UNM and in Dr. Leseman's research group. My friends and colleagues in our research group made my stay very enjoyable and memorable. In particular, I would like to thank my dear friend Drew Goettler for his help, support, friendship and comradeship. He made me feel at home and welcomed me to his home and family. For the past six years we have shared our office space and often times our frustrations after many failed experiments with each other. We regularly bounced ideas off of each other and had insightful discussions that proved very instrumental in the completion of this work. He is also finishing his PhD this semester and I wish him the very best of luck in his future endeavors.

I am thankful for the support provided by Elena Dobrica and Ying-Bing Jiang of Earth and Planetary Sciences Department at UNM. They were extremely helpful and insightful in acquiring some of the analytical microscopy data. Elena was very instrumental in preparing and imaging the TEM lift-out that led to the

discovery of the most exciting results presented in this dissertation. Without her support to this work would have been incomplete.

I would like to extend my special thanks to Dr. Azeem Sarwar who convinced me to return to graduate school and pursue doctoral studies. His encouragement, motivation and subsequent assistance paved the way for me to embark on this endeavor and I appreciate it greatly. My thanks to Kazim Ali Malik, Abrar Manzar and Rafay Zahid Ansari for their moral support and companionship.

I am very grateful to my younger sister Faryal Abbas for shouldering my share of familial obligations towards our parents for last six year. This work would definitely not have been possible had she not stepped forward and filled in my shoes. Last, and most importantly my parents deserve much credit for my success. They raised me in an atmosphere of appreciation of science, for learning and for striving to understand the world around me. I am especially grateful to my mother for her prayers, constant encouragement, unconditional support and genuine love.

I have inevitably missed some people but I would like all of them to know that their help is no less appreciated - “Thanks a lot.”

CHARACTERIZATION OF THE MECHANICAL PROPERTIES OF FREESTANDING PLATINUM THIN FILMS

BY

KHAWAR ABBAS
B.E. Mechanical, National Univ. of Sc. & Tech., Pakistan, 2000
M.S., Mechanical Engineering, University of New Mexico, 2008
PhD, Engineering, University of New Mexico, 2013

ABSTRACT

Many MEMS devices utilize nanocrystalline thin metallic films as mechanical structures, in particular, micro switching devices where these films are used as Ohmic contacts. But the elastic and plastic properties of these thin films (thickness < 1μm) are significantly different from those of the bulk material. At these scales the volume fraction of material defects such as: grain boundaries, dislocations and interstitials become quite significant and become a chief contributor to the physical and mechanical material properties. In order to effectively design MEMS devices it is important that these material properties are explored and mechanical behavior of the structure they form be characterized. Popular thin film materials used in MEMS devices are Aluminum (Al), Copper (Cu), Nickel (Ni) and Gold (Au). Platinum has traditionally gained acceptance into the MEMS industry because of its chemical inertness and high temperature stability. However the mechanical properties of platinum remains the least exploited. Platinum has a high Young's Modulus (164 GPa, for bulk) and high melting temperature (1768 ^{o}C) and therefore can be used as a 'thin film' structure

(cantilever, a bridge or a membrane) in high temperature environments with high resistance to mechanical failure.

The physical size of these thin film structure make it very difficult to handle them and employ traditional mechanical testing methodologies and techniques and therefore require custom test platforms. One such recently developed platform is presented in this dissertation. The test platform is comprised of a microfabricated cascaded thermal actuator system and test specimen. The cascaded thermal actuator system is capable of providing tens of microns of displacement and tens of milli-Newton forces simultaneously while applying a relatively low temperature gradient across the test specimen. The dimensions of the platform make its use possible in both the SEM/TEM environments and on a probe station under an optical microscope. Digital image correlation was used to obtain similar accuracy (~10 nm) for displacement measurements in both an SEM and under an optical microscope.

The mechanical behavior of nanocrystalline thin film structure has been the subject of extensive research in recent years. Mainly, the focus has been on the effects of the film thickness with only a few researchers mentioning anything about the grain sizes of their polycrystalline films. The effect of thin film cross sectional morphology on the mechanical behavior of a thin film structure has never been studied directly. Presented in this dissertation is experimental evidence that these thin film structures are composite structures of various grain morphologies and the overall mechanical behavior exhibited by them is the combined effect of individual contributions of each of these grain morphologies.

Table of Contents

List of Figures

Chapter 1

INTRODUCTION

1.1. Background and Motivation

Advancements in semiconductor fabrication technology, particularly the advancement in bulk and surface micromachining techniques of silicon (Si), during the 1980's and early 1990's opened doors to a new era of miniaturized electro-mechanical structures and devices that are now known as "MEMS (Micro Electro-Mechanical Systems)" [1-5]. These devices offered new capabilities, improved performance and lower cost due to batch production over traditional transducers and sensors. Perhaps the greatest advantage that MEMS had to offer was their ability to be cofabricated, compatibly, with an integrated circuit (IC) thereby reducing the overall size and power requirements of a complete mechanical system to that of a mere electronic IC chip. Since then, this field of science has transformed into an industry of its own which perhaps one day will be as great as its parent semiconductor industry. There are now numerous MEMS devices that are commercially available and are being used in our daily lives. They are being used in many physical, chemical and biological applications. A number of these applications make use of the mechanical properties of thin metal films. In particular, micro switching devices where these films are used as an ohmic contact material.

Platinum has traditionally gained acceptance into the MEMS industry because of its chemical inertness and high temperature stability [6]. More recently, its use

as an ohmic contact has started to increase and several studies into its electrical properties have been performed [7-10]. However the mechanical properties of platinum remains the least exploited. Platinum has a high Young's Modulus (164 GPa, for bulk) and high melting temperature (1768 ^{o}C) and therefore can be used as a 'thin film' structure (cantilever, a bridge or a membrane) in high temperature environments with high resistance to mechanical failure. Ekkels et al. [11] successfully demonstrated the use of these properties by using platinum as a structural material in RF micro switches. High melting temperature, chemical inertness and stability also makes it an ideal candidate for post processing steps such as zero-level packaging.

Nano-structured thin films (typical grain size <100nm) exhibit elastic and plastic properties that are significantly different from those of the bulk material [12-14]. At these scales the volume fraction of material defects such as: grain boundaries, dislocations and interstitials become quite significant and become a chief contributor to the physical and mechanical material properties of the thin films. Thin films generally exhibit higher strength than the material in the bulk form with reduced ductility. Their tendency towards a more brittle behavior increases as the thickness of the film diminishes and grain size reduces [15-19]. Most of these studies have been conducted on metals like Al, Au, Cu and Ni, the metals that are commonly used in electronic components. The material properties of platinum at this scale, however, have not been very extensively studied. The studies that are available [20, 21] suggest that even for an ultra fine

grain size of 25 nm platinum exhibits very large plasticity and its dependence on the strain rate [20]. This is very intriguing and raises the following questions:

- Does platinum exhibit different behavior than what is observed in other in FCC metals?
- What is the transition grain size for platinum below which plasticity is not observed?
- Is there such a transition grain size range?

Material properties and morphology of thin films is also dependent on their fabrication process. For physical vapor deposited films they depend greatly on the ratio T/T_m, where T is the substrate temperature and T_m is the melting temperature of the material [22]. For platinum, which has a very high melting temperature (higher than Al, Cu, Au and Ni), deposited at temperatures close to room temperature; T/T_m remains very low for many processing routes. Low T/T_m implies that less energy is available for activation of self and bulk diffusion. This is hypothesized to result into arrested grain growth. Does this mechanism provide opportunity to isolate the effects of film thickness and grain size individually? To answer these questions further a study is required that specifically seeks to address these behaviors.

In summary, this dissertation is the author's attempt to perform a study on the mechanical properties of thin platinum films of varying grain size. The motivation for this is the potential for increased use of platinum in commercial MEMS devices as a structural material and lack of existing studies that

characterize the mechanical properties of nano-structured platinum. Nano-structured grains with dimension less than 100 nm are expected to show unique behaviors not seen in bulk Pt and possibly properties that have not been seen in other nano-structured metals.

1.2. Relationship to prior work

The material properties of nanostructured materials in general, and thin metal films in particular, are a subject of ongoing research. Even though it is sometimes debatable as to what behavior is the true specimen behavior and not an artifact of the specimen fabrication procedure or test methodology, polycrystalline FCC thin metal films are known to exhibit certain property trends with reduced grain size / film thickness. The said trends include: higher than bulk yield strength, reduced plasticity, plastic strain and creep recovery.

Material properties of thin films depend separately on the grain size film thickness and crystallographic texture [23, 24]. Isolating the film behavior with the change of each of these parameters remains difficult. Higher than bulk yield strength with decreasing film thickness was reported on films attached to the substrates by Artz and Spaepen [17-19]. However in order to remove any doubts about the influence of the substrate on the film properties author's preference remains with the testing of free standing films. Experiments for characterization of the material properties on free standing films are limited [12, 15, 25, 26] Haque and Saif [26, 27] pioneered the use MEMS actuators for in-situ in SEM/TEM materials testing. They reported nonlinear elasticity with lower elastic modulus, lack of work hardening, and brittle failure for free standing polycrystalline Au and

Al films of thicknesses <100 nm [26]. Samuel and Haque [28] then noticed the relaxation of freestanding nano-crystalline Au films at room temperature and used an analytical model based on a spring and a dashpot to predict an instantaneous Young's modulus. They also determined the effect of size in nano scale solids by comparing the relaxation time at room temperature with that of bulk solids. However in their experiments the grain size also varied with the film thickness and interpretation of the results by isolating the behavior of size effect from the well-known Hall-Petch effect remains difficult.

Espinosa and co workers [15, 16] tested much thicker films of Au, Cu and Al (200 nm - 1 μm) by use of a membrane deflection experiment (MDE). The average grain size in their work was maintained constant at 200 nm and was independent of the film thickness. They reported a substantial size effect on the yield stress. They noticed the effect of both the film thickness and specimen width, with film thickness having greater influence. Their observation of decreasing ductility with decreasing film thickness was consistent with that of Haque et al. However, contrary to Haque's work Espinosa did not report any variation in the elastic modulus with the decreasing film thickness. In the case of Au however, they noticed a major change in the inelastic response as the film thickness was reduced from 1 μm to 300 nm. SEM and TEM analysis of the films conducted postmortem revealed the existence of deformation bands in the thicker films whereas none were found in thinner films.

In addition to the dependence of the onset of plasticity on the film thickness, the existence of plasticity in these nanostructured films is also very

intriguing to researchers. In bulk materials permanent deformation is attributed to the motion and nucleation of the dislocations across the grains; and the grain boundaries are known to create resistance to this dislocation movement. Nanostructured films however, have a relatively higher fraction of grain boundaries and therefore present very high resistance to plasticity. And dislocation motion and nucleation alone cannot completely explain the amount of plastic deformation seen at this scale. Various experimental and dislocation dynamics simulation studies [26, 29] have been conducted to explain the reasons for the plastic behavior and size effects of the nano structured films. It is believed that the permanent deformation in nano-crystalline materials in addition to dislocation motion, interaction storage and annihilation is also grain boundary mediated caused by the grain boundary sliding or grain rotation [30-32]. Other mechanisms and the effects of film thickness and grain size on various mechanisms and their contribution to the overall plasticity are a topic of ongoing research. The existence of more than one dominant mechanism for deformation and the individual and competing effect of these mechanisms are manifested in the form of material properties of these films. It is because of this that nanostructured films are known to recover partially from plastic strains and creep [33-37], and display the Bauschinger effect in unpassivated films [38].

Figure 1.1 presents the relationship between the grain size and film thicknesses for the nanocrystalline gold (Au) thin films reported in the literature. Since there is not much information available in the literature on Pt the data for Au is presented in Figure 1.1. Au is a noble FCC metal and is expected to exhibit

properties similar to that of the Pt. It is noteworthy that while for thin film specimens with thicknesses >400nm (labeled as Region 'B'), the consistency in grain size makes it possible to isolate the effect of film thickness from that of the grain size; this is not possible for specimens with thicknesses <400nm (labeled as Region 'A'). This lack of certainty in correlating the material properties to the grain size and film thickness makes this region the region of interest. Also plotting the available information on Pt on the same plot it is seen that even though an ultra fine grain size of ~25 nm at film thickness of 400nm puts it close to Region 'A'; the mechanical behavior exhibited by it is consistent with Region 'B' [20].

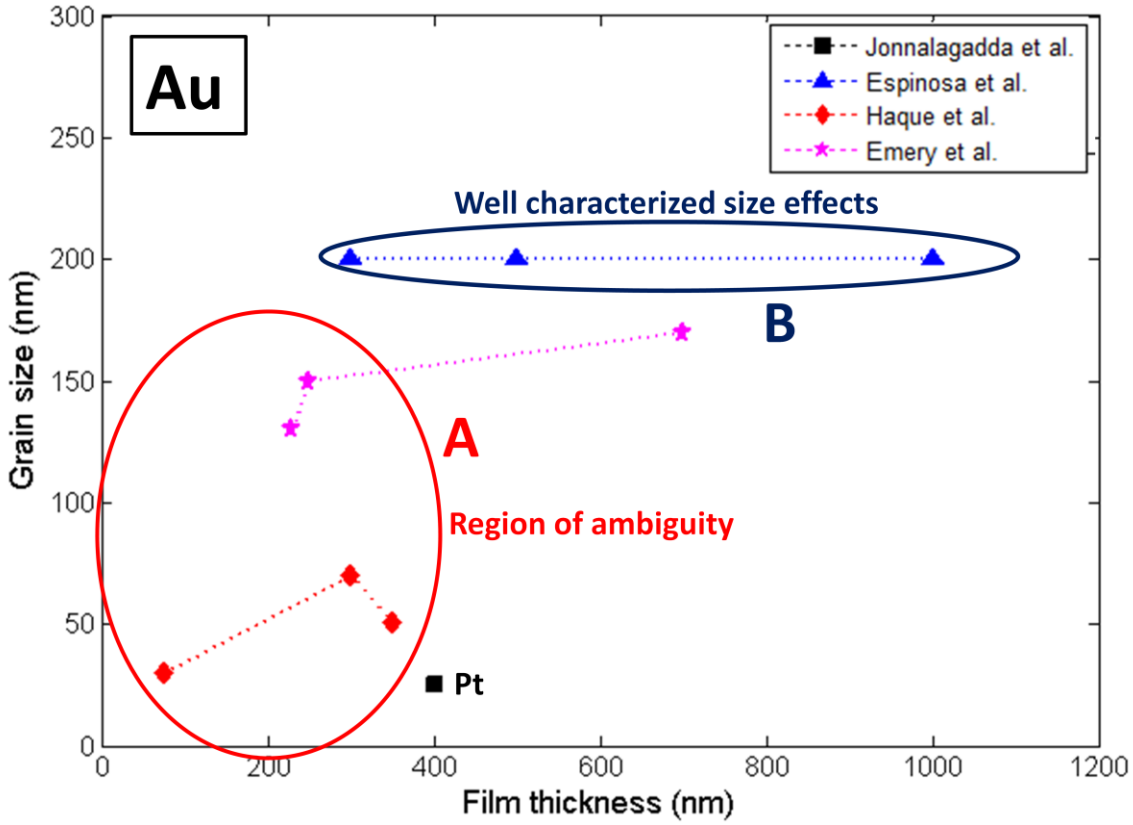

Figure 1.1: Relationship between grain size and film thickness for nanocrystalline Au thin film specimens from literature

In this study the author attempts to characterize platinum, another FCC metal that has not been studied in detail before. The aim is to compare and contrast its mechanical behavior to the mechanical behavior of other thin film materials reported in the literature. Attempts were also made to explore and investigate both experimentally and analytically to answer the ambiguity raised by Figure 1.1.

1.3. Scope and deliverables

Since this study is being performed from the view point of MEMS devices where the films are used as the structural material for switches in a membrane geometry, the scope of this study is restricted to the study of free standing thin films only. Tensile testing is a traditional and simplest method for materials testing that provides stress-strain relationship directly; for this reason it remains author's preferred choice of testing mechanism. There are no standard testing platforms for testing free standing films at this scale. Keller et al. [25], Espinosa [15, 39], Haque [27] and Chasiotis [40] all have developed custom test platforms for characterization of thin film. Therefore, the author's choice for the scope for this study is as follows:

a. Design, fabrication and characterization of a test platform that can be used perform tensile stress on a free standing thin film metal specimen. The platform should be able to provide sufficiently large displacements so as to facilitate in situ testing both in a SEM and with an optical microscope on probe station. Tests under both environments are important. Testing under an optical microscope on a probe station provides ease of setup and facilitates testing in

comparatively less time than SEM. SEM however facilitates the viewing and imaging of any morphological or surface activity on the test specimen during and after the test

b. Write a custom MATLAB script for digital image correlation and tracking of the gathered image sequence and its translation into specimen stress and strain

c. Write a custom MATLAB script to control a programmable DC power supply in order to drive the MEMS based actuator platform and conduct experiments at various strain rates if required

d. Test platinum thin films specimens of various thicknesses and find transition of platinum behavior between ductile to brittle

e. Test thin film specimens of various thicknesses with special emphasis to characterize their mechanical properties and investigate the underlying mechanisms at play.

1.4. Overview / Organization

This dissertation is divided into six chapters. The second chapter presents the research methodology for characterizing the mechanical properties of free standing Pt thin films by use of cascaded thermal MEMS actuators used in this study. It also provides the mechanics behind the operation of cascaded thermal actuators; some of the common design rules and constraints; as well as its comparison to traditional thermal actuators. Chapter three provides a detailed explanation of the fabrication process to co-fabricate free standing thin Pt films with thermal actuators used in this study. Chapter four describes the

experimental setup and procedure used to test and characterize both the fabricated devices and the Pt thin film specimens. Chapter five of this dissertation presents the experimental results and discussion of the mechanical properties of Pt thin film specimens and their dependence on the thin film's cross sectional morphology. Chapter six is the last chapter of this dissertation and presents the conclusion and areas for future work.

Chapter 2

RESEARCH METHODOLOGY

In recent years, several studies have emerged subjecting nano-scale materials to tensile loading utilizing either ‘off-chip’ actuators [20, 41-44] or ‘on-chip’ MEMS actuators [27, 45-47]. They operate in different size and scale ranges. Off-chip actuators are used to test specimen thicknesses of 400 nm to 1 μm whereas on-chip actuators have been used to test specimens in 75 nm to 125 nm thickness range. Off-chip actuators are generally piezo actuators and form test platforms where the force applying actuators are separate to the test specimen. Such test platforms provide the advantage of being easier to setup because of their size and experiments are generally performed under an optical microscope. Also, since the specimen is independent of the actuators they offer a choice of wide range of specimen materials. The choice of specimen materials is limited for the on-chip actuators because the specimens are either co-fabricated along with the actuator [27, 47] or mounted later by the use of probe and focused ion beam (FIB) [45, 46]. On-chip actuators however provide the huge benefits of precise sample alignment as well as high load and displacement resolutions.

Two types of MEMS actuators are used for on-chip tensile testing of nanoscale films, comb drive actuators and chevron type thermal actuators. Thermal actuators have been demonstrated to be robust and capable of providing far greater force and displacement than the comb drive actuators. However, the large thermal gradient required to produce these forces and displacements have limited their utilization potential. Test platforms used for

material testing should not have large temperature gradients across them, since this temperature gradient may alter the materials response to mechanical stimuli. For example, it may alter the stiffness of the test specimen. In order to avoid large temperature gradients across the thermal actuators used for materials testing other researchers [48, 49] have restricted their use to very small displacements. This displacement restriction limits their use to a scanning electron microscope only where very small displacements can be measured with greater accuracy.

For this study the author has developed a test platform that utilizes and combines the techniques developed separately for both in-situ and ex-situ SEM studies along with the displacement amplification technique originally developed for strain gauges to measure stresses induced in wafers and films due to curvature. This platform provides very large force and displacement with comparably small temperature rise and therefore can be used for studies over the entire range (75nm-1μm) of specimen film thickness both under an optical microscope mounted on a probe station and SEM.

The schematic of the MEMS based mechanical testing platform proposed for this work is shown in Figure 2.1. The system is composed of three distinct features; a) the load-cell b) the platinum test specimen and c) a cascaded thermal actuator. The test specimen is attached at one end to a fixed-fixed beam that acts as a load sensor and at the other end to the actuator. Since the sample is co-fabricated with the device therefore any specimen misalignment to the actuator and load cell are dictated by the tolerances in the photolithography

masks, which are miniscule when compared to the rest of the structure and therefore can be ignored.

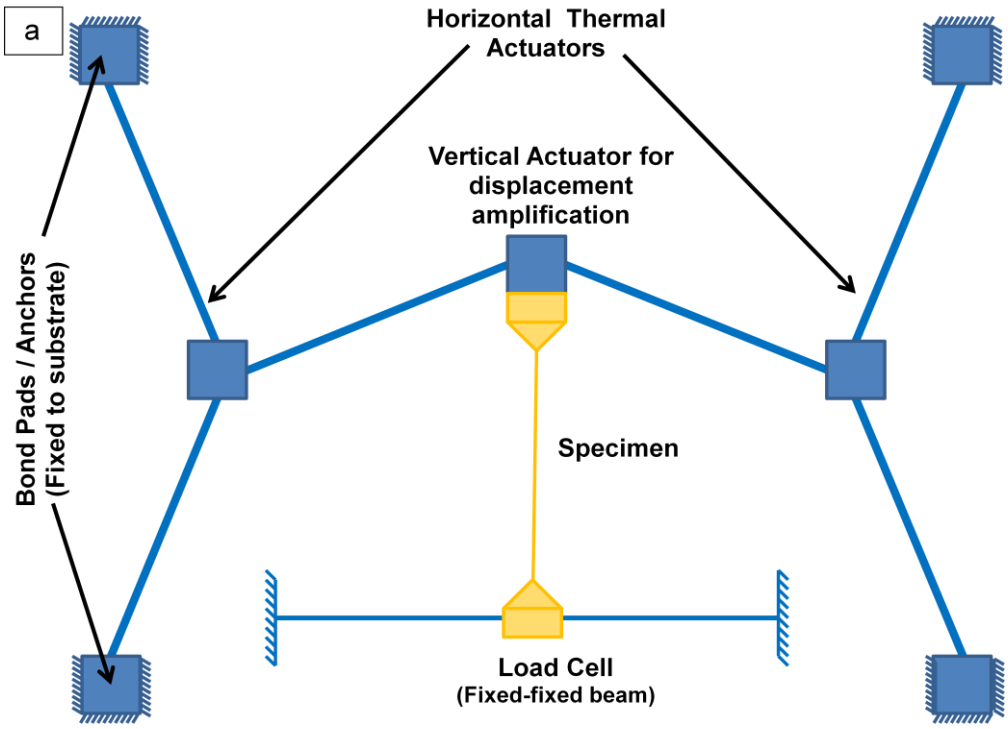

Figure 2.1: Schematic of the proposed test platform [50].

The cascaded actuator system consists of a regular chevron type thermal actuator bridging between two similar actuators on each side. This design was first proposed by the Gianchandani et al. [51] as the means for strain measurement and later for displacement amplification and actuation of micro motors [52, 53]. In this system the motion and force exerted by each side actuator is mechanically amplified by the central chevrons and applied to the test specimen. A simplified schematic of the complete test platform is shown in Figure 2.2a. The platform can further be divided into three constituent subsystems labeled in Figure 2.2b as the ‘specimen and load cell system’, the ‘vertical

actuator system' and the 'horizontal actuator system'. The actuators are labeled based on the direction of their actuation motion.

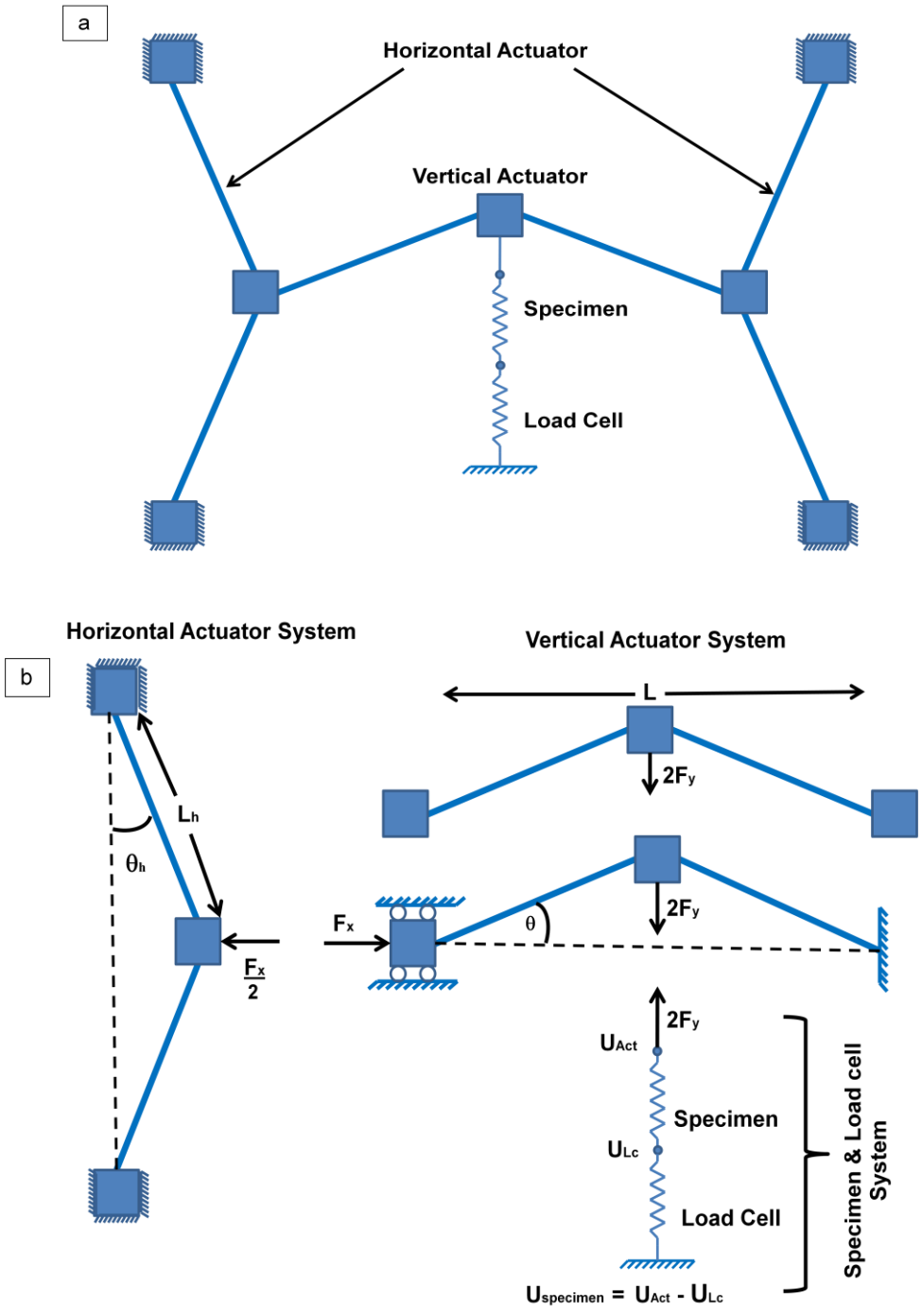

Figure 2.2: a) Simplified schematic of the test platform shown in Figure 1. b) Division of platform into its constituent subsystems for the ease of analytical modeling. The subsystems are specimen and load cell system, the vertical actuator system and the horizontal actuator system [50].

2.1. Design criteria and Modeling

In order to design the test platform for materials testing, it is essential to specify the range of specimen load and displacement required for the test specimens. The test platforms shown in Figure 2.1 are to be designed such that it is capable of providing up to several milli-newtons of force and a displacement of up to 25 μm simultaneously with temperature change (ΔT) of less than 50 ^{o}C on a specimen that is 2 μm wide and up to 500 μm long and variable thickness of the range 75nm-1μm. Although the force and the displacement required for the platinum test specimens is much lower, the specifications are set purposefully much higher than the requirement to allow for some margin to work with stronger specimens if required. On test platforms used for testing nano scale material such as this, it is imperative that the temperature change across the test specimen remains insignificant and does not affect the specimen compliance. The temperature gradient specification of < 50 ^{o}C has been selected based on similar work by other researchers [48].

Based on the specifications laid out above, analytical and finite element models were developed for the actuator based test platforms and some general trends were observed. Change in temperature 'ΔT' increases linearly with the increase in displacement produced at the specimen and can be optimized by designing the actuators to produce maximum displacement for minimum force. The cascaded actuator system comprised of horizontal and vertical actuator systems proposed here is basically a displacement amplifier whereby the displacement produced in the horizontal actuator system is amplified by the

vertical actuator system. Parameters that increase output or specimen displacement would generally decrease the available output force for it. Listed below are some of the parametric trends for the cascaded actuator system without being loaded by a specimen.

- Available maximum output displacement increases with the increase in the chevron length
- Available maximum output displacement increases with the decrease in the chevron angles
- Available maximum output displacement is not affected by the chevron cross-sectional area
- Available maximum output displacement is not affected by the number of chevrons
- Available maximum output force increases with the decrease in available maximum output displacement
- Available maximum output force increases with the increase in chevron angle
- Available maximum output force increases with the decrease in chevron length
- Available maximum output force increases with increase in chevron cross-sectional area

- Available maximum output force increases linearly with the number of chevrons

As the above list indicates that design parameters produce conflicting outcomes, e.g. maximizing output force lowers the possible displacement. Therefore tradeoffs must be made to meet the desired load and displacement specifications. The geometric parameters selected for this work are presented in Table 2.1.

Table 2.1: Parameter values for the cascaded actuator system.

	Parameter	Value
Horizontal Actuator System	Chevron length on each side of shuttle	1000μm
	Chevron width	5μm
	Chevron thickness	25μm
	Chevron angle	5^o
	Number of chevrons	15
Vertical Actuator System	Chevron length on each side of shuttle	1000μm
	Chevron width	5μm
	Chevron thickness	25μm
	Chevron angle	5^o
	Number of chevrons	15
Load Cell Beam	Length of fixed-fixed load cell beam	400μm
	Width of the beam	5μm
	Number of the load cell beams	1

2.2. Analytical Model

As depicted in Figure 2.2b the actuator system can be divided into its constituent subsystem for the ease of analytical modeling. The subsequent section provides detailed models of each subsystem.

2.2.1. Specimen and load cell system

The specimen and load cell system can be modeled as a system of two springs of stiffness k_{Spec} and k_{Lc} in series with one another as represented in Figure 2.3.

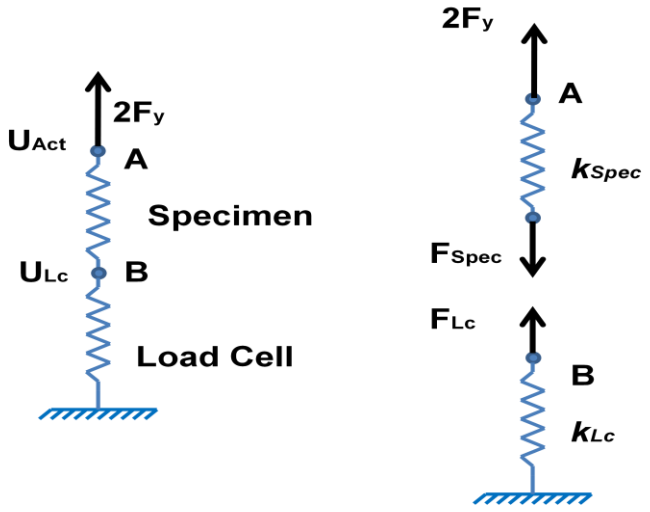

Figure 2.3: Free body diagram of the specimen and load cell system [50].

Where, U_{Act} and U_{Lc} are the displacements at nodes 'A' and 'B' respectively and can be measured during the test. Also, from the free body diagram of the system above:

$$F_{Lc} = F_{Spec} = 2F_y \tag{1}$$

Load cell: Specimen is attached at one end to a load cell which is a fixed-fixed type beam. It has been demonstrated that for very small displacements roughly until ¼ of the width of the beam; the displacement of the beam can be approximated linearly [54, 55]. However for large displacements, which is the situation in this case, the second order effects of beam bending and a tensile lateral force 'S' (Figure 2.4) acting along the beam axis cannot be ignored.

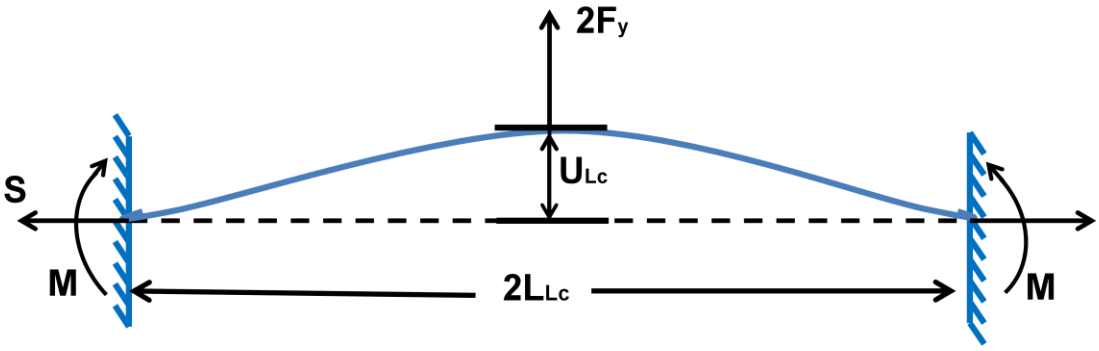

Figure 2.4: Free body diagram of load cell beam [50].

This non linear system can be solved by eliminating '*u*' which is a function of tension in the beam in the following set of equations [56]:

$$U_{Lc} = 2\left(\frac{2I_{Lc}}{A_{Lc}}\right)^{1/2}(u - \tanh u)\left(\frac{3}{2} - \frac{1}{2}\tanh^2 u - \frac{3}{2}\frac{\tanh u}{u}\right)^{-1/2} \tag{2}$$

$$F_y = \frac{8EI}{(L_{Lc})^3}\left(\frac{2I_{Lc}}{A_{Lc}}\right)^{1/2} u^3\left(\frac{3}{2} - \frac{1}{2}\tanh^2 u - \frac{3}{2}\frac{\tanh u}{u}\right)^{-1/2} \tag{3}$$

where:

$$u = \sqrt{\frac{S(L_{Lc})^2}{EI_{Lc}}}$$

'A_{Lc}', and 'I_{Lc}' are the cross-sectional area and the second moment of inertia of the load cell beam. 'L_{Lc}' is the half the length of the beam as described in the Figure 2.4.

Specimen: The elongation experienced by the specimen is the difference between the actuator motion and load cell displacement (Figure 2.3) and both are measured during the test.

$$U_{Spec} = U_{Act} - U_{Lc} \tag{4}$$

Therefore, the stress and strain on the specimen are calculated directly.

$$\sigma_{Spec} = 2\frac{F_y}{A_{Spec}}; \qquad \varepsilon = \frac{U_{Spec}}{L_{Spec}} \tag{5}$$

Where 'A_{Spec}' and 'L_{Spec}' are the cross section area and the gage length of the specimen.

2.2.2. Vertical actuator system

The vertical actuator system is a system of chevrons connected to a common central shuttle at one end and at the other end chevrons are attached to the horizontal actuator system as depicted in Figure 2.2a. By taking into account symmetry the system can be simplified to a single beam under lateral bending and axial compression as depicted by the free body diagram in Figure 2.5.

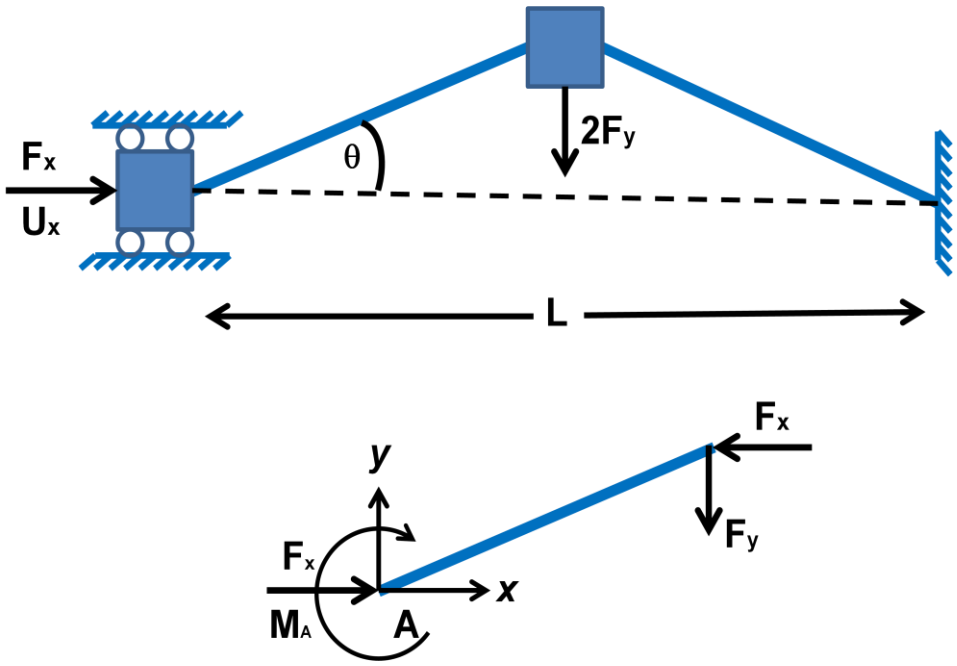

Figure 2.5: Free body diagram of the vertical actuator system. The system was reduced to a single beam under lateral bending and axial compression by taking into account the system symmetry [50].

The bent beam described by the free body diagram in Figure 5 is modeled as:

$$M_A = EI\frac{\partial^2 y}{\partial x^2} = F_y x - F_x y \tag{6}$$

And the boundary conditions:

$$y_{x=0} = 0; \qquad \left.\frac{\partial y}{\partial x}\right|_{x=0} = \left.\frac{\partial y}{\partial x}\right|_{x=L/2} = \tan\theta$$

The solution to the above nonlinear second order homogeneous differential equation is given by [51]:

$$U_{Act} = 2\frac{\tan\theta}{k}\left[\tan\frac{kL}{4}(1-\cos kx)+\sin kx\right]-\frac{L}{2}\tan\theta$$

where $k = \sqrt{\frac{F_x}{EI}}$

$$U_{Act}\big|_{x=L/2} = 2\frac{\tan\theta}{k}\tan\frac{kL}{4}-\frac{L}{2}\tan\theta \qquad (7a)$$

Where $U_{Act}\big|_{x=L/2}$ is the displacement of the central shuttle when subjected to the lateral force F_x. For actuator displacement with no load (F_y = 0) equation (7a) is reduced to:

$$U_{Act}\big|_{x=L/2} = 2\frac{\tan\theta}{k}\tan\frac{kL}{4} \qquad (7b)$$

The shortening of the beam the subjected to lateral force F_x is given by [57]:

$$\frac{L'}{2} = -\frac{1}{2}\int_0^{L/2}\left(\frac{\partial U_{Act}}{\partial x}\right)^2 dx \qquad (8)$$

L' is the difference between the actual length of the beam and its projection along x-axis. By solving equations (7) and (8) we get:

$$L' = \frac{(\tan\theta)^2}{4k}\left[2G + kL + kLG^2 + \sin kL - 2G\cos kL - G^2 \sin kL\right] \tag{9}$$

where: $G = \tan\frac{kL}{4}$

With the increase in the compressive load the beam bends such that *L'* also increases. However the change in *L'* does not take into account the elastic deformation of the material. Therefore the total lateral displacement is obtained by combining the contributions both bending and elastic deformations along x-axis.

$$U_x = \Delta L' + \frac{F_x L}{Ewh} \tag{10}$$

where 'w' and 'h' are the width and height of the beam and 'E' is the Young's modulus of the beam material.

Que et. al. [52] defined the max actuator displacement as that at which the shuttle displacement is zero and derived the following expression by complementary energy method.

$$\left(F_y\right)_{\max} = \left(U_{Act}\right)_{\max} K_y; \qquad K_y = m\frac{2\sin^2(\theta')AE}{L} \tag{11}$$

Where *m* is the number of chevrons attached to shuttle, θ' is the effective bending angle which may differ from the designed angle due to shuttle displacement.

The relationship between the lateral force $(F_x)_{max}$ for maximum shuttle displacement $(U_{Act})_{max}$ and peak output force $(F_y)_{max}$ can be given by:

$$\left(F_y\right)_{\max} = \left(F_x\right)_{\max} \tan\theta \tag{12}$$

In order to obtain the maximum actuator output force $(F_y)_{max}$; the deflection is set to zero (U_{Act} = 0) and in order to obtain the max actuator deflection (U_{Act}) the output force is set to zero (F_y = 0).

From the equations presented above the analytically calculated force that the proposed actuator design is capable of providing is 250 mN which is roughly 100 times greater than what is required for testing platinum thin film specimens.

2.2.3. Horizontal actuator system

On either side of the vertical actuator system are horizontal actuators. They are the main source of lateral force and displacement that is amplified by the vertical actuator. The lateral force and displacement in the horizontal actuators is generated by the thermal expansion of the chevrons due to Joule heating. As shown in the schematic (Figure 2.6) the horizontal actuator system is very similar to the vertical actuator system described in the previous section and can be modeled in a similar fashion.

The relationship between the displacement of the actuator and the change in temperature required to generate is given by [51]:

$$\Delta T = \frac{1}{\alpha L_h}\left[\Delta L_h' + L\frac{F_x/2}{E_h A_h}\right] \tag{13}$$

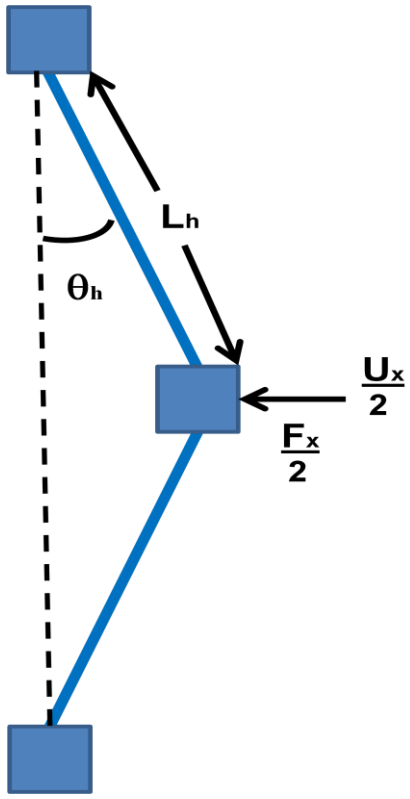

Figure 2.6: Schematic representation of horizontal actuator system [50].

However, from the perspective of device design; Equation (13) does not provide a straightforward correlation between the lateral displacement of the horizontal actuator and temperature rise required to produce it. For this purpose Zhu et. al. [48] provides a simpler linear approximation by considering both lateral bending and axial deformation for small deflections.

$$\Delta T = \left[K_{TA} U_x - \frac{F_x}{2} \right] \left[\frac{1}{2\alpha E_h A_h \sin\theta_h} \right]$$

Where

$$K_{TA} = 2\left(\sin^2\theta_h + \frac{\cos^2\theta_h}{\psi} \right) \text{ and } \quad \psi = \frac{A_h L_h}{12 I_h} \tag{14}$$

A_h, L_h, I_h are the cross sectional area, length, and second moment of inertia, respectively, of the actuator chevron. θ_h is the chevron angle with respect to vertical as depicted in Figure 2.6 E_h is the Young's modulus of the actuator material. The assumption of small actuator deflection is valid in this case because each horizontal actuator sees half the overall compression and a fraction of displacement output by the vertical actuator.

2.2.4. Thermo-mechanical response

The thermo-mechanical behavior of the device was modeled analytically using parameters previously provided. As with any modeling technique the accuracy of the results depends greatly on the material properties being used. For the thermo-mechanical model the Young's modulus of the actuator's structural material and the coefficient of thermal expansion (CTE) are the required important properties. These micro fabricated MEMS actuators will be fabricated on single crystal silicon substrate. The value of Young's modulus for Si (100) of 164 GPa is used for the purpose of this study. The value of coefficient of thermal expansion for Si at room temperature is 2.5 x 10^{-6} C^{-1}, but increases greatly with the temperature. In order to simulate the results as close to the

reality as possible the expression of instantaneous CTE for single crystal silicon between 300 K and 1500 K by Okada et. al. [58] was used:

$$\alpha = \left(3.725\times\left(1-\exp\left(-5.88\times10^{-3}\left(T-125\right)\right)\right)+\left(5.548\times10^{-4}\right)T\right)\times10^{-6} \qquad (15)$$

where α is the CTE and T is the temperature in Kelvin**.** The relationship between the horizontal actuator compression (in μm) due to the motion of horizontal actuators and vertical actuators displacement and change in temperature (ΔT) required to produce it, which were calculated analytically (Equations 7 and 13), are presented in Figure 2.7.

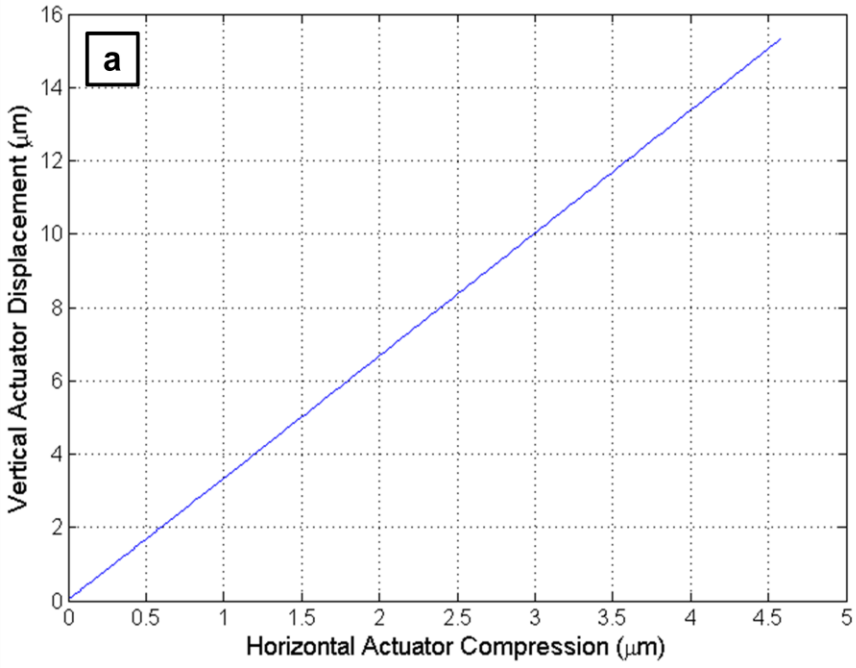

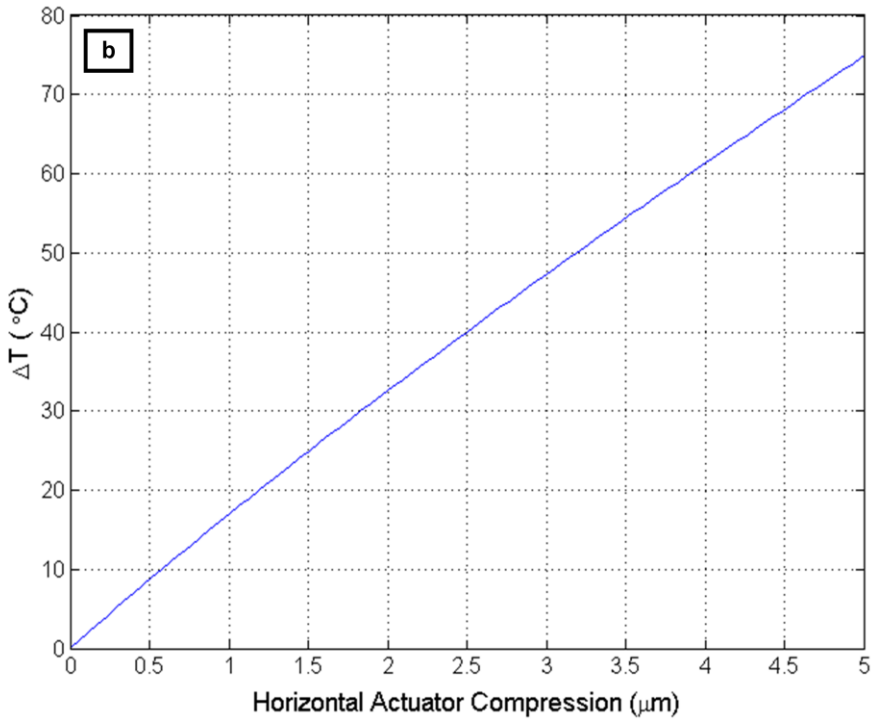

Figure 2.7: a) Relationship between the horizontal compression due to the motion of horizontal actuator displacements (in μm) of and vertical actuators displacement for system shown in figure 1, calculated analytically. b) Relationship between the horizontal compression due to the motion of horizontal actuator displacements and change in temperature (ΔT) required to produce it calculated analytically [50].

It may be noted that in order to produce the overall horizontal compression on the actuator system, each horizontal actuator has to provide half the required displacement. Therefore, it may be deduced from Figure 7a that the proposed design produces a displacement amplification of approximately 3.3 times. The displacement amplification provided by the cascaded actuators has the additional benefit of reducing the ΔT required for producing the load and displacement required. The ΔT necessary for actuation of the cascaded actuator structure has been lowered by roughly 3 times over the similar range of motion for a standard single chevron thermal actuator. For the specimen specifications outlined previously, the required vertical actuator displacement remains below 5-6 μm.

From Figure 2.7a and b it can be observed that required horizontal actuator compression to produce 5 – 6 μm vertical actuator displacement is approximately 0.5 - 1μm and $\Delta T < 30\ ^{o}C$.

2.3. Finite Element Model

Multiphysics finite element analysis (FEA) was also conducted in ANSYS software and was also used to simulate the performance of the unloaded devices. The FEA model was a coupled model of electric, thermal and mechanical fields with applied voltage as the input parameter and force and displacement at the specimen location as the outputs of interest. Electrical boundary condition of applied voltage was set at the anchors / bond pads. The mechanical boundary condition was fixed displacement at the bond pads. A thermal boundary condition was constant room temperature at the bond pads. The thermal and displacement fields are shown in Figure 2.8.

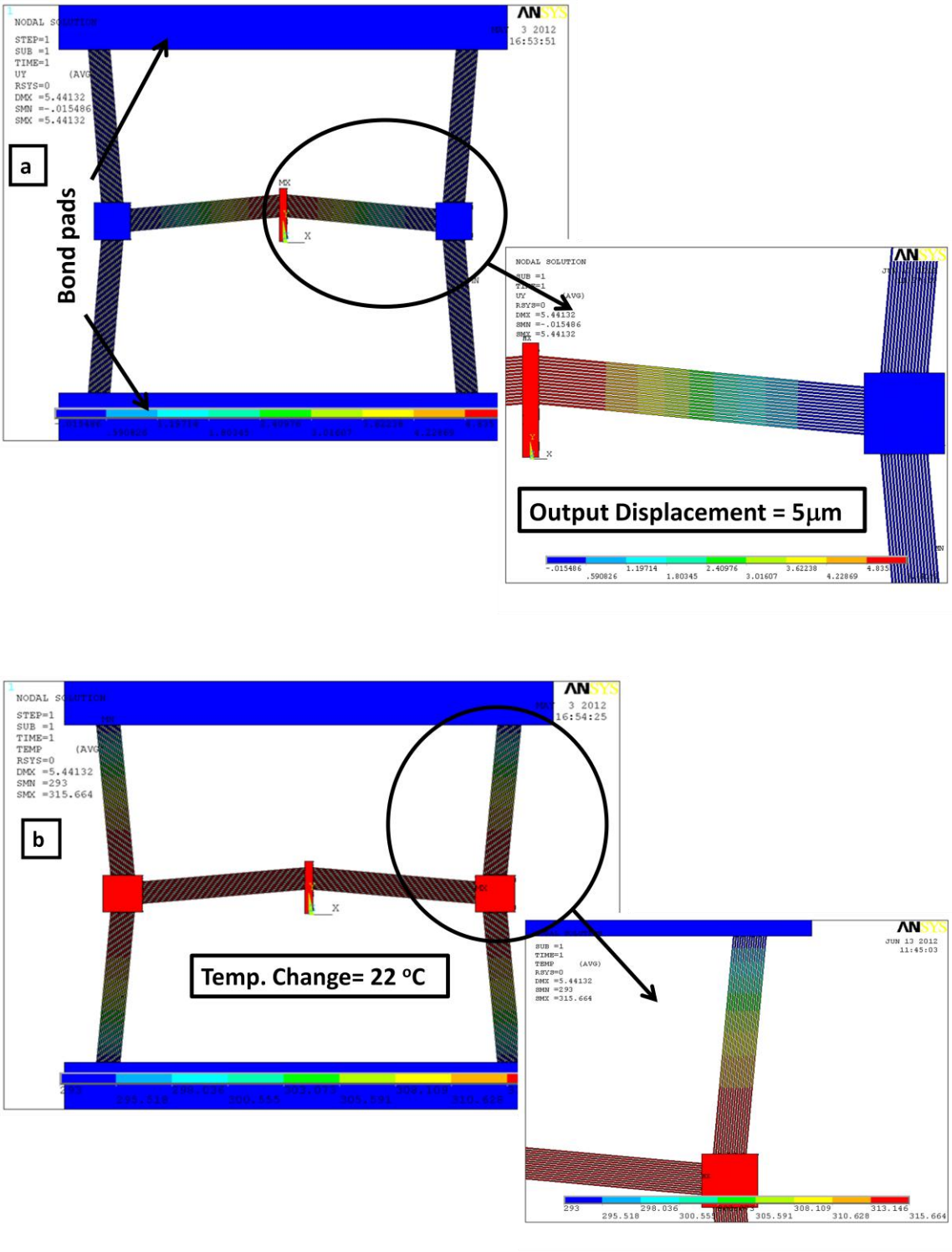

Figure 2.8: (a) Displacement (in μm) and (b) temperature (in K) fields of cascaded thermal actuator system [50].

The emphasis of the finite element model was on predicting the thermo-mechanical response of the system and not the electro-thermal response. Since in practice the single crystal Si (SCS) wafers used are boron or phosphorous doped (n-type or p-type) and not virgin SCS wafers and the electrical resistivity of the wafer even from the same lot varies from wafer to wafer. This makes it very difficult to accurately define the electrical resistivity (at room temperature and/or as a function of temperature) in the FEA simulation that will be a true representative of the experimental system. The thermomechanical response however is dependent on the material properties such as thermal conductivity and coefficient of thermal expansion for Si and are well documented in literature [58, 59]. Therefore a very accurate thermomechanical response simulation is possible and was conducted.

At the max displacement of roughly 5.5μm (1.1% strain on 500 μm long beam), ΔT across the system is just 22^{o} C. The difference between the ΔT provided analytic model and that provided by the FEA model was less than 10% for the entire test range. This low temperature gradient is very important when seeking the material properties of a piece of material at specified temperature. This is a great advantage of this design. As a comparison, the displacements and temperature fields of a standard thermal actuator with same chevron length and angle is presented in Figure 2.9. The ΔT on this actuator for 5 μm displacement despite the addition of heat sink beams to lower the temperature at the specimen interface is 148 ^{o}C. The heat sinks beams were: 5 in number, 400μm long, and have a cross section of 5 μm x 25 μm

a

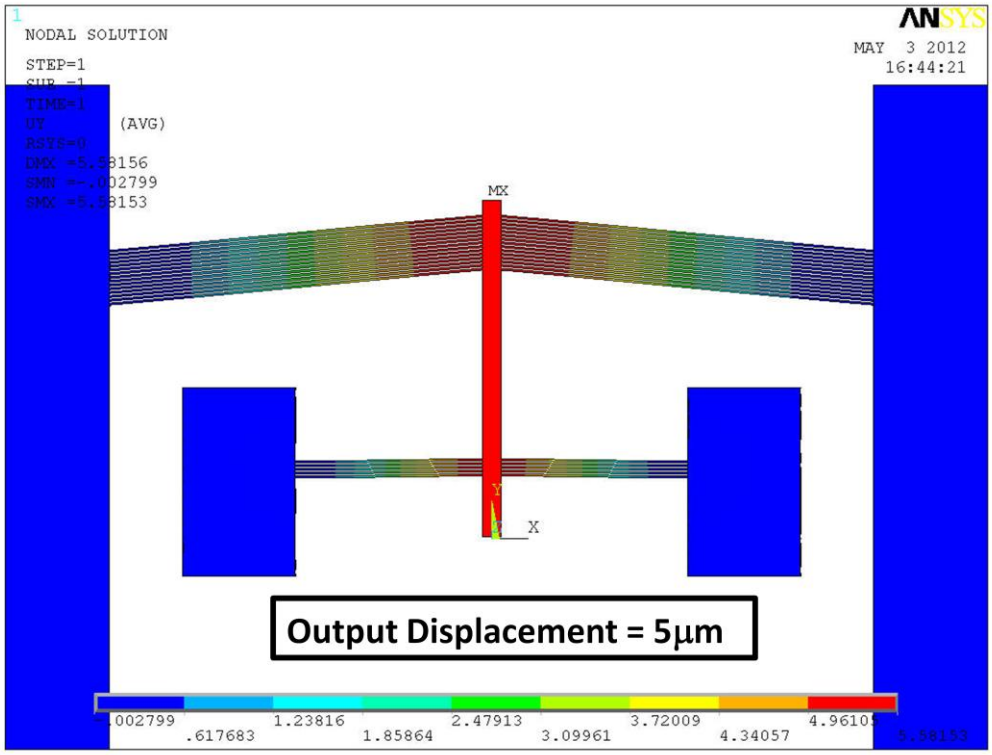
NODAL SOLUTION
STEP=1
TIME=1
UY (AVG)
MAY 3 2012
16:44:21
MX
Output Displacement = 5μm
.617683
1.23816
1.85864
2.47913
3.09961
3.72009
4.34057
4.96105

b

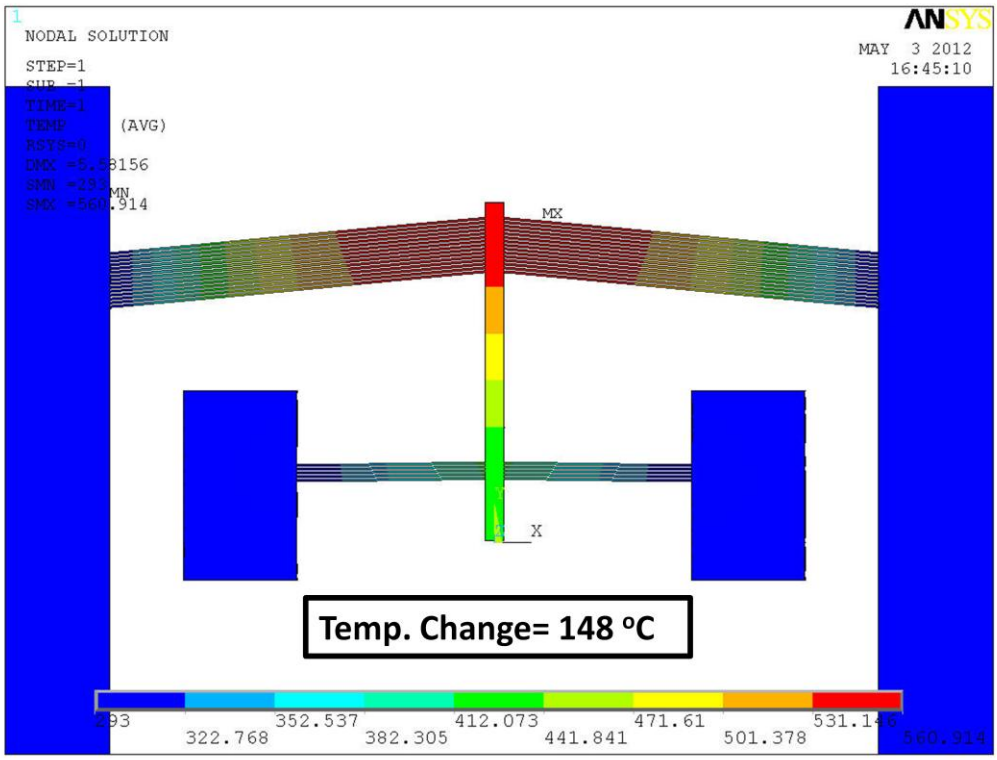
NODAL SOLUTION
STEP=1
TIME=1
TEMP (AVG)
MAY 3 2012
16:45:10
MX
Temp. Change= 148 °C
322.768
352.537
382.305
412.073
441.841
471.61
501.378
531.146

Figure 2.9: (a) Displacement (in μm) and (b) temperature (in K) fields of standard thermal actuator system [50].

The maximum force output of the actuator systems from the finite element model is obtained in a method similar to the analytical model by applying the boundary condition of a fixed end on the shuttle at the specimen location and determining the reaction force from the FEA solution.

Chapter 3

DEVICE FABRICATION

3.1. Mask Design and Development

First step in the development and fabrication of a MEMS device is the design and development of photolithography masks. The mask is flat glass plate with the desires pattern usually of chrome. They are needed to transfer the required pattern onto the light sensitive photoresist. The chrome pattern blocks the light exposure on the part of the wafer coated with photoresist underneath. This makes the exposed areas of the photoresist more soluble in the developer solution, thereby transferring pattern. The mask was designed using the AutoCAD software and all the design considerations described in previous chapter were accommodated in the design. As the MTTC cleanroom facility is equipped for 6 inch wafers the masks designed were all 7”x7” suitable for 6” wafers. Four masks were designed 1) Specimen mask 2) Bondpad pattern, 3) Actuator pattern and 4) Specimen opening. After the completion of the design the CAD files were sent out to a photomask manufacturer for generation.

3.2. Actuator Fabrication

The MEMS actuator fabrication is the most challenging aspect of this study to implement. The difficulty lies in fabricating a freestanding nano structured membrane and retaining it intact until the end of the process. The summary process flow for the fabrication of the micro-actuator system along with the co-fabricated platinum freestanding test films is as follows:

a. The fabrication is performed on a SOI (Silicon on Insulator) wafer with device layer of 20-25 μm of Si, Buried Oxide or BOX of 1-2 μm and handle layer of ~600 μm thick Si. Crystal orientation on both the device layer and handle layer were (100). The resistivity of the device layer for the wafers used was 0.01-0.02 Ohm-cm. The resistivity of the handle layer for the wafers used was 10 Ohm-cm. The lower resistivity on the device layer provides good electrical path on a MEMS device surface and a higher resistivity (less dopant) on the handle layer prevents higher residual stress in the wafer from buckling the freestanding beams upon release. These wafer specifications have been chosen from author's past experience with MEMS devices during his Masters Work [60] (Figure 3.1a).

b. The specimen pattern in platinum is formed on the wafer device layer by forming an inverse pattern by use of photolithography followed by electron beam evaporation of platinum metal on to the wafer. The photoresist (PR) is later removed along with the excess metal to provide the pattern of the platinum specimen. This process is commonly known as 'lift-off' process (Figure 3.1b).

c. In a similar fashion bond pads are patterned next on the wafers by the lift-off process. Bond pads are comprised of a layered structure of Al/Cr/Au in a 800nm / 100nm / 100nm configuration. From the past experience, this configuration provides a good Ohmic contact with the Si surface and sufficiently soft and stable pad surface for wire bonding later (Figure 3.1c).

d. Next, the designed actuator is patterned in PR aligned to both the platinum specimen and bond pads. The device layer will then be etched down to the BOX layer by ‘Deep Reactive Ion Etching’ (DRIE) using the Bosch process [61]. This process creates a high aspect ratio structure by etching vertically down from the edge of the PR layer. Next, the PR layer is removed using acetone, isopropyl alcohol, and de-ionized water rinses respectively (Figure 3.1d).

e. Next the wafer is coated again with the PR sufficiently thick to cover the entire high aspect ratio structure. The PR is then etched selectively to expose the specimen area. The Si under the platinum sample is then etched in a custom built XeF_2 etching system to form a freestanding thin film platinum specimen. The PR over the remaining area is removed next in an O_2 plasma (Figure 3.1e).

f. Finally the device is released by timed etching of the BOX layer in a custom-built vapor HF system. The completed device had a free standing platinum thin film specimen, the freestanding actuator structure and anchors. Some of the anchor structures act as both the substrate anchor and surface for bond pads and wire bonding (Figure 3.1f).

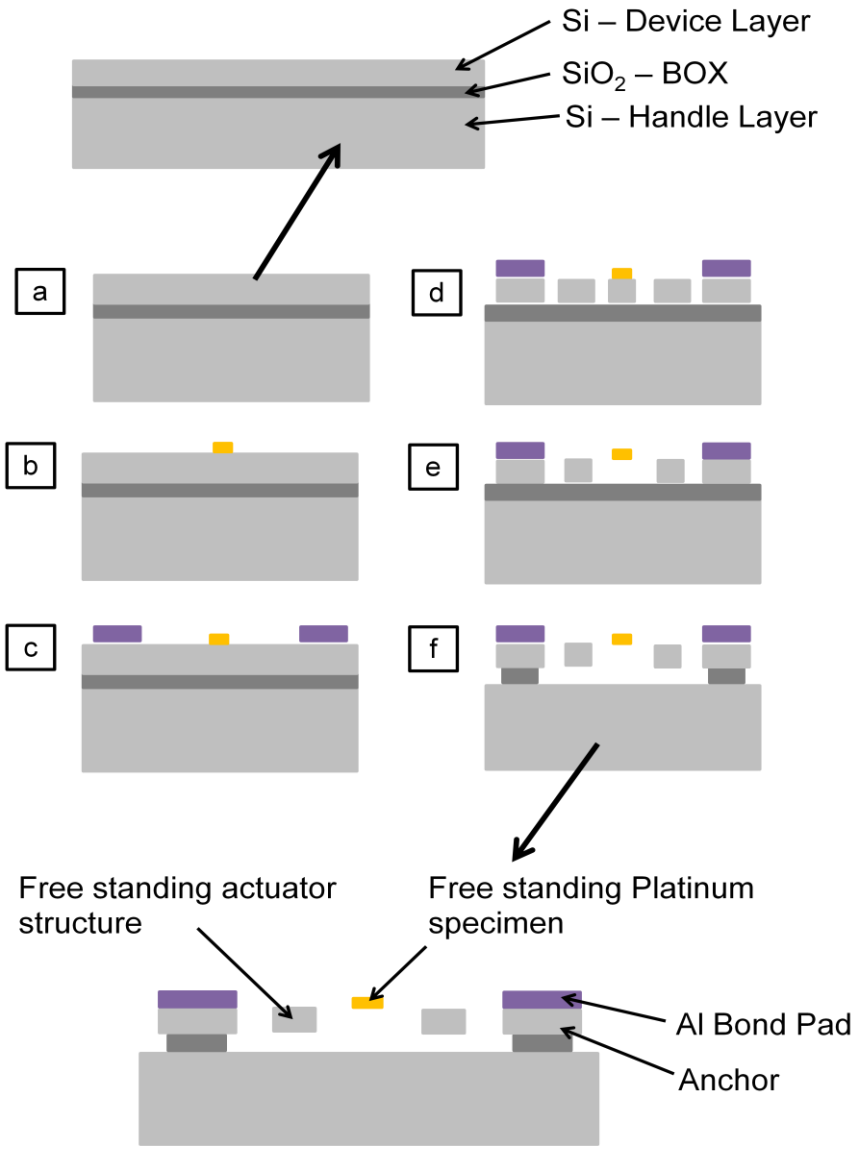

Figure 3.1: Schematic of the device fabrication process. a) SOI wafer b) Platinum specimen is patterned on the device layer c) Bond pads are patterned on the device layer d) Actuator is patterned on the device layer and Si is etched by DRIE down to the BOX layer e) Specimen is released by selectively etching Si underneath it in XeF_2 f) Device is released in vapor HF [50].

The detailed step-wise process sheet is provided in Appendix 'A'. SEM image of the fabricated device with 250μm long and 2μm wide and 250nm thick free standing Pt test specimen is shown in Figure 3.2 below:

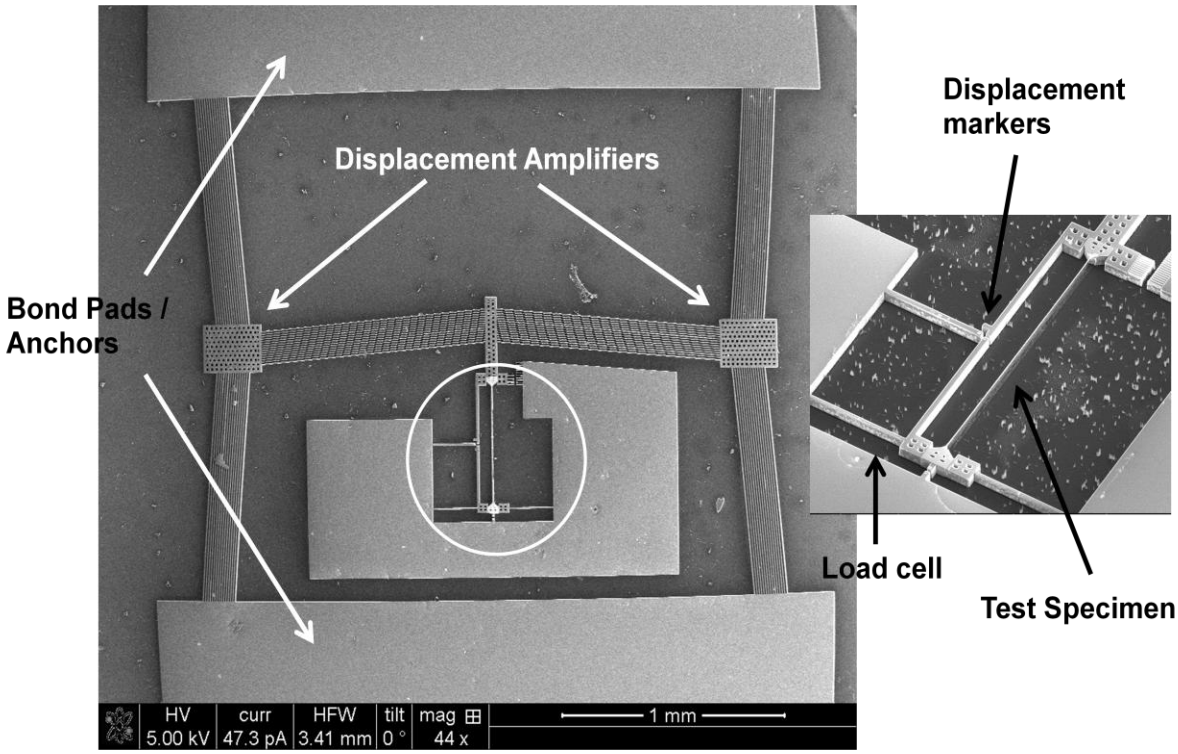

Figure 3.2: SEM picture of a cascaded thermal actuator system with co-fabricated freestanding Pt specimen. All chevrons on the actuator are 5 μm wide, 1000 mm long, at a 5^{o} angle, and the structure is 25 μm deep (into the page). The Pt sample is 2 μm wide, 250 nm thick and 500 μm long [50].

Energy dispersive spectroscopy (EDS) signatures were collected on the free standing thin film specimens to check for the contaminations and impurities on the specimen surface introduced during the fabrication process. The author's main concern was the use of O_2 plasma at the final step to remove photoresist residue may have also created a thin layer of Pt_xO_y on the Pt surface. A screen shot of the EDS results below indicate no appreciable O_2 signature, see Figure 3.3.

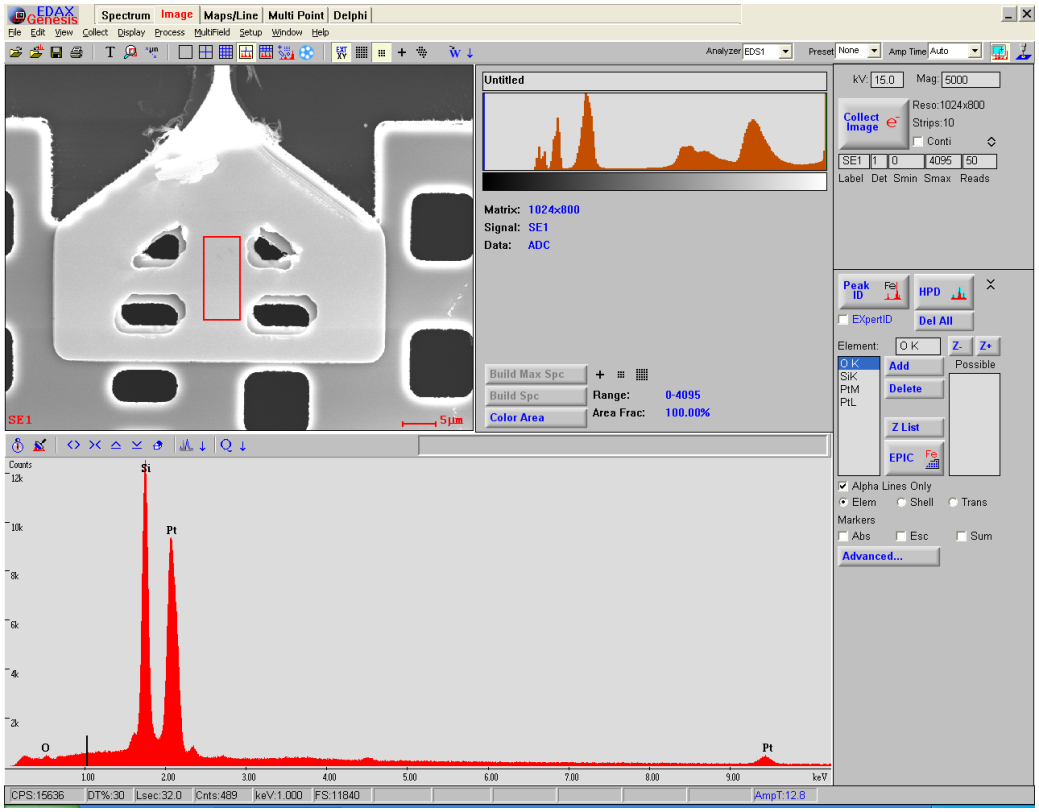

Figure 3.3: Screen shot of energy dispersive spectroscopy signature obtained for the thin film specimen.

Chapter 4

EXPERIMENTAL SETUP AND CHARACTERIZATION

Large displacements and extremely low temperature gradients on these cascaded thermal actuators allow their use both in SEM and under an optical microscope. The following sections describe both these experimental setups.

4.1. Optical microscope setup

Use of optical microscope on a probe station enables quick set up and ease of experimentation. The device die is setup on the vacuum chuck of a probe station equipped with an optical microscope with extra long working distance objectives mounted on the 4 lens turret. Electrical connections are made to the device die via tungsten probes mounted onto micro-positioners. The micro-positioners provide accurate X, Y and Z positioning of the tungsten probes, which are brought in contact with the bond pads on the die.

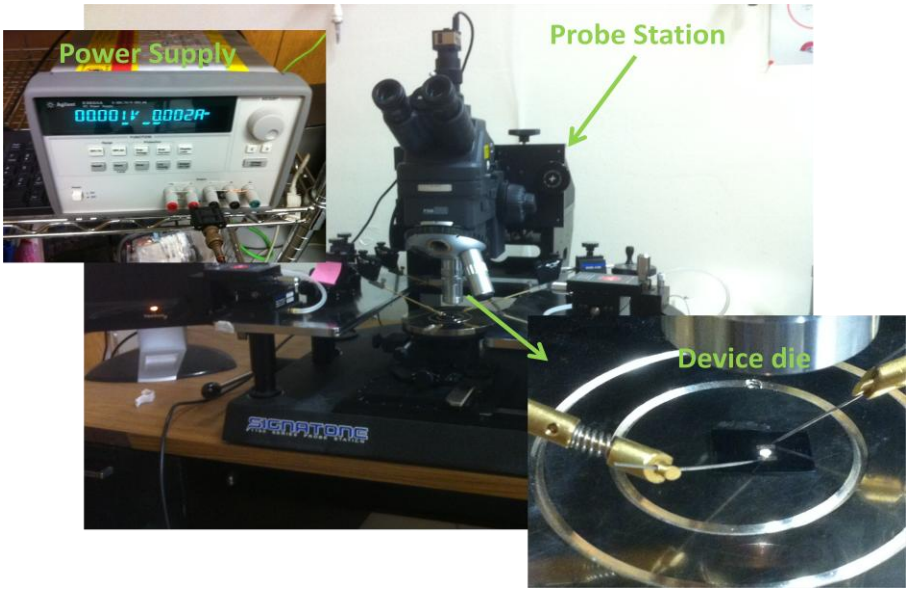

Figure 4.1: The optical test setup.

A computer controlled power supply is later connected to the micro-positioners to drive the MEMS micro actuators on the die. The optical test setup is shown in Figure 4.1.

4.2. Scanning electron microscope (SEM) setup

The scanning electron microscope test setup is more complicated than the optical setup. The device die is first attached to an 84 pin leadless ceramic chip carrier by use of carbon tape. Carbon tape provides good electrical contact between the die and the chip carrier and prevents charging of the die in the SEM. The choice of chip carrier was based on the size of the cavity (0.7” x 0.7”) to attach the die rather than the number of pin contacts.

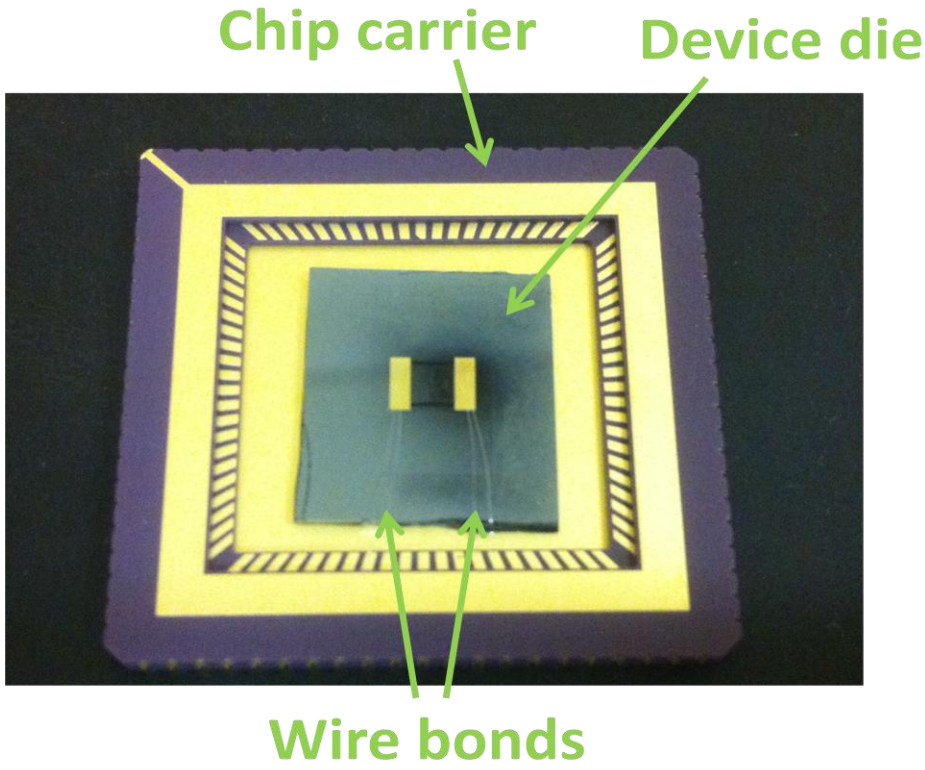

Figure 4.2: Cascaded actuator device die attached and wire bonded to a chip carrier.

Wire bonds are later made between the bond pads on the device and pads on the chip carrier. Figure 4.2 shows a cascaded actuator device die attached and wire bonded to a chip carrier.

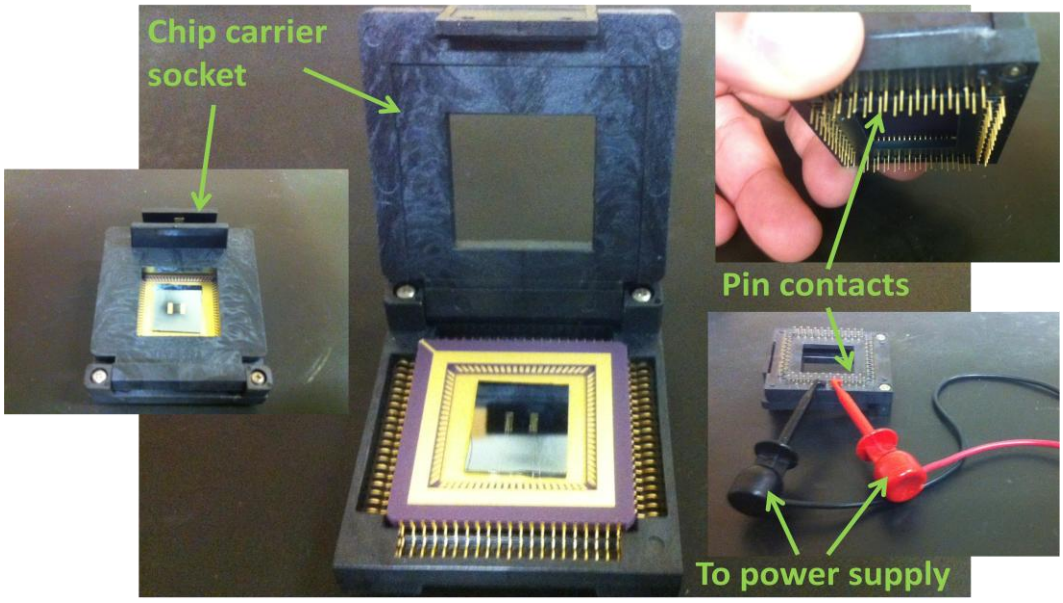

Figure 4.3: Assembly of the cascaded actuator die on the chip carrier and socket for testing in SEM.

The chip carrier is later assembled into a chip carrier socket. The vacuum chamber on FEI Quanta 200 environmental scanning electron microscope (ESEM) has an electrical feed thru port with 7 SMB connections for the making electrical contact between vacuum and air sides. A custom built cable with two SMB connectors on one end and hook type test clips on the other is used to connect the pin contacts on the chip carrier socket to the mating SMB connectors on the feed thru port. Figure 4.3 shows the assembly of a chip carrier with MEMS actuator die to chip carrier socket and test clips. The assembled chip carrier socket is then mounted on to FEI stage adaptor for SEM stubs with

carbon tape and installed on to motorized SEM stage. The window on the top side of the chip carrier socket enables viewing of the device in the SEM. The electrical connectors and large size of the socket restricts the rotation and tilt of the SEM stage therefore great care is taken before hand to ensure that the device is installed in the SEM in such a manner so as to avoid any large rotational motion of the stage later.

4.3. Displacement measurement methodology

In order to calculate the specimen stress and strain the measurement of load cell and actuator displacements is required. The accuracy with which these displacements are measured has a direct impact on the accuracy of the test data gathered. Digital image correlation and tracking is author's method of choice for measuring and tracking both load cell and actuator displacements. For this purpose the test data is gathered in the form of a video. This video is later parsed into its constituent frames to generate a sequence of images. A custom set of MATLAB scripts (Appendix 'B') were written that then track the motion of user defined areas or sub images of interest on a base image through this sequence of images. The script then translates that motion into the force and displacement leading to the stress and strain on the platinum thin film specimen. Given below is the description algorithm for the digital image correlation and image tracking script.:

a. The script prompts the user for the path to the sequence of images.

b. The script creates a list of images that it needs to go through. For this it is important that the user follows a naming convention with sequential numbers and that it remains constant to avoid the script from crashing.

c. The script opens the first image on the image-list and sets it as the base image. All the remaining images are then compared to the base image for motion tracking.

d. The user is then prompted to select regions of interest on the base image that need to be tracked.

e. These selected areas are saved as sub images.

f. The script then opens the next image on the list of images and correlates the sub images and retrieves their pixel positions. This process continues until sub images are correlated on all the images of the sequence.

g. This information is then saved and the script exits.

Also represented in Figure 4.4 is the flow chart for digital image correlation and tracking script.

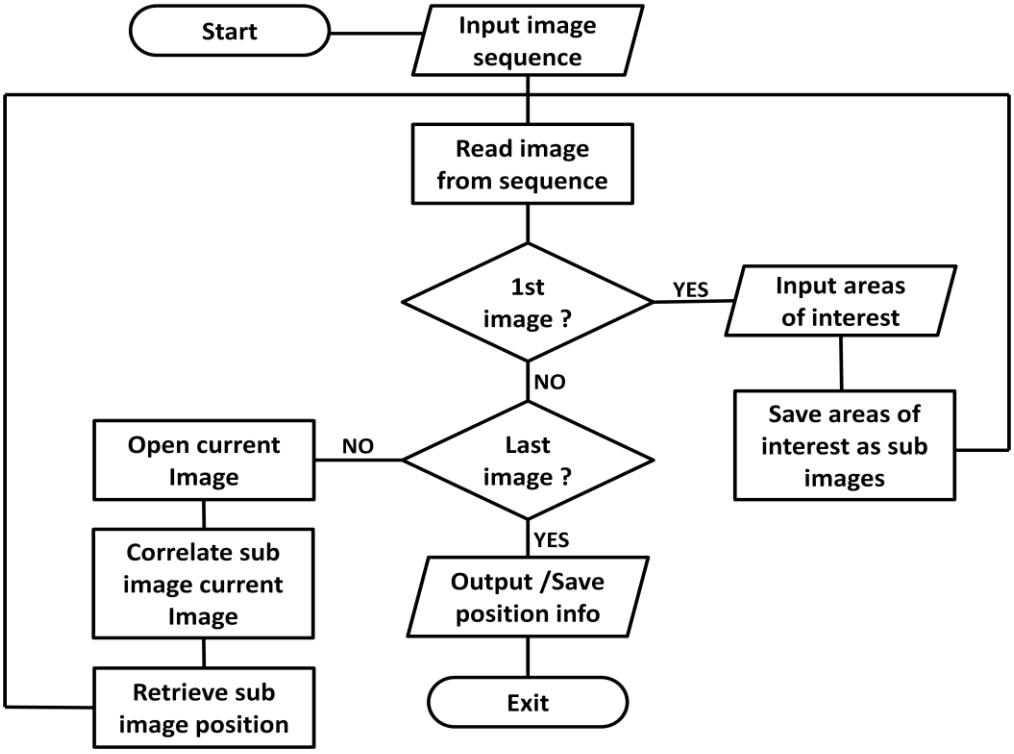

Figure 4.4: Algorithm for the custom digital image correlation script

This saved pixel motion information is then translated into microns by use of μm/px scaling factor based on the magnification and resolution of the CCD camera used for data collection. The load cell displacement when combined with its physical dimensions and stiffness provide the applied force and hence the stress in the thin film, whereas the actuator displacement information provides the specimen strain.

4.4. Digital image correlation and measurement resolution

In order to obtain the stress-strain data on the specimen under test, both the load cell and actuator displacements are required. For this purpose three custom markers were designed in such a way that one was attached to the load cell, a

second was attached to the actuator shuttle and a third for the reference (Figure 4.5).

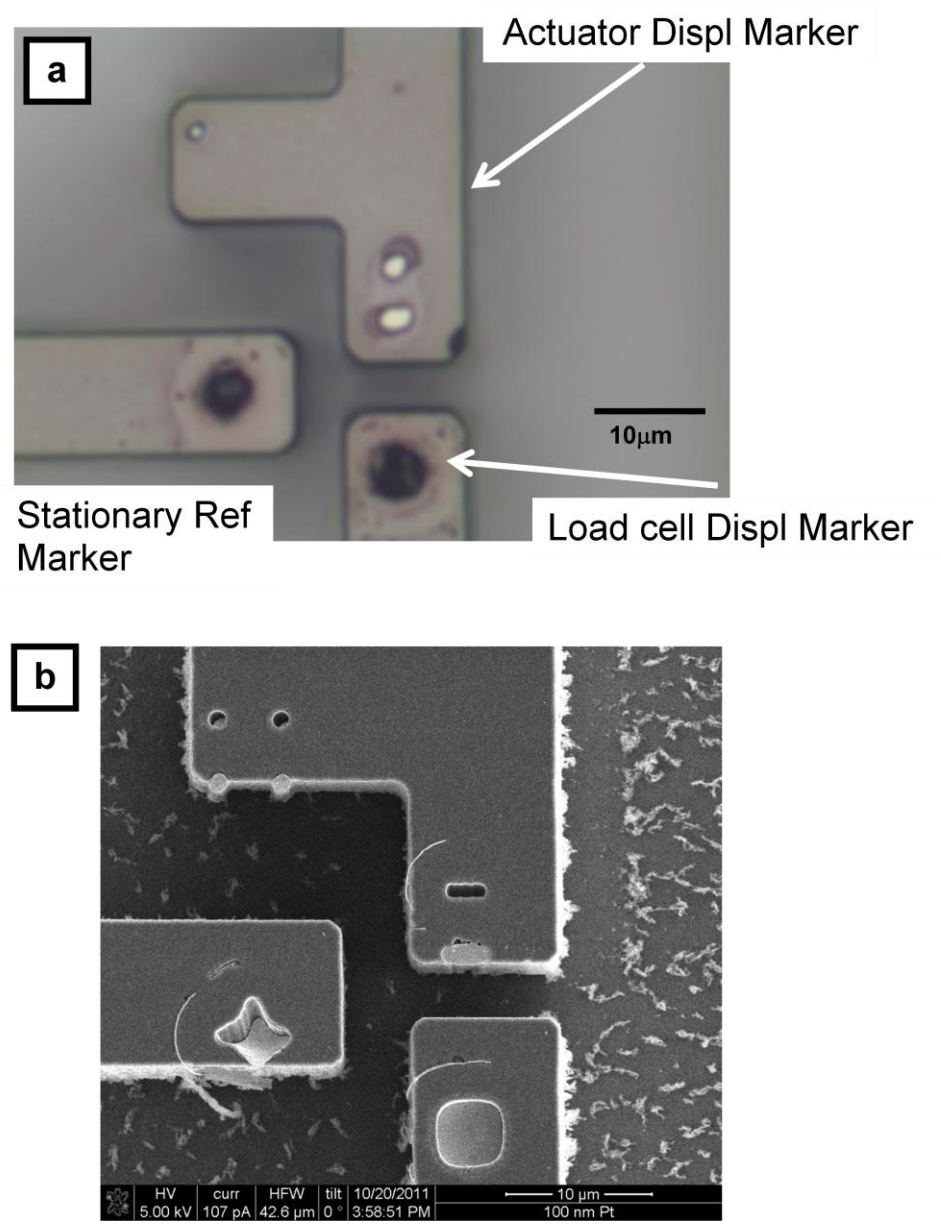

Figure 4.5: a) Optical micrograph and b) SEM image of displacement markers used for digital image correlation are shown for comparison. Both imaging techniques provide roughly similar accuracy of displacement measurement [50].

By tracking the motion of first two markers with respect to the third the displacement of the load cell and actuator can be determined. The Pt thin film

tests were performed both in SEM and on a probe station. Images of the marker motion were collected during the test and later digitally correlated to each other to obtain the data. For tests conducted under the probe station microscope, the images were collected horizontal field width (HFW) of 57.6 μm/px and the image resolution of 3840 x 2748 pixels, which translates to 15 nm/px. SEM images were collected at the HFW of 41.6 μm at the image resolution of 1024 x 886 pixels providing resolution of 40.6 nm/px. It is generally accepted that for rigid body digital image correlation motion accuracy of +/- 1/8 px or better can be achieved [62, 63]. This was in fact true for the SEM images, thus a resolution of 5 nm was attainable for displacement measurement. This allows for a strain of 1×10^{-5} (for 500μm long specimen) to be resolved for the specimens in this work. For optical images it was found experimentally that due to the low image depth of focus the motion accuracy was +/- 1px, which translates to +/- 15 nm. Therefore despite having higher resolution on the optical microscope the uncertainty in the collected data brings the effective resolution of the optical images to 30 nm/px, which allows a strain of 6×10^{-5} to be detected for the tensile specimens in this work (for 500μm long specimen). This displacement resolution also translates into the stress resolution of +/- 10MPa for specimen of cross section 250 nm x 2μm.

4.5. Cascaded Actuator Characterization

For a test platform that will be used for materials testing, it is very important that its own behavior is well characterized. The following sections give the thermo-mechanical and thermo-electrical responses of the cascaded actuator

based freestanding thin film test platform developed by the author for the purpose of this study.

4.5.1. Thermo-mechanical response

The best method to verify and compare the theoretical model to the experimental data is to compare the vertical and horizontal actuator motions of an unloaded device. Figure 4.6 presents this comparison where both the vertical and horizontal displacements of the actuator and temperature change have been calculated using analytical model presented in the previous and are compared to the data obtained by making displacement measurements on an actual device in air. It can be seen that the experimental behavior of the device is in close agreements to the analytical model. The vertical displacements obtained experimentally are roughly 11% lower than those obtain analytically in the specimen test range (vertical displacement < 6 μm) and roughly 8% lower at horizontal displacements of 25 μm. This difference is likely due to convective losses to air in the experiment. Neither the analytical nor FEA models accounted for the heat loss due to convection.

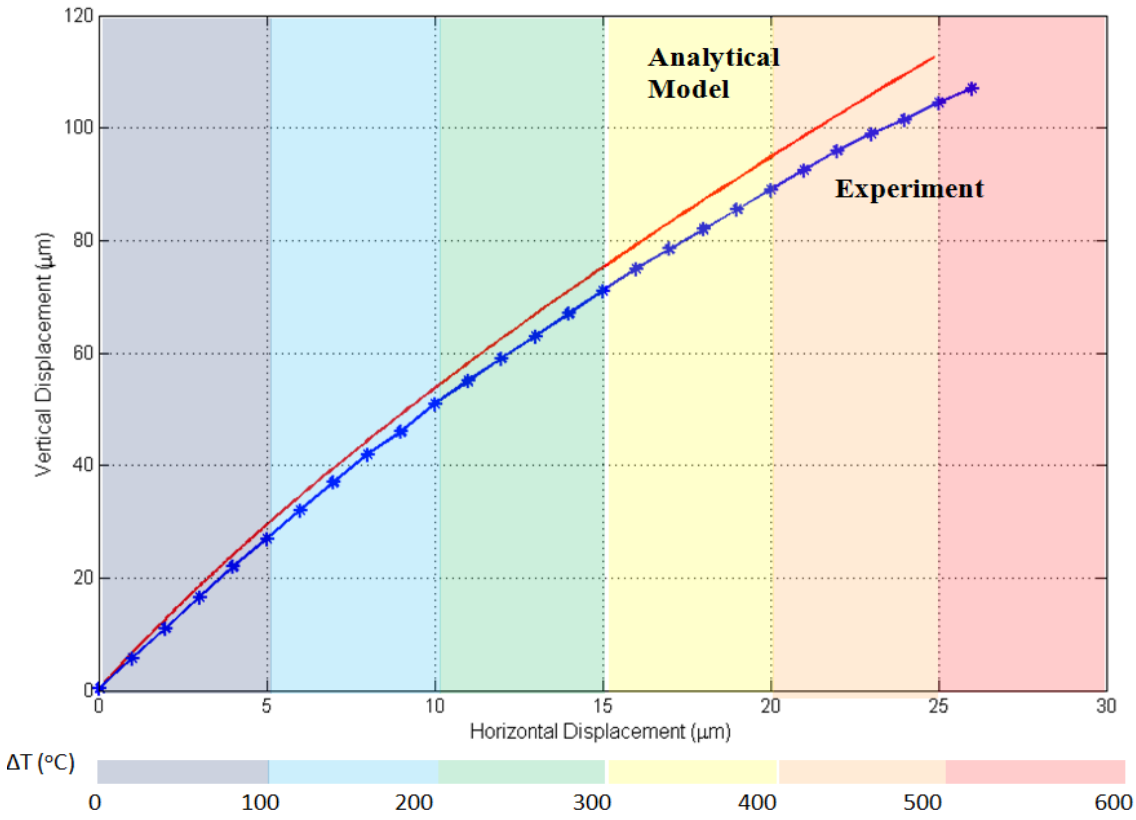

Figure 4.6: Horizontal compression vs. vertical displacement of cascaded thermal actuator system. The theoretical curve and temperature distribution are calculated using the analytical model. Experimental response is close agreement to the analytical model [50].

4.5.2. Electro-mechanical response

In order to characterize the electro-mechanical response of the device, it was operated with Agilent E3634A programmable power supply. It was discovered that for output displacements of < 20 μm, the specimen displacement of the device proportionally increased with the applied power. For these experiments a custom MATLAB script was written to control the power supply (Appendix 'C'). The script read the instantaneous current and voltage applied to the device while incrementing the voltage such that there was a linear increase in applied power over time. This method was advantageous as it made it possible to test

specimens at various strain rates by simply varying the linear rate constant for power application. The relationship between the applied power and measured vertical displacement obtained experimentally with a Pt specimen is given in Figure 4.7. Figure 4.7 only displays the displacement trend up to 3 μm at which time the specimen fractured.

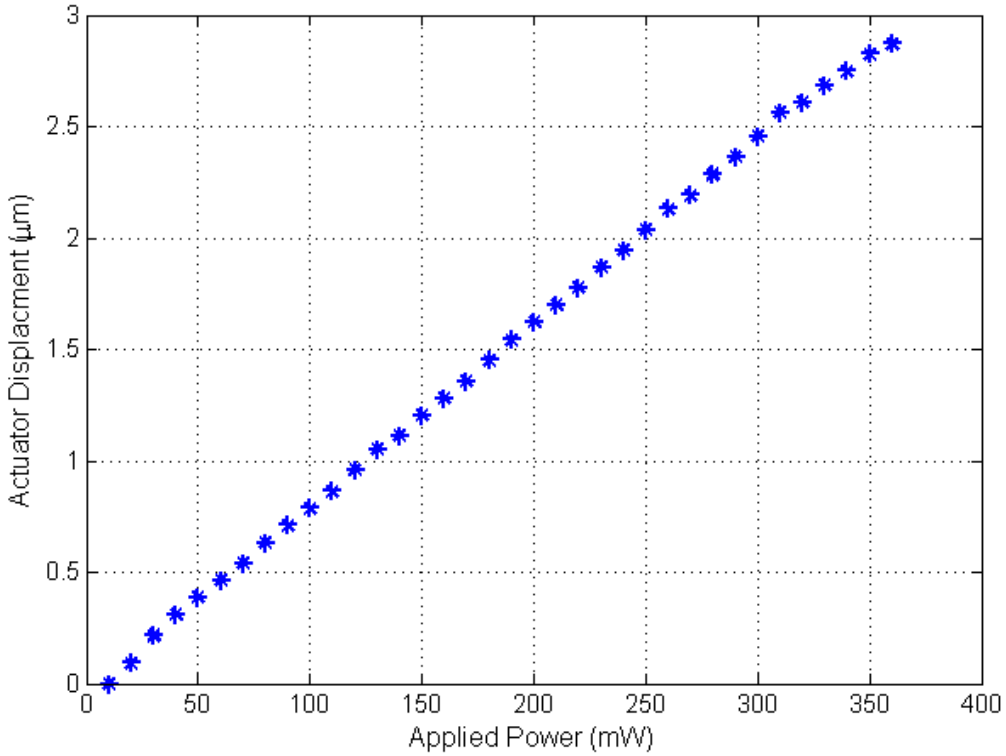

Figure 4.7: Relationship between the cascaded actuator output displacement (in μm) and applied power (mW) obtained experimentally with Pt specimen to characterize the electromechanical response [50].

A more useful characteristic curve for the device is the relationship between the applied power and work done (Figure 4.8). Output force and displacement are inversely proportional to each other. For a given temperature change the maximum force that an actuator is capable of providing is at zero output displacement and similarly for a given temperature change the maximum

displacement the actuator is capable of providing is at zero output force. But work done is a product of both instantaneous output force and output displacement and therefore characteristic of a particular set of actuator dimensions irrespective of the specimen. The curve in Figure 4.8 is nonlinear because of non-linear force provided by the load cell beam (Equation 3).

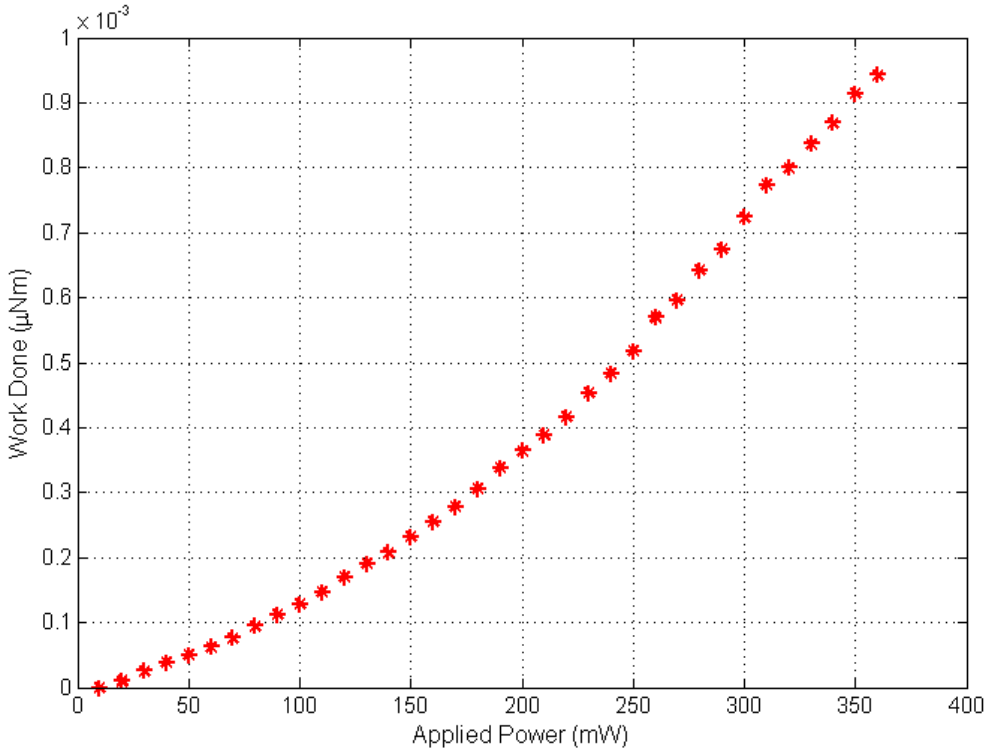

Figure 4.8: Relationship between the applied power (mW) and work done (in μNm) by cascaded thermal actuator obtained experimentally with Pt specimen to characterize the electromechanical response [50].

Chapter 5

RESULTS AND DISCUSSION

When venturing into uncharted territories with high ambitions and hopes, one always runs the risk of underestimating the magnitude of challenges and overemphasizing ones skill set and available resources. Research goals are no stranger to this phenomenon either and the author had to learn this lesson the hard way. After the author's defense of his MS thesis his confidence and ego were inflated. Upon embarking on this adventure to test the uncharted waters and tackling the most challenging of the tasks (the fabrication of a reliable test platform and repeatable mechanical testing) the author's confidence and ego were deflated and the realization of the daunting task ahead set in. After endless days and sleepless nights amid dwindling resources and breaking tools; the author finally did manage to realize this objective. To his extreme delight the results are very encouraging. Presented in the sections below are the results of the tensile tests conducted on the 75 nm, 100 nm, 250 nm and 400 nm thick platinum thin films followed by a discussion of the mechanisms that are at play that dictate the mechanical properties of these structures. It is worth noting that Platinum in bulk form has a FCC crystal structure with bulk Young's modulus of 160 GPa and the yield stress range of 125MPa – 240MPa. The fracture / yield stress observed for test samples of all film thicknesses was higher than yield strength of bulk platinum.

5.1. Results

5.1.1. 75nm thick test films

The engineering stress-strain curves for the two 75 nm thick tested films are presented in Figure 5.1. Young's modulus for the 75nm thick films was between 105GPa - 107GPa. Fracture stress for the film ranged between 530MPa – 703MPa while fracture strain was between 0.0056 – 0.0074. All samples failed in a brittle fashion (Figure 5.2).

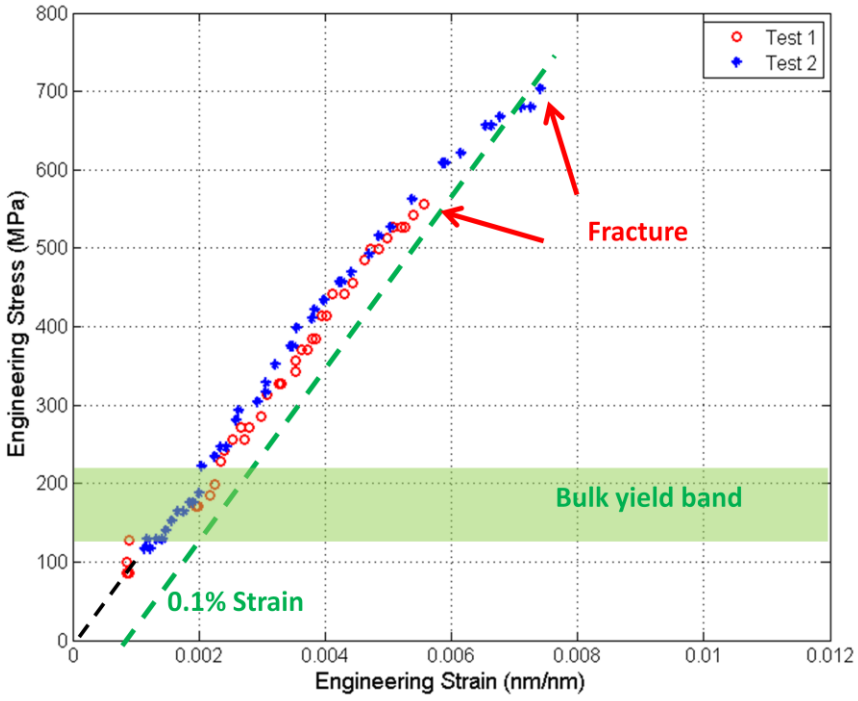

Figure 5.1: Engineering stress and strain curves for two different 75nm thick test specimens. The Young's modulus for 75nm thick test specimen was 105GPa – 107GPa.

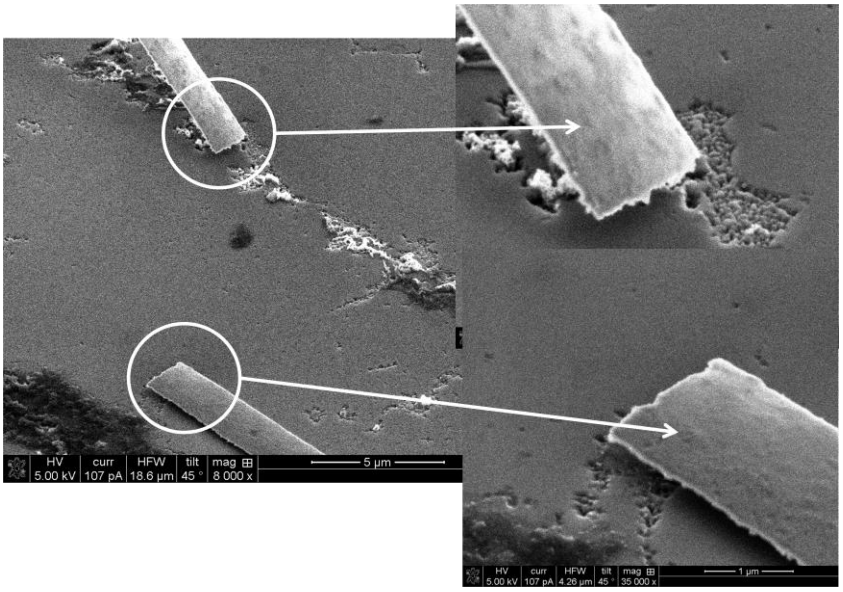

Figure 5.2: SEM images of 75nm thick test specimens showing specimen failure in brittle fashion

All 75nm thick samples fractured in a brittle fashion. The SEM image of the mating ends of a fractured 75nm thick films after the test are presented in Figure 5.2.

5.1.2. 100nm thick test films

The engineering stress-strain curves for the three 100nm thick tested films are presented in Figure 5.3. Young's modulus for the 100nm thick films was 116 +/- 2 GPa. Fracture stress and fracture strain ranged between 770 MPa – 810 MPa 0.0072 – 0.0077 respectively.

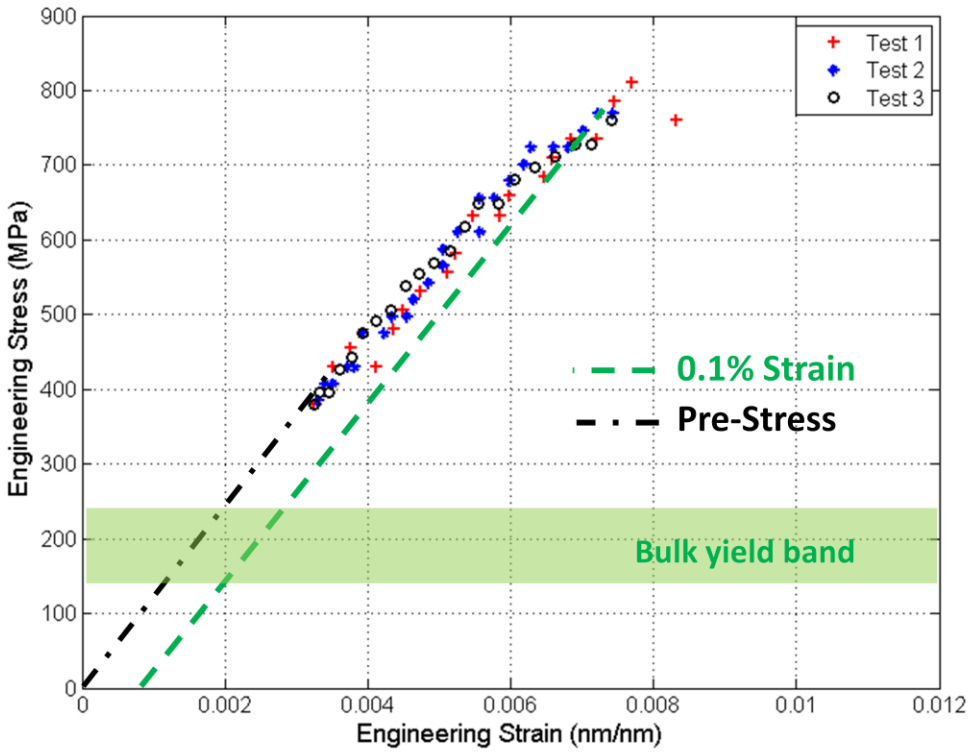

Figure 5.3: Engineering stress and strain curves for two different 100nm thick test specimens. The Young's modulus for 100nm thick test specimen was 116GPa.

All samples failed in a brittle fashion. Figure 5.4 a&b show the mating ends of a 100nm thick film after the test. The fracture is intergranular in nature with no apparent traces of plastic deformation.

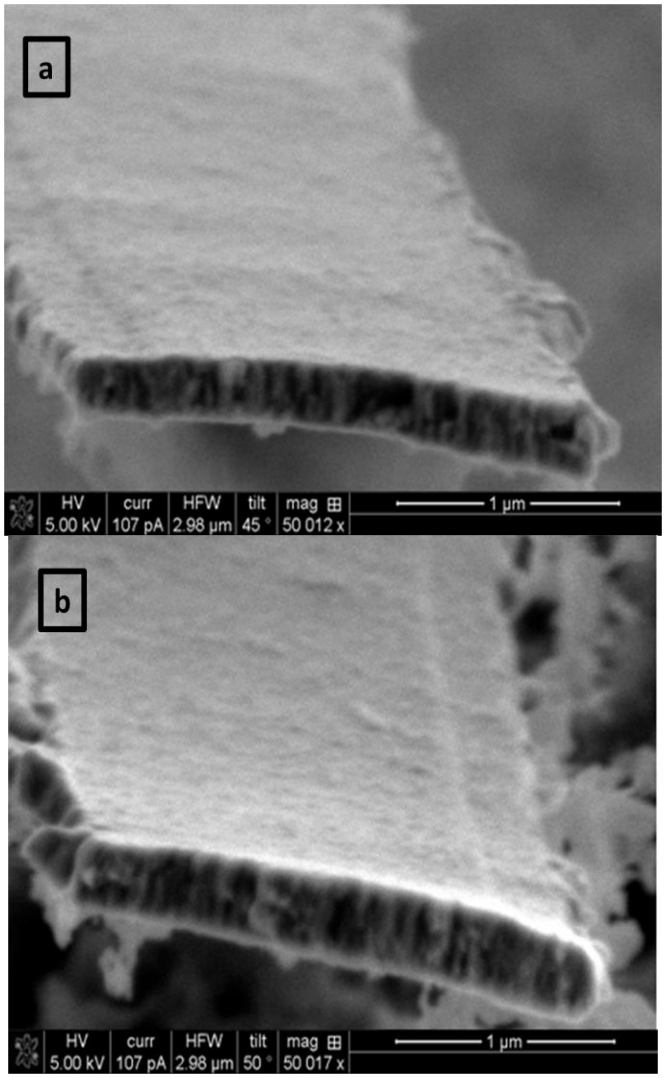

Figure 5.4: SEM images of mating surfaces of 100nm thick test specimens after fracture.

5.1.3. 250nm thick test films

The engineering stress-strain curves for the two 250 nm thick tested films are presented in Figure 5.5. Young's modulus for the 250nm thick films was between 138GPa – 142GPa for samples subjected to both tensile fracture and fatigue loading.

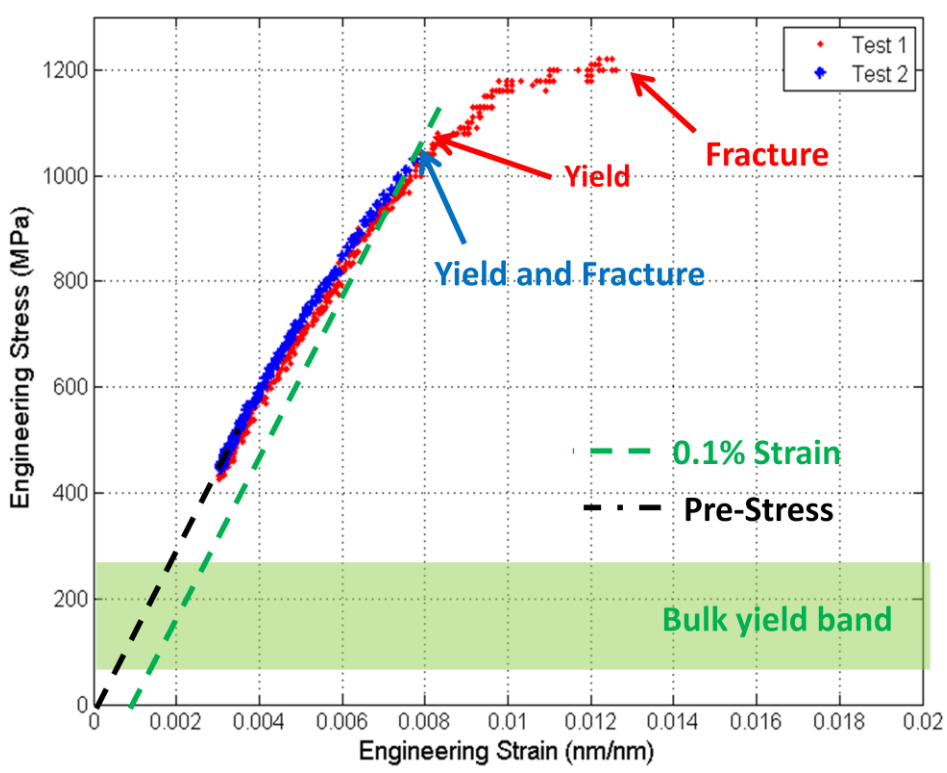

Figure 5.5: Engineering stress and strain curves for two different 250nm thick test specimens. The Young's modulus for 250nm thick test specimen was 138GPa - 142GPa

The 250nm thick films showed dual brittle/ductile behavior. One sample fractured in brittle fashion and one with limited ductility. The fracture/yield stress and strain were 1070 MPa and 0.00841 respectively. For the films that showed ductile character the ultimate tensile stress and strain were 1218 MPa and 0.0124 respectively. The fracture was intergranular in nature with intergranular cracks along the film surface. Also unlike the 75 nm and 100 nm thick films the fractured surface on 250 nm thick films are jagged indicating limited ductility.

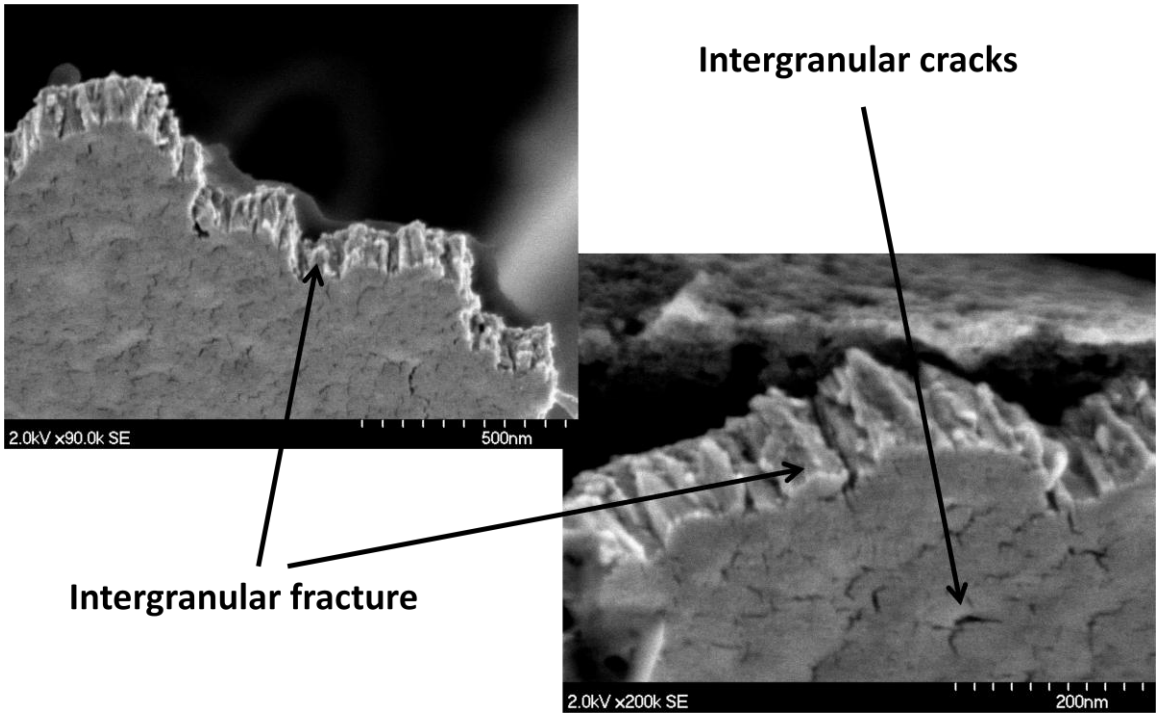

Figure 5.6: SEM images of mating surfaces of 250nm thick test specimens after fracture.

The 250nm thick films were also subjected to cyclic loading of $400 < \sigma < 1000$ MPa (within elastic limit) at strain rates of $4x10^{-4}$ ε/s, $4x10^{-5}$ ε/s and $4x10^{-6}$ ε/s. The films that displayed the brittle character failed after less than 10 cycles for all strain rates; whereas a single film with ductile character is still intact after more than 200 cycles. There was no noticeable effect of strain rate on brittle films; ductile film on the other hand displayed slight stress relaxation at slower strain rates Figure 5.7. The failed brittle films had numerous through thickness cracks on the surface along the grain boundaries.

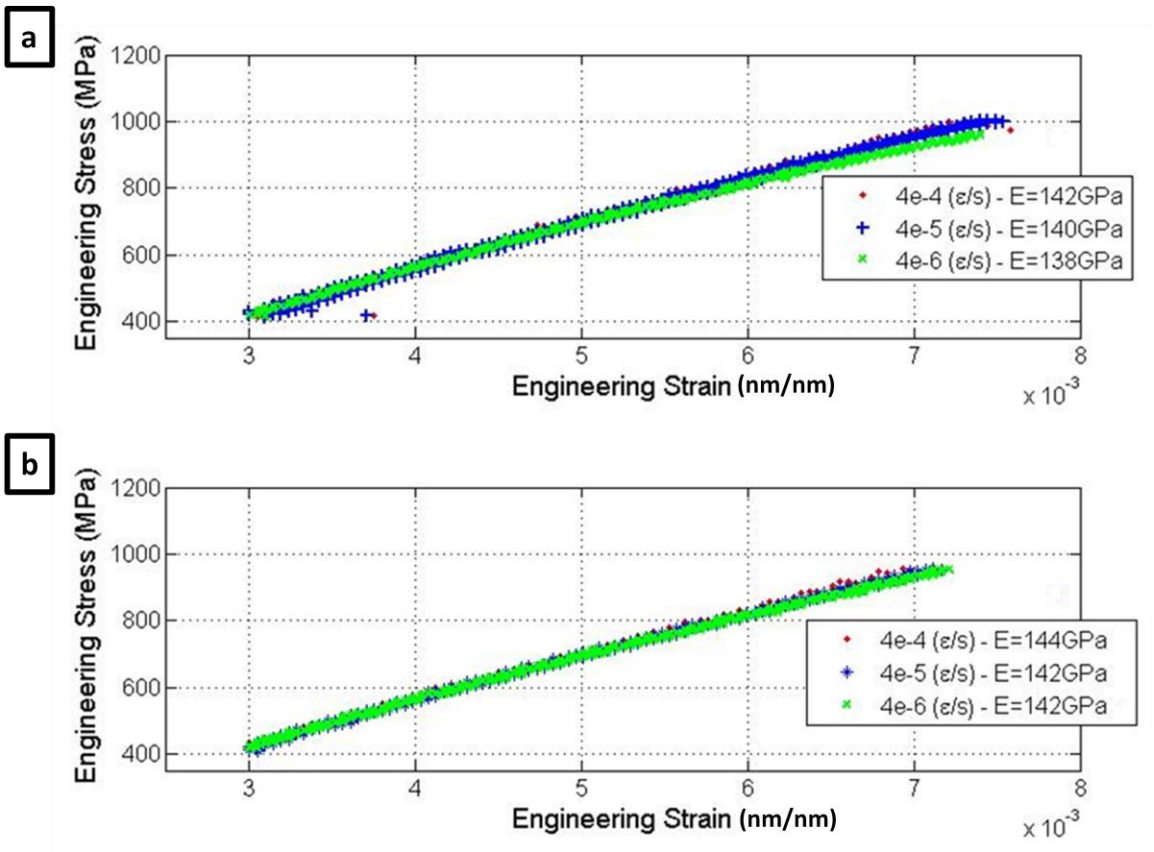

Figure 5.7: Stress-strain curve for the specimen subjected to cyclic loading and variable strain rates (a) Stress relaxation with decreasing strain rate is observed in sample with ductile character (b) No effect of strain rate with samples with brittle character

The fractured end of the samples with brittle character and subjected to the cyclic loading indicated intergranular fracture with a small cup and cone feature indicating the area where possibly smaller intergranular cracks coalesced together and grew to a critical length before catastrophic fracture (Figure 5.8).

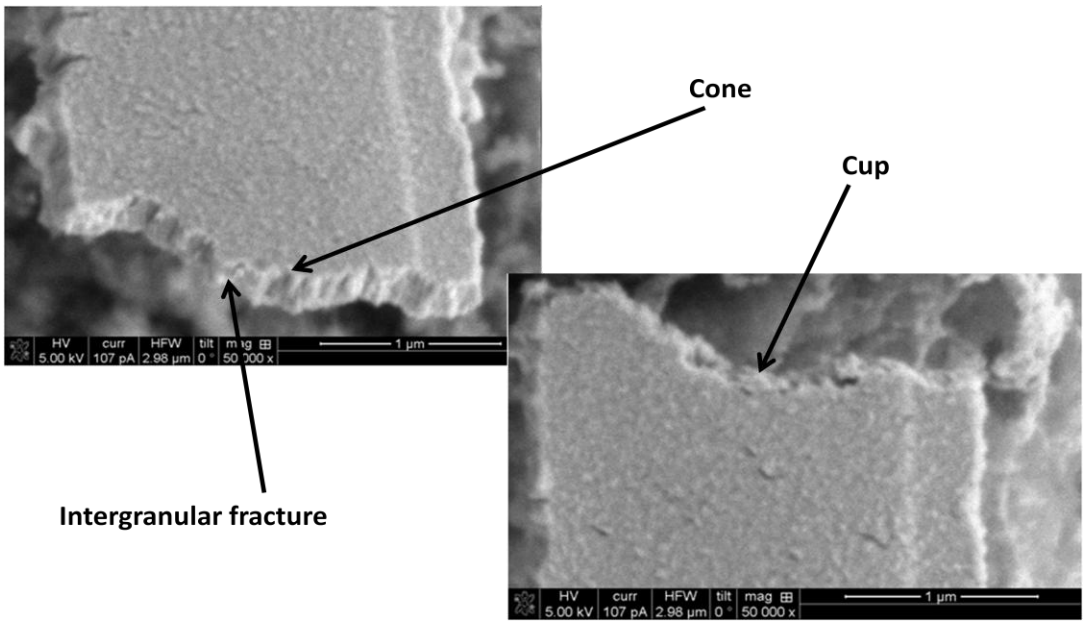

Figure 5.8: SEM images of mating ends of 250nm thick test specimens of brittle character subjected to cyclic loading. The 'cup' and 'cone' features highlight the area of intergranular crack growth to critical length.

Similar intergranular fatigue cracks were also found at numerous other locations along the length of the test film (Figure 5.9).

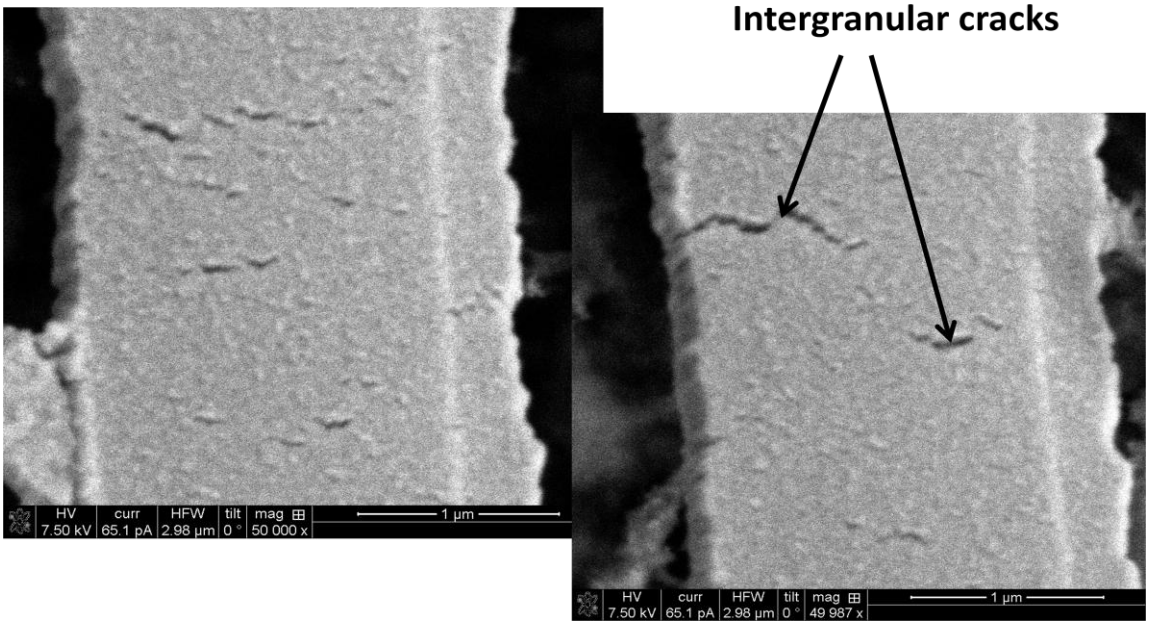

Figure 5.9: Intergranular fatigue cracks along the length of the 250nm thick test film subjected to fatigue loading.

5.1.4. 400nm thick test films

The engineering stress-strain curves for three 400 nm thick tested films are presented in Figure 5.10. The Young's modulus for the 400 nm thick films was 158 +/- 2 GPa. All 400nm thick films samples showed ductile behavior with a relatively large amount of plasticity when compared to smaller thickness samples. The yield stress and strain were approximately 1200 MPa and 0.008 respectively whereas the ultimate tensile stress and strain were ~1700 MPa and ~0.024 respectively.

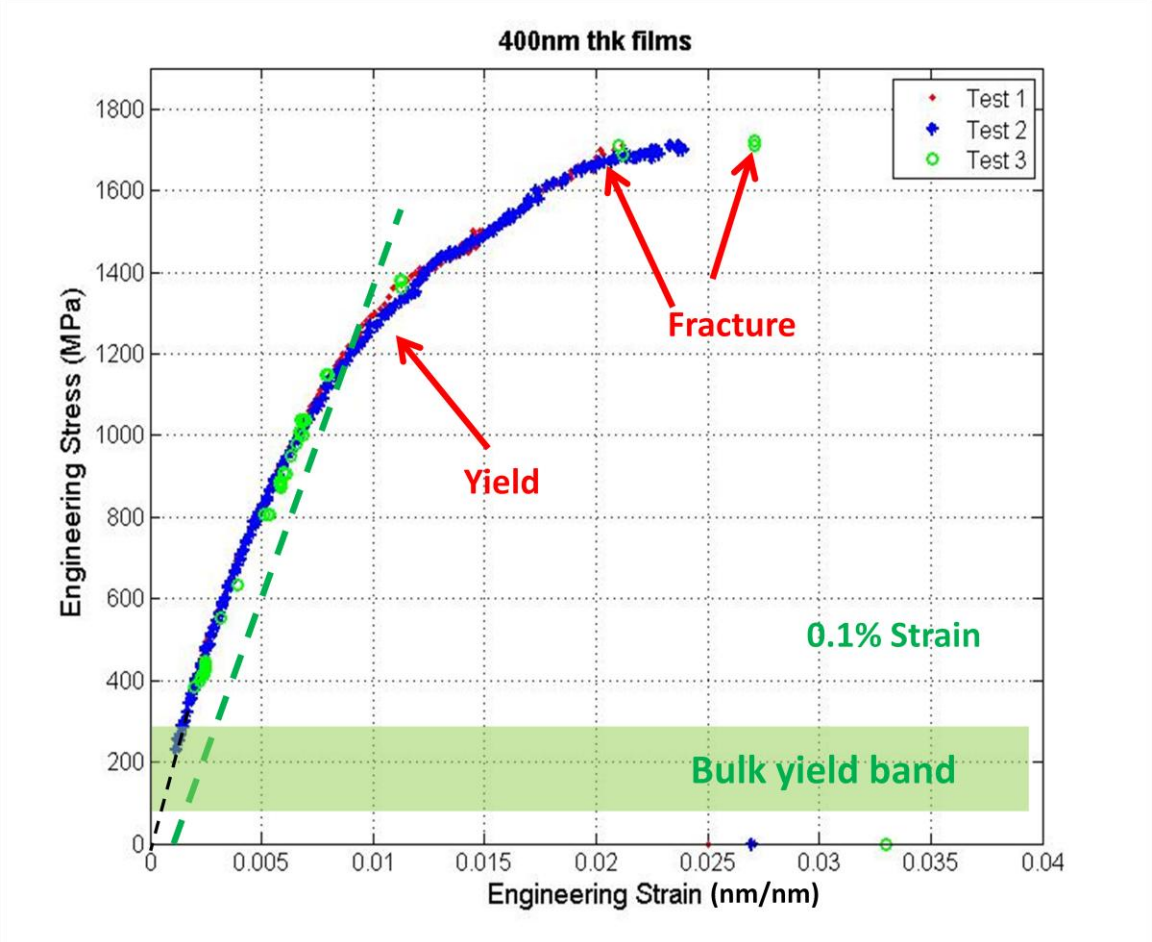

Figure 5.10: Engineering stress and strain curves for two different 400nm thick test specimens. The Young's modulus for 250nm thick test specimen is 156GPa - 160GPa

The fractured surfaces of the 400nm thick tested samples showed evidence of plastic deformation and ‘bulk-like’ features of ductility like ‘necking’ and ‘cup / cone’.

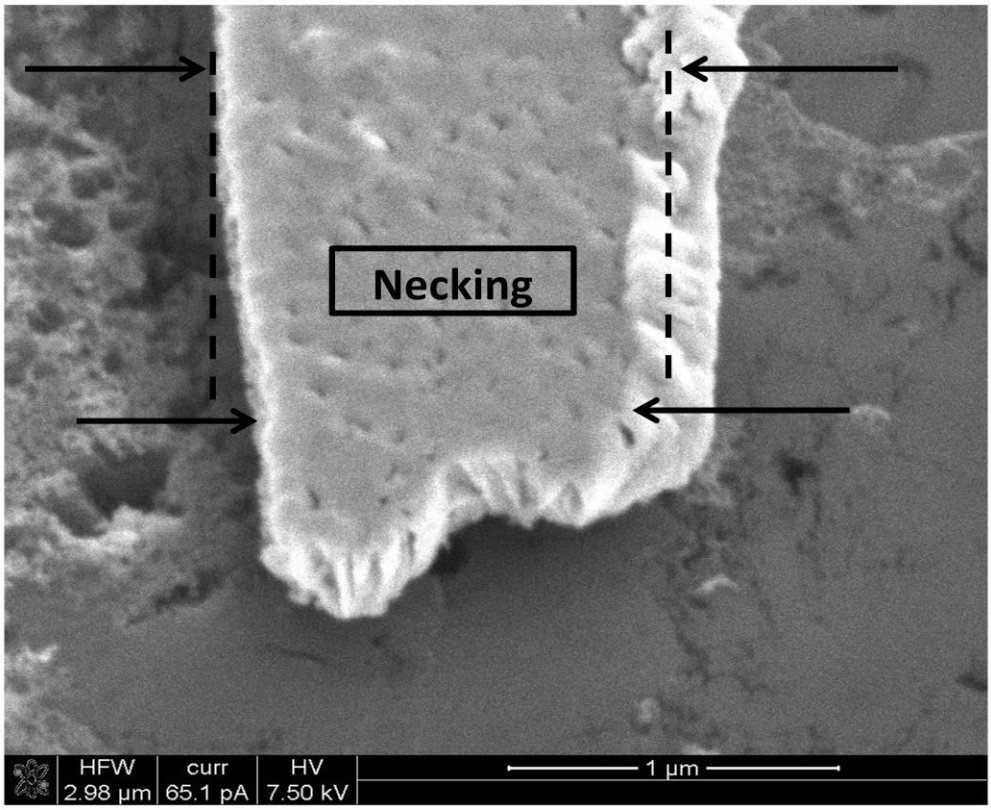

Figure 5.11: SEM image of the 400nm thick tested sample with bulk like necking in the fractured area.

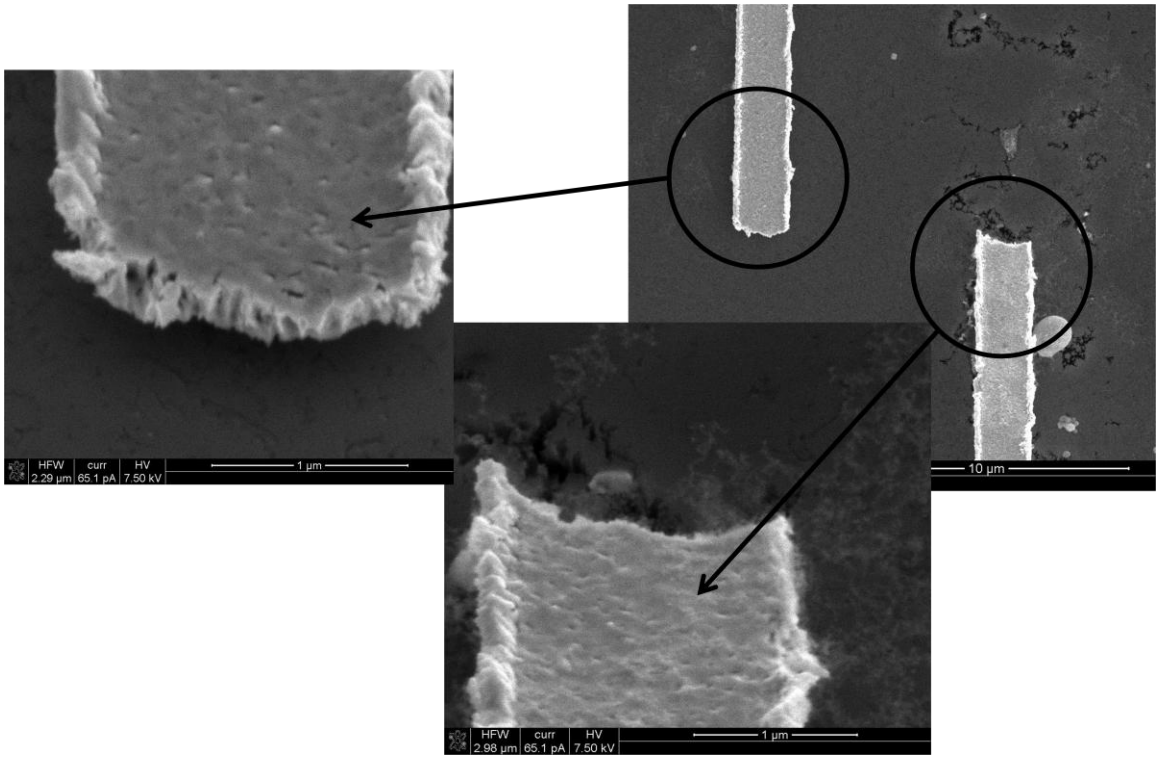

Figure 5.12: SEM images of mating ends of 400nm thick test film showing cup and cone feature.

5.2. Discussion

The results presented in the previous section can be summarized as follows: platinum freestanding films of various thicknesses 75 nm, 100 nm, 250 nm and 400 nm were tested and their mechanical behavior was recorded. The Young's moduli of 75 nm, 100 nm, 250 nm and 400 nm thick films were 105GPa, 115GPa, 140GPa and 160GPa respectively. Both the Young's modulus and the fracture/yield strength of the films increased with the increase in the film thickness. The thinner 75 nm and 100 nm films exhibited total brittle behavior. The 250 nm thick films exhibited dual brittle/limited ductile character, while 400 nm thick film was totally ductile. The findings for total brittle behavior in 75 nm and 100 nm and reduced ductility in 250 nm thick films are consistent with the findings reported by Haque and Saif [26] for free standing polycrystalline Au and

Al films of thicknesses <100 nm. The increased bulk-like plasticity in thicker 400 nm thick films was consistent with the observed on Au (1 μm thick) by Espinosa [15, 16] and very large plastic deformation on Pt by Jonnalagadda [20] (400 nm thick).

Although the grain size and film thickness effects on mechanical behavior of the free standing thin metal films has been the subject of experimental investigations in the past, the effect of cross sectional grain morphology of the thin film structure has never been reported. In all previous studies the grain sizes and film thicknesses have been reported with the underlying assumption that the cross sectional structure of the film is homogeneous however in this study no experimental evidence to support such an assumption was observed. It was observed that as the film thickness of a metal thin film structure increases it evolves as a composite structure of various grain sizes, crystallographic orientations and more importantly the grain morphologies. This existence of more than one grain morphology, its evolutionary nature and their individual effects are manifested in the form of evolving nature of the overall mechanical behavior exhibited by the thin film.

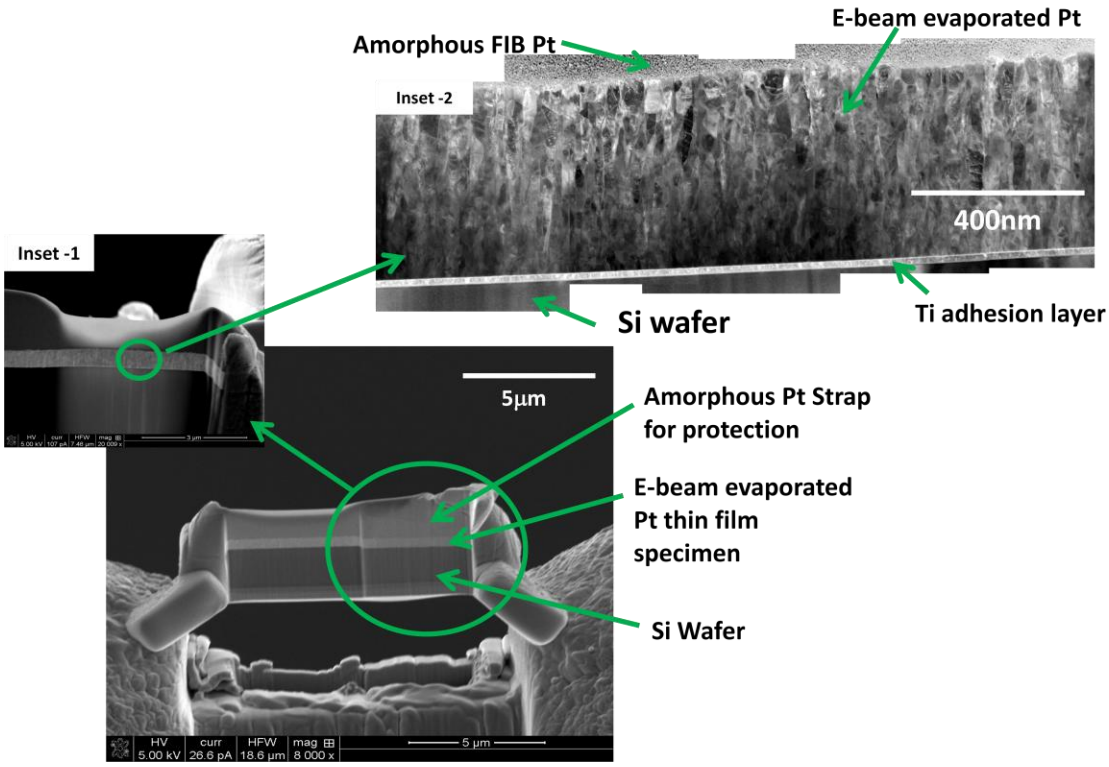

Figure 5.13: Preparation of a TEM sample for the study of the thin film cross sectional morphology using a FIB and ESEM. Inset-2 is a scanning electron transmission image of the sample.

In order to study the cross sectional morphology a cross sectional TEM sample was prepared using in situ lift-out method [64, 65] with FEI Quanta 3D FEG dual beam FIB / ESEM on a witness sample co-evaporated with 400 nm thin film specimen. Prior to the ion beam milling a strap of amorphous Pt was deposited using focused ion beam on top of the thin film sample to protect it from damage. The completed 'lift out' was then attached to a copper TEM grid using the nano manipulator and thinned out until it was transparent to the e-beam (Figure 5.13).

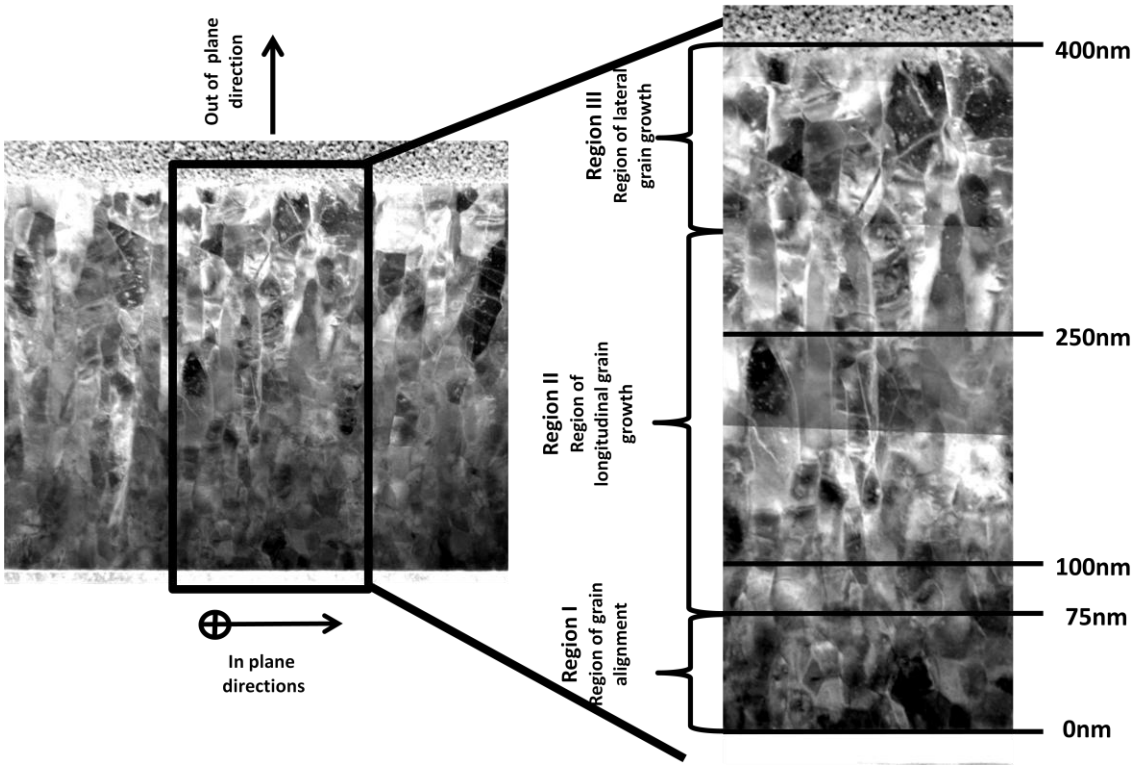

Figure 5.14: Scanning transmission electron microscope (STEM) image of the thin film cross section obtained from in situ lift sample of the 400nm thick film.

Figure 5.14 presents the transmission electron microscope (TEM) image of the thin film cross section. It can be seen in the cross sectional image that the entire cross section is completely dense and can roughly be divided into three regions; 'Region I' - region of grain alignment, 'Region II' - region of longitudinal grain growth and the 'Region III' - region of lateral grain growth. Starting at the bottom of the image the first ~80 nm of the film is comprised of a fairly equiaxed grain structure with large angled grain boundaries. This structure is representative of the composition of 75 nm thick film structure. The grain size in this region is 3-6 nm. An and average grain size of 5 +/- 2 is found over the entire 80 nm thickness and an average grain size 3 nm is found in the immediate

vicinity of the substrate on which the films have been deposited. The grain size grows as the film thickness is increased. It is likely that this structure arises due to the deposition of the platinum on a layer of titanium to promote adhesion between the silicon substrate and the platinum film, a common practice in semiconductor manufacturing. The reason that the titanium is effective in providing adhesion is because titanium diffuses into both the deposited platinum and the silicon substrate. This inter-diffusion of metals occurs during the deposition process itself and forms Ti-Pt couple diffusion zone along the grain boundaries of deposited platinum [66] which restricts the coalescence of the nucleated islands and thereby restricting the grain size in the immediate vicinity of the titanium surface Figure 5.15.

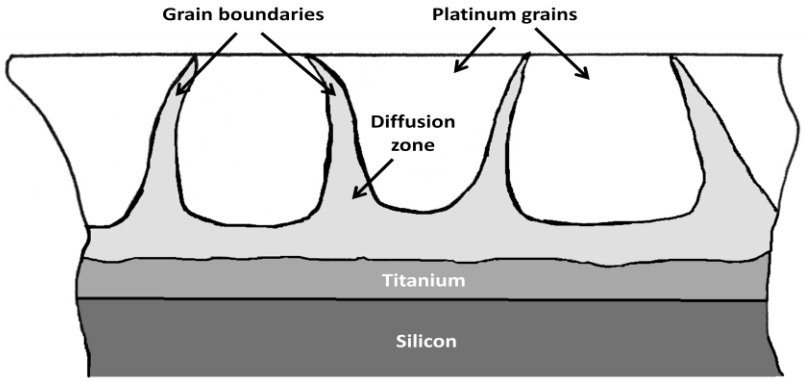

Figure 5.15: Schematic of titanium diffusion zone into platinum surface.

As the film thickness grows the effect of titanium subsides but with very low activation energy ($T/T_m < 0.1$) for surface diffusion growth is dominated by the shadowing effects resulting in a fully dense structure with very small grains and very large grain boundary volume density. With further thickening of the film the energetic considerations to reduce interface and surface energies favor

certain plane surfaces more than others [67] and the grain structure eventually evolves from random equiaxed into columnar with an out of plane (111) texture characteristic of FCC metals. This was confirmed by obtaining through thickness selected area diffraction pattern of the 100nm thick test film.

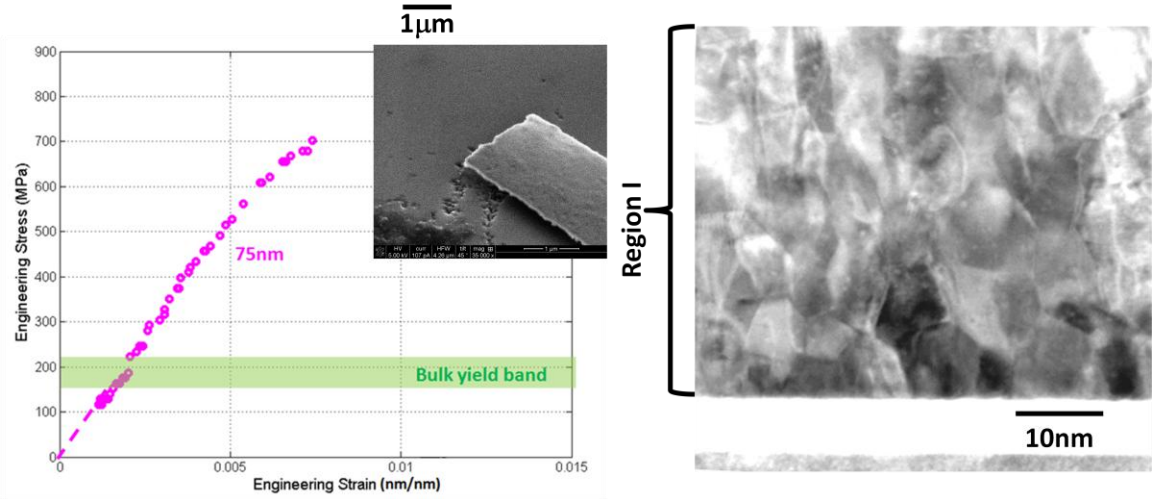

Figure 5.16: Correlating the cross sectional grain structure with the mechanical behavior of 75 nm thick film. The 75 nm thick film comprises entirely of 'Region I' type grain structure.

By correlating the mechanical behavior to the cross sectional details (Figure 5.16) it becomes clear that a 75nm thick film is mostly comprised of randomly oriented small equiaxed grain structure with very large grain boundary volume density and exhibits lower than bulk Young's modulus, and brittle failure likely due to inhomogeneous intrinsic stress distribution due large grain angles that facilitates the nucleation of cracks along the grain boundaries. The lower than bulk modulus for such structures is also consistent with other experimental and numerical studies conducted on other nanocrystalline FCC metals, most prominently Au [26, 68-70]. The Ti-Pt alloy at the substrate interface and along the grain boundaries as described previously, is eventually removed along with any remaining titanium when the films are etched in hydrofluoric acid for final

release and therefore do not contribute towards elastic strength of the film. However they likely leave behind surface cracks that run along the grain boundaries and contribute to the brittle failure.

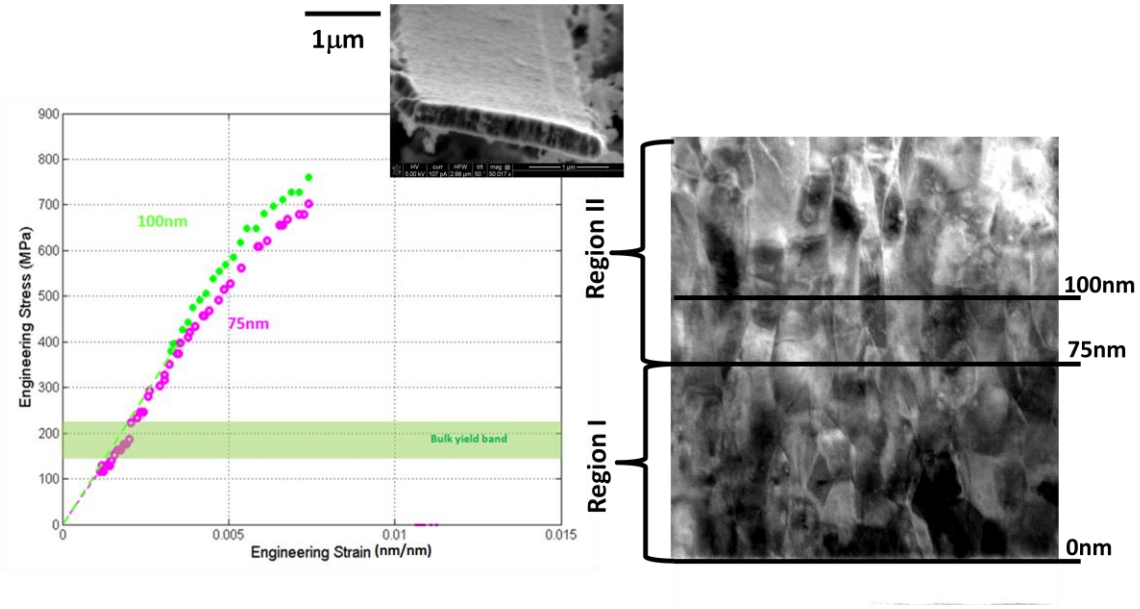

Figure 5.17: Correlating the cross sectional grain structure with the mechanical behavior of 100nm thick film. The 100nm thick film comprises both of 'Region I' and 'Region II' type grain structures which is reflected in its mechanical behavior.

The platinum films of thicknesses between 80nm-300nm comprise of both 'Region I' and 'Region II' type grain structures. 'Region II' is the region of longitudinal grain growth and the thickening of the film occurs through epitaxial growth on the aligned grain surfaces of 'Region I'. The grain growth in the direction perpendicular to the plane of the test film increases many times more than the grain growth in the plane of the film and results in a in a columnar grain structures (Figure 5.17). The measured out-of-plane grain size in this region is 100 nm – 200 nm whereas at 100 nm film thickness the in plane grain size ranges from 10 nm-15 nm. With the thickening of the film this in-plane grain size increases to 20-25 nm at 250 nm film thickness and ~30 nm at ~300 nm film

thickness. This slow but gradual in-plane grain growth indicates restructuring and rotational alignment of the grains to minimize grain boundary mismatch with the increase in the film thickness. From the grain structure mechanical behavior of this region is expected to be anisotropic with in plane strength greater than that of 'Region I'. However the columnar structure offers minimum resistance to any nucleated crack propagating longitudinally along the grain boundary.

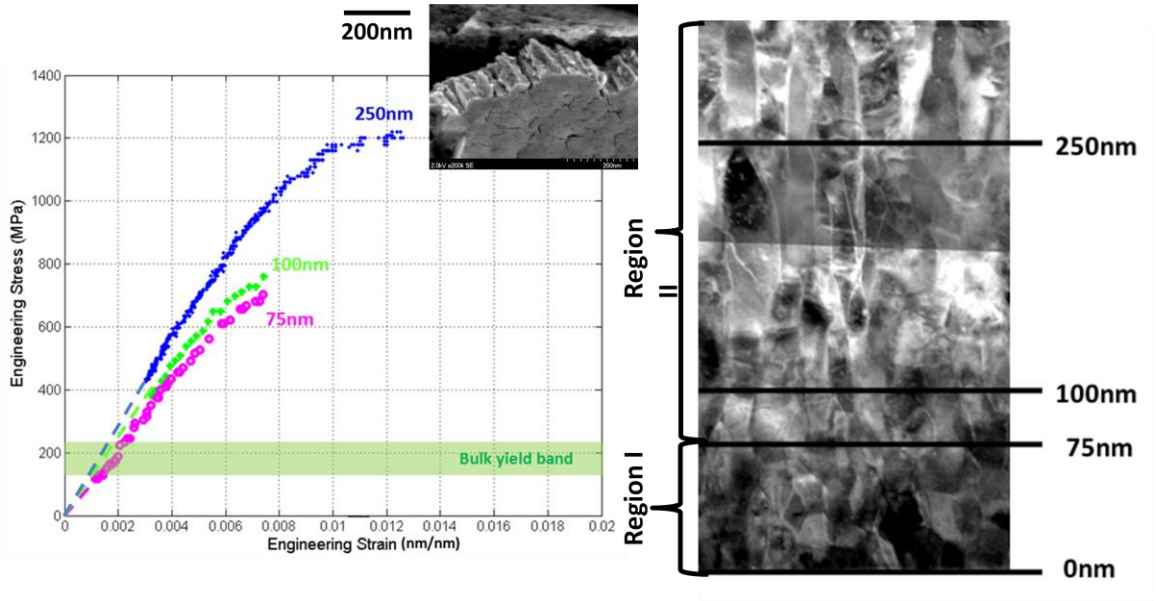

Figure 5.18: Correlating the cross sectional grain structure with the mechanical behavior of 250nm thick film. The 250nm thick film comprises both of 'Region I' and 'Region II' type grain structures with the contribution of 'Region II' higher in the 250nm thick film than in 100nm thick film.

The difference in the mechanical behavior of the 100 nm and 250 nm thick platinum films tested in this study is because of the volume fraction of 'Region II' type grain structure. To verify this, the in-plane selected area diffraction (SAD) pattern of the 100 nm and 250 nm thick platinum test films were obtained by detaching the thin film test specimen from test platform and attaching it to a TEM grid by use of nano manipulator in the environmental SEM. The film was attached to the TEM grid by use of FIB deposited Pt straps as shown in Figure

5.19. The attached the cross section of the specimen was then thinned out by FIB to the thickness (~30-50 nm), which was transparent to electron beam at 200 keV in a JEOL 2010 TEM. This approach although painfully tedious, but provided accurate localized grain size and texture information that is assumed to be the representative of the entire length of the specimen.

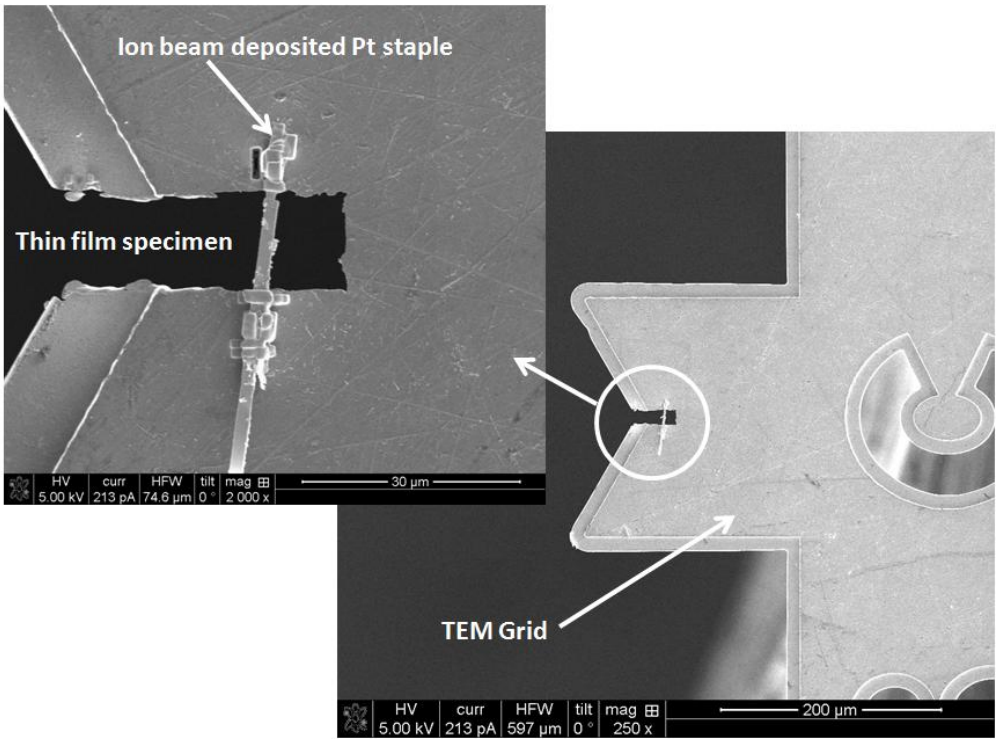

Figure 5.19: SEM picture of a thin film specimen attached to a TEM grid prior to FIB thinning for the determination of film grain size and preferred texture in TEM

The selected area diffraction patterns of 100 nm and 250 nm thick platinum test films are shown in Figure 5.20. A 100 nm thick film has a very weak out-of-plane texture but 250 nm thick films have a very strong out-of-plane texture indicating higher contribution of ‘Region II’ type out of plane grain structure. Please note that the both film thicknesses have relatively stronger [111] texture which is a characteristic of FCC metals on Si.

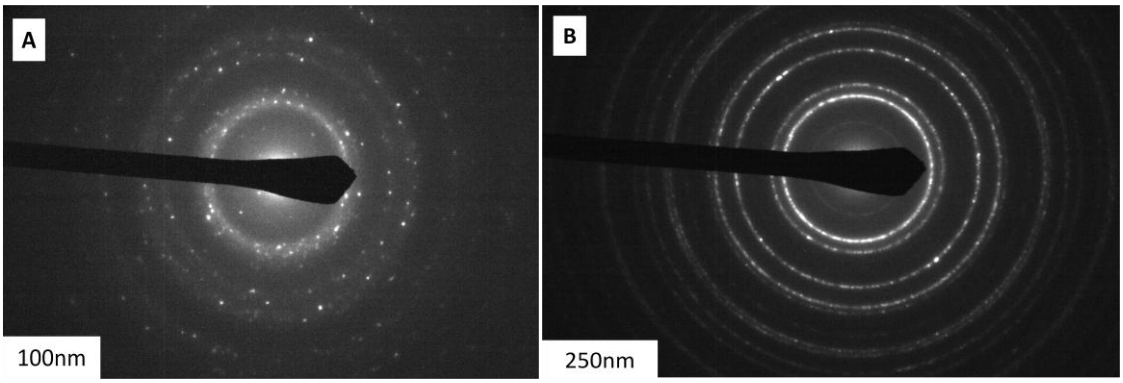

Figure 5.20: (A) In-plane selected area diffraction pattern of 100nm thick film indicating lack of strong out of plane texture. (B) In-plane selective area diffraction pattern of 250nm thick film specimen indicating development of strong out of plane [111] texture.

The 100 nm thick test films with higher volume contribution of the 'Region I' type grain structure failed in absolute brittle fashion, however the volume fraction of 'Region II' grain structure resulted in effective Young's modulus and fracture strength higher than that of 75 nm thick films. The 250nm thick films exhibited transitional behavior with some films fracturing in a brittle fashion while others fractured with limited ductility Figure 5.18. The Young's modulus for both types of thin film samples that fractured in brittle fashion and those that fractured with some degree on ductility was the same therefore it is unlikely that this behavior was caused by sample-to-sample variation of 'Region II' to 'Region I' type structure volume ratio. Since the dominant mechanical behavior is the result of dominant 'Region II' grain structure both fracture mechanisms must originate in the 'Region II'. With platinum's high stacking fault energy (~330 mJ/m^2) and nanocrystalline grain structure dislocation nucleation is extremely unlikely and deformation will only be by dislocation glide. Therefore, the limited plasticity observed in the films is most likely grain boundary mediated resulting from grain boundary sliding and/or axial grain rotation of a columnar grain structure. The

observed brittle behavior is likely the result of the volume fraction of grain boundary mismatch in longitudinal direction that acts as nucleating sites for cracks that eventually propagate first longitudinally and then later laterally along the grain boundaries resulting in ‘intergranular fracture’. This transitional brittle–ductile behavior of 250 nm thick test films can be attributed to the interplay between these two competing mechanisms. The SEM images of the fractured surfaces indicate intergranular fractures (Figure 5.6). The 250 nm thick films subjected to cyclic loading had numerous through thickness cracks on the surface along the grain boundaries (Figure 5.9); this observation is in agreement with the explanation of likely failure mechanism described above.

In film thicknesses >300 nm, the continued film thickness growth gives rise to a third region labeled as ‘Region III’ in Figure 5.21. In ‘Region III’, the longitudinal grain growth seen in ‘Region II’ slows down and is replaced by increased lateral grain growth. The in-plane grain size in this region ranges between 45 nm - 80 nm and the grains are tapered into the plane. The author hypothesizes that as the ‘Region II’ columnar grain structure grows thicker the grain boundary mismatch between two adjacent columnar grains is decreased eventually decreasing to such an extent that the two grains eventually coalesce into one large grain with high dislocation density due to the presence semi annihilated grain boundary. This mechanism explains both the tapered structure and increased lateral grain growth.

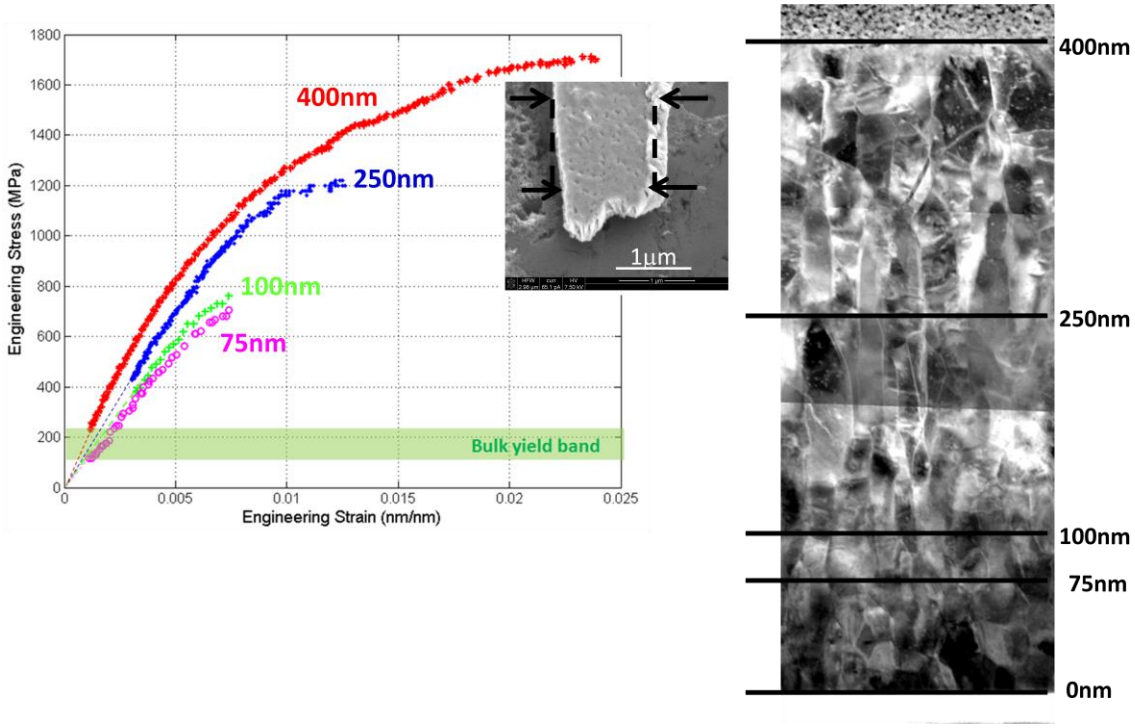

Figure 5.21: Correlating the cross sectional grain structure with the mechanical behavior of 400nm thick film. The 250nm thick film comprises of 'Region I', 'Region II' and 'Region III' type grain structures.

The mechanical behavior exhibited by 400 nm thick films tested for this study supports this hypothesis as well. Since 'Region III' is roughly the ¼ of the thickness of the test film therefore it has significant effect on the mechanical behavior of 400 nm thick film. The 400 nm thick films exhibit extremely large plastic deformation with 'bulk-like' failure features of necking (Figure 5.11) and cup and cone fracture mechanisms (Figure 5.12). This extremely large plastic deformation is most likely the result of both the intergranular and transgranular sources and motion of dislocations in 'Region III' in addition to the grain boundary meditated plasticity in 'Region II'.

The experimental and analytical observations of nanocrystalline platinum thin films suggest that these films are composites of several grain structures and the mechanical behavior results from the combined effects of all these grain

morphologies. The ductility of the film increases as the film thickness increases because the grain morphology changes and more sources of dislocations and their avenues for motion become available. Hence in exploring the mechanical behavior of the nanocrystalline metals it is important that not only the grain sizes and film thicknesses be considered but also the composite nature of cross-sectional grain morphology.

Chapter 6

CONCLUSION AND FUTURE WORK

6.1. Concluding remarks

This dissertation gives a detailed account of design, fabrication and the characterization of a MEMS thermal actuator based test platform that can be used for materials testing and characterization of the their mechanical behavior. By use of a clever design, the displacements exhibited by thermal actuators were amplified greatly and applied to the test specimen while maintaining a very low temperature gradient across the thermal test specimen. This low temperature gradient ensures that the material properties of the test specimen are not affected by the change in temperature across it. The system was designed to operate in both SEM/TEM environments and on a probe station under an optical microscope. Digital image correlation was used to obtain similar accuracy (~10 nm) for displacement measurements in both an SEM and under an optical microscope.

The developed test platform was then used to successfully test and characterize the mechanical behavior of freestanding platinum films of thicknesses 75 nm, 100 nm, 250 nm and 400 nm. Experimental evidence collected suggests that the mechanical behavior of the platinum thin films varies from completely brittle to completely ductile with transition around 250 nm thickness. Upon further investigation the dependence of mechanical behavior exhibited by the thin films on its nanocrystalline cross sectional morphology was

discovered. The mechanical behavior of nanocrystalline thin film structure has been the subject of extensive research in past but all of the focus had been on the effects of the film thickness and grain size on their mechanical behavior and the effects of thin film cross sectional morphology on the mechanical behavior of a thin film structure had never been studied previously. Presented in this dissertation is experimental evidence that these thin film structures are composite structures of various grain morphologies and the overall mechanical behavior exhibited by them is the combined effect of individual contributions of each of these grain morphologies.

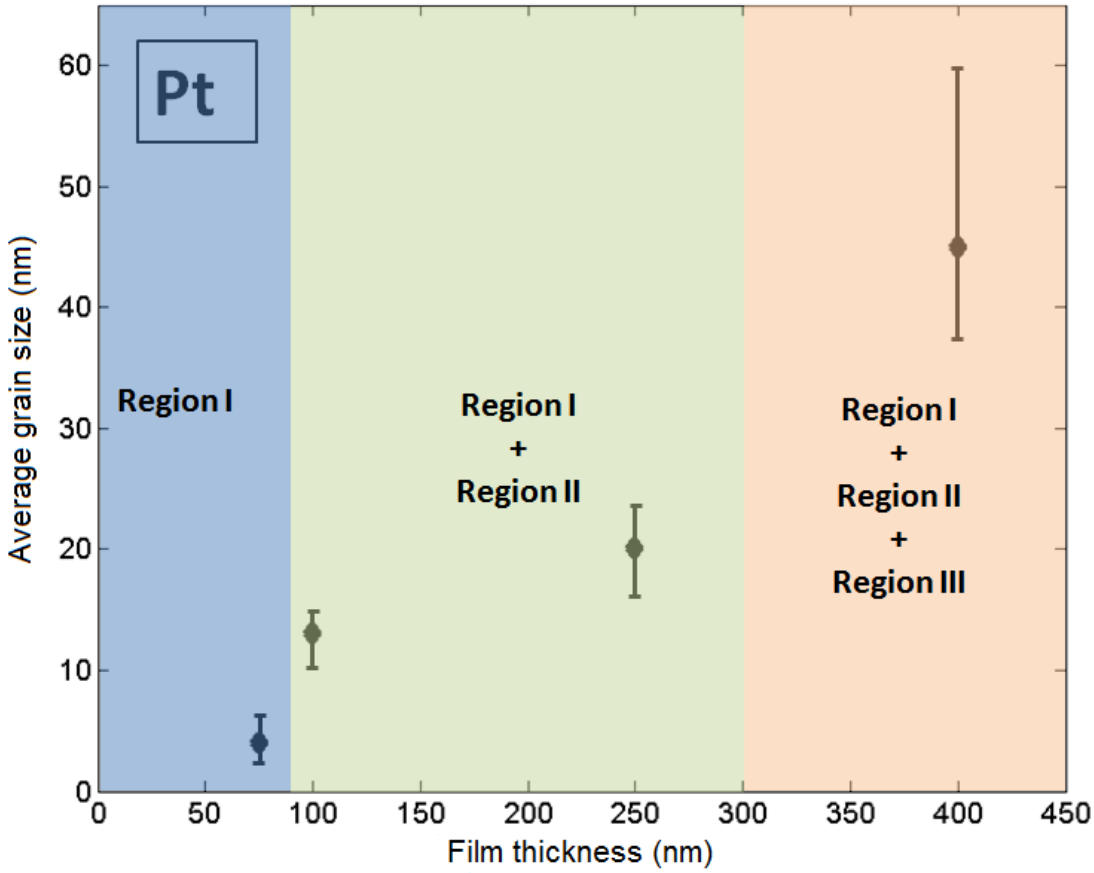

Figure 6.1: Characteristic chart for nanocrystalline Pt thin film specimens providing information on grain size, film thickness and cross sectional morphology for comparison with its mechanical behavior.

With this additional information now available the characteristic chart for the platinum freestanding thin films can be developed and it would contain not only the in-plane grain size and film thickness but also the information on its grain morphology as a function of thickness (Figure 6.1). The error bars on the average grain size in Figure 6.1 indicates the range of grain sizes observed. Since the mechanical behavior depends on the cross section grain morphology therefore Figure 6.1 is a better predictor of the thin film mechanical behavior in terms of its ductile / brittle behavior than the chart presented in Figure 1.1 (reproduced here as Figure 6.2).

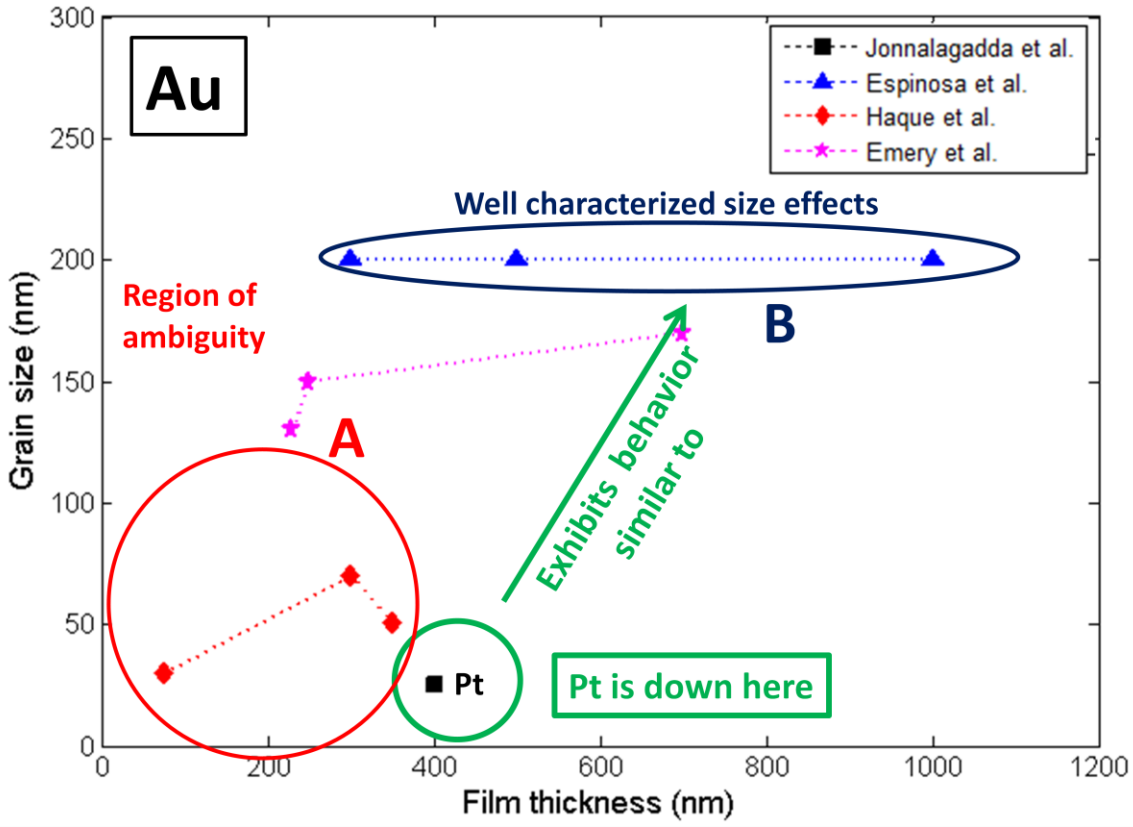

Figure 6.2: Relationship between grain size and film thickness for nanocrystalline Au thin film specimens from literature

It can now be explained as to why there was an ambiguity in establishing a relationship between the mechanical properties and grain size effects for Au film of < 400 nm thickness from the information available in the literature. This ambiguity can be attributed to the lack of available information on the evolution of the Au film's cross sectional morphology. In the absence of this information it remains impossible to isolate the effects of grain size increase on mechanical behavior from the effects of change in the grain morphology. Platinum thin films are able to display huge plastic deformations and bulk like plasticity despite their ultra fine grain size because their cross sectional grain morphology and their volume fractions.

6.2. Directions for future work

6.1.1. Mechanical properties by design

One of the greatest hurdles in the design of efficient and reliable MEMS devices is the unknown nature of material properties at this scale. With the discovery of new information in this dissertation it is potentially possible to tailor and design these properties by controlled alteration of cross sectional grain morphology by changing the deposition conditions. Movchan and Demchishin [71] developed the Structural Zone Models (SZMs) in 1969 describing the grain morphology based on the deposition conditions. Variations in the representations of Structural Zone Diagrams (SZDs) have been suggested since then. The present day representations of the SZD have 3 axes that are representative of thickness, temperature and processing conditions. The thickness axis allows for the visualization of crystal structure as growth progresses from the substrate

(bottom) to the top surface (z-axis in Figure 6.3). The temperature of the substrate during deposition is usually normalized to the melting temperature of the material (T_s/T_m). The third axis is commonly added to represents many different processing parameters. The one in Figure 6.3 deals with a normalized energy unit that could represent the chamber pressure. Another such representation could be that of the kinetic energy of bombarding particles from a plasma as in sputter etching [72].

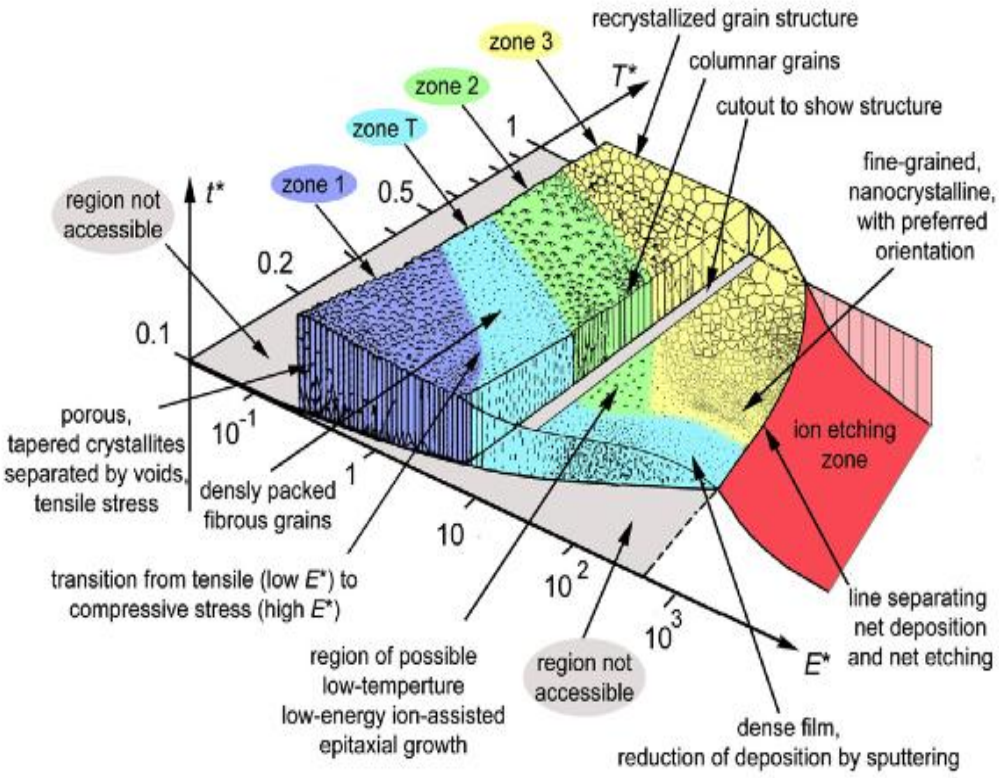

Figure 6.3: The Structure Zone Diagram (SZD) for a sputtered thin film [72]

The SZD in Figure 6.3 displays 4 zones; the first zone, Zone 1 ($T_s/T_m < 0.2$) displays porous crystallites that have a high density of dislocations. This type of structure is attributed to low adatom mobility. The second zone, Zone T ($0.2 < Ts/Tm < 0.4$), is a transition zone where the Zone 1 structure is transforming into

densely packed fibrous grains due to enhanced surface diffusion. The third zone, Zone 2 ($0.4 < Ts/Tm < 0.5$), is a fully columnar structure and Zone 3 ($Ts/Tm > 0.5$) has a more equiaxed structure with nanocrystalline grains tending towards the lower part of this zone and larger grains (due to grain growth during deposition) at the upper end of this range. Note that Figure 6.3 is for a sputtered film. SZD's for evaporated films are quite similar, but lack Zone T, and then Zone 1 has $T_s/T_m < 0.3$ and Zone 2 has $0.3 > T_s/T_m < 0.5$. By varying the substrate temperature or processing parameters various areas of the SZDs can be accessed and since the mechanical properties of the films depend on their cross sectional morphology, their mechanical behavior could potentially be designed and tailor to the required specifications.

6.1.2. Localized stress and strain

The mechanical behavior of the films described in this dissertation is their overall behavior. However, not much information is available about their localized behavior at the site of crack propagation or fracture. Crystallographic information on the film surface including the texture and the grain outline could be obtained by collecting the electron back scatter diffraction (EBSD) data at various stress and strain states. Digital image correlation can later be performed on this crystallographic information to identify any grain growth, rotation, motion, nature and mode of fracture propagation under the application of uniaxial stress. Due to the ultra fine grain sizes at this scale it would be best if the EBSD data is collected in TEM rather than the SEM. Since the e-beam spot size in TEM is much smaller than that in the SEM the crystallographic information collected will

be more accurate. The current design of the test platform would require modifications to the fabrication process to allow a through device die via for e-beam transmission in TEM.

BIBLIOGRAPHY

[1] K. E. Petersen, "Silicon as a mechanical material," *Proceedings of the Ieee,* vol. 70, pp. 420-457, 1982.

[2] R. S. Muller, "From ics to microstructure: Materials and technologies," presented at the IEEE Micro Robots and Teleoperators Workshop, Hyannis, Mass., 1987.

[3] M. Mehregany, K. J. Gabriel, and W. S. N. Trimmer, "Integrated fabrication of polysilicon mechanisms," *IEEE transactions on Electron Devices,* vol. 35, pp. 719 - 723, 1988.

[4] T. A. Lober and R. T. Howe, "Surface micromachining processes for electrostatic microactuator fabrication," presented at the Technical digest, IEEE solid state sensors and actuators workshop, Hilton Head Island, SC., 1988.

[5] K. Hjort, J. A. Schweitz, and B. Hok, "Bulk and surface micromachining of gaas structures " presented at the Technical digest, IEEE Micro Electro Mechanical Systems Workshop, Napa Valley, CA, 1990.

[6] R. E. Oosterbroek, T. S. J. Lammerink, J. W. Berenschot, G. J. M. Krijnen, M. C. Elwenspoek, and A. vandenBerg, "A micromachined pressure / flow-sensor," *Sensors and Actuators A: Physical,* vol. 77, pp. 167-177, 1999.

[7] P. G. Slade, *Electrical contacts: Principles and applications*: Marcel Dekker, New York, 1999.

[8] L. Chen, H. Lee, Z. J. Guo, N. E. McGruera, K. W. Gilbert, S. Mall, K. D. Leedy, and G. G. Adams, "Contact resistance study of noble metals and alloy films using a scanning probe microscope test station," *Journal of applied physics,* vol. 102, 2007.

[9] H. Lee, R. A. Coutu, S. Mall, and K. D. Leedy, "Characterization of metal and metal alloy films as contact materials in mems switches," *Journal Micromechanics and Microengineering,* vol. 16, pp. 557-563, 2006.

[10] H. Kwon, D.-J. Choi, J.-H. Park, H.-C. Lee, Y.-H. Park, Y.-D. Kim, H.-J. Nam, Y.-C. Joo, and J.-U. Bu, "Contact materials and reliability for high power rf-mems switches," presented at the IEEE 20th International conference on Micro Electro Mechanical Systems, Hyogo, Japan, 2007.

[11] P. Ekkels, X. Rottenberg, R. Puers, and H. A. C. Tilmans, "Evaluation of platinum as a structural thin film material for rf-mems devices," *Journal of Micromechanics and Microengineering,* vol. 19, 2009.

[12] H. Huang and F. Spaepen, "Tensile testing of free standing cu, ag, and al thin films and ag/cu multilayers," *Acta Materialia,* vol. 48, pp. 3261-3269, 2000.

[13] A. J. Kalkman, A. H. Verbruggen, and C. A. M. Janssen, "Young's modulus measurement and grain boundary sliding in free standing thin metal films," *Applied Physics Letters,* vol. 78, pp. 2673-2675, 2001.

[14] R. P. Vinci and J. J. Vlassak, "Mechanical behavior of thin films," *Annual Review of Material Science,* vol. 26, pp. 431-436, 1996.

[15] H. D. Espinosa, B. C. Prorok, and M. Fischer, "A novel method for measuring elasticity, plasticity and fracture of thin films and mems materials," *Journal of Mechanics and Physics of Solids,* vol. 51, pp. 47-67, 2003.
[16] H. D. Espinosa, B. C. Prorok, and B. Peng, "Plasticity size effects in free standing submicron polycrystalline fcc films subjected to pure tension," *Journal of Mechanics and Physics of Solids,* vol. 52, pp. 667-689, 2004.
[17] E. Arzt, "Size effects in materials due to microstructural and dimensional constraints: A comparative review," *Acta Materialia,* vol. 46, pp. 5611-5626, 1998.
[18] E. Arzt, G. Dehm, P. Gumbsch, O. Kraft, and D. Weiss, "Interface controlled plasticity in metals: Dispersion hardening and thin film deformation," *Progress in Materials Science,* vol. 46, pp. 283–307, 2001.
[19] F. Spaepen, "Interfaces and stresses in thin films," *Acta Materialia,* vol. 48, pp. 31-42, 2000.
[20] K. N. Jonnalagadda, I. Chasiotis, S. Yagnamurthy, J. Lambros, J. Pulskamp, R. Polcawich, and M. Dubey, "Experimental investigation of strain rate dependence of nanocrystalline pt films," *Experimental Mechanics,* vol. 50, pp. 25-35, 2010.
[21] M. C. Salvadori, I. G. Brown, A. R. Vaz, L. L. Melo, and M. Cattani, "Measurement of the elastic modulus of nanosructured gold and platinum films," *Physical Review B,* vol. 67, 2003.
[22] J. A. Thornton, "High rate thick film growth," *Annual Review of Materials Science,* vol. 7, pp. 236-260, 1977.
[23] J. Sanchez and E. Arzt, "Effects of grain orientation on hillock formation and grain growth in aluminum films on silicon substrate," *Scripta metallurgica et materialia,* vol. 27, pp. 285-290, 1992.
[24] C. V. Thompson, "The yield stress of polycrystalline thin films," *Journal of Material Research,* vol. 8, pp. 237-238, 1993.
[25] R. R. Keller, J. M. Phelps, and D. T. Reed, "Tensile and fracture behavior of free standing copper films," *Material Science and Engineering: A,* vol. 214, pp. 42-52, 1996.
[26] M. A. Haque and M. T. A. Saif, "Deformation mechanisms in free standing nanoscale films: A quantitative in situ transmision electron microscope study," *Proceedings of the National Academy of Sciences,* vol. 101, pp. 6335-6340, 2004.
[27] M. A. Haque and M. T. A. Saif, "In-situ tensile testing of nano-scale specimens in sem and tem," *Experimental Mechanics,* vol. 42, pp. 123-128, 2002.
[28] B. A. Samuel and M. A. Haque, "Room temperature relaxation of free standing nanocrystalline gold film," *Journal of Micromechanics and Microengineering,* vol. 16, pp. 929-934, 2006.
[29] H. D. Espinosa, S. Berbenni, M. Panico, and K. Schwarz, "An interpretation of size-scale plasticity in geometrically confined systems," *Proceedings of the National Academy of Sciences,* vol. 102, pp. 16933-16938, 2005.

[30] Z. W. Shan, J. M. K. Wiezorek, E. A. Stach, D. M. Follstaedt, J. A. Knapp, and S. X. Mao, "Dislocation dynamics in nanocrystalline nickel," *Physical Review Letters,* vol. 98, 2007.
[31] Z. W. Shan, E. A. Stach, J. M. K. Wiezorek, J. A. Knapp, D. M. Follstaedt, and S. X. Mao, "Grain boundary mediated plasticity in nanocrystalline nickel," *Science,* vol. 305, pp. 654-657, 2004.
[32] Z. W. Shan, E. A. Stach, J. M. K. Wiezorek, J. A. Knapp, D. M. Follstaedt, and S. X. Mao, "Response to comment on "grain boundary mediated plasticity in nanocrystalling nickel"," *Science,* vol. 308, 2005.
[33] J. Rajagopalan, J. H. Han, and M. T. A. Saif, "Plastic deformation recovery in freestanding nanocrystalline aluminum and gold thin films," *Science,* vol. 315, pp. 1831-1834, 2007.
[34] K. Abbas, Z. C. Leseman, and T. J. Mackin, "Ultra low cycle fatigue of axisymmetric freestanding nanoscale gold films," in *Proceedings of ASME International Mechanical Engineering Congress and Exposition* Seattle, Washington, 2007.
[35] Y. Wei, A. F. Bower, and H. Gao, "Recoverable creep deformation due to hetrogeneous grain boundary diffusion and sliding," *Scripta Materialia,* vol. 57, pp. 933-936, 2007.
[36] Y. Wei, A. F. Bower, and H. Gao, "Recoverable creep deformation and trasient local stress concentration due to hetrogeneous grain boundary diffusion and sliding in polycrystalline solids," *Journal of Mechanics and Physics of Solids,* vol. 56, pp. 1460-1483, 2008.
[37] X. Li, Y. Wei, W. Yang, and H. Gao, "Competing grain boundary and dislocation mediated mechanisms in plastic strain recovery in nanocrystalline aluminum," *Proceedings of the National Academy of Sciences,* vol. 106, pp. 16108-16113, 2009.
[38] J. Rajagopalan, J. H. Han, and M. T. A. Saif, "Bauschinger effect in unpassivated free standing nanoscale metals films," *Scripta Materialia,* vol. 59, pp. 734-737, 2008.
[39] H. D. Espinosa, Y. Zhu, and N. Moldovan, "Design and operation of a mems based material testing system for nanomechanical characterization," *Journal of Microelectromechanical Systems,* vol. 16, 2007.
[40] I. Chasiotis and W. G. Knauss, "A new microtensile tester for the study of mems material with the aid of atomic force microscopy," *Experimental Mechanics,* vol. 42, pp. 51-57, 2002.
[41] R. D. Emery and G. L. Povirk, "Tensile behavior of free standing gold films - part i: Coarse grained films," *Acta Materialia,* vol. 51, pp. 2067-2078, 2003.
[42] R. D. Emery and G. L. Povirk, "Tensile behavior of free standing gold film - part ii: Fine grained films," *Acta Materialia,* vol. 51, pp. 2079-2087, 2003.
[43] K. N. Jonnalagadda, N. Karanjgaokar, I. Chasiotis, J. Chee, and D. Peroulis, "Strain rate sensitivity of nanocrystalline au films at room temperature," *Acta Materialia,* vol. 58, pp. 4674-4684, 2010.

[44] Mohammad Naraghi and I. Chasiotis, "Novel method for mechanical characterization of polymeric nanofibers," *Review of scientific instruments,* vol. 78, 2007.
[45] Mohan Prasad Manoharan, Sandeep Kumar, M. A. Haque, Ramakrishnan Rajgopalan, and H. C. Foley, "Room temperature amorphous to nanocrystalline transformation in ultra thin films under tensile stress: An in-situ tem study," *Nanotechnology,* vol. 21, 2010.
[46] Yong Zhu and H. D. Espinosa, "An electromechanical material testing system for in situ electron microscopy and applications," *Proceedings of the National Academy of Sciences,* vol. 102, pp. 14503-14508, 2005.
[47] M. A. Haque and M. T. A. Saif, "Microscale materials testing using mems actuators," *Journal of Microelectromechanical Systems,* vol. 10, pp. 146-152, 2001.
[48] Yong Zhu, Alberto Corriliano, and H. D. Espinosa, "A thermal actuator for nanoscale in situ microscopy testing: Design and characterization," *Journal of Micromechanics and Microengineering,* vol. 16, pp. 242-253, 2006.
[49] S. Kumar, D. Zhuo, D. E. Wolfe, J. A. Eades, and M. A. Haque, "Length scale effecs on fracture of multilayer," *Scripta Materialia,* vol. 63, pp. 196-199, 2010.
[50] K. Abbas, S. Alaie, and Z. C. Leseman, "Design and characterization of low temperature gradient and large displacement thermal actuators for in-situ mechanical testing of nano-scale materials," *Journal Micromechanics and Microengineering,* vol. 22, p. 125027, 2012.
[51] Y. B. Gianchandani and K. Najafi, "Bent-beam strain sensors," *Journal of Microelectromechanical Systems,* vol. 5, pp. 52-58, 1996.
[52] Long Que, Jae-Sung Park, and Y. B. Gianchandani, "Bent-beam electrothermal actuators - part i: Single beam and cascaded devices," *Journal of Microelectromechanical Systems,* vol. 10, pp. 247-254, 2001.
[53] Jae-Sung Park, Larry L. Chu, Andrew D. Oliver, and Y. B. Gianchandani, "Bent-beam electrothermal actuators—part ii: Linear and rotary microengines," *Journal of Microelectromechanical Systems,* vol. 10, pp. 255-262, 2001.
[54] K. Abbas, Z. C. Leseman, and T. J. Mackin, "A traceable calibration procedure for mems- based load cells," *International Journal of Mechanics and Materials in Design,* vol. 4, pp. 383-389, 2008.
[55] Z. C. Leseman and T. J. Mackin, "Indentation testing of axisymmetric freestanding nanofilms using a mems load cell," *Sensors and Actuators A: Physical,* vol. 134, pp. 264-270, 2007.
[56] R. R. Frisch-Fay, *Flexible bars*. New South wales, Australia: Butterworths & Co. Limited, 1962.
[57] W. Young, *Roark's formulas for stress and strain*, 6th ed., 1989.
[58] Y. Okada and Y. Tokumarau, "Precise determination of lattice parameter and thermal expansion coefficient of silicon between 300 and 1500 k," *Journal of applied physics,* vol. 56, pp. 314-420, 1984.

[59] M. Chiao and L. Lin, "Self-buckling of micromachined beams under resistive heating," *Journal of Microelectromechanical Systems,* vol. 9, pp. 149-151, 2000.
[60] K. Abbas, " Design fabrication and calibration of mems actuators for in-situ materials testing," Masters Thesis, Department of Mechanical Engineering, The University of New Mexico, 2008.
[61] F. Larmer and A. Schilp, "Method for anisotropically etching silicon," DE 4241045, US 5501893 and EP 625285, 1992.
[62] G. Vendroux and W. G. Knauss, "Submicron deformation field measurements: Part 2. Improved digital image correlation," *Experimental Mechanics,* vol. 38, pp. 86-92, 1998.
[63] B. Serio, J. J. Hunsinger, and B. Cretin, "In-plane measurements of microelectromechanical systems vibrations with nanometer resolution using the correlation of synchronous images," *Review of scientific instruments,* vol. 75, 2004.
[64] R. M. Langford and C. Clinton, "In situ lift-out using a fib-sem system," *Micron,* vol. 35, pp. 607-611, 2004.
[65] L. A. Giannuzzi and F. A. Stevie, "A review of focused ion beam milling techniques for tem specimen preparation," *Micron,* vol. 30, pp. 197-204, 1999.
[66] T. C. Tisone and J. Drobek, "Diffusion in thin film ti-au, ti-pd and ti-pt couples," *Vacuum Science and Technology,* vol. 9, pp. 271-275, 1971.
[67] C. V. Thompson and R. Carel, "Texture development in polycrystalline thin films," *Material Science and Engineering: B,* vol. 32, pp. 211-219, 1995.
[68] H. Tanimoto, S. Sakai, and H. Mizubayashi, "Mechanical behavior of high-densitynanocrystallinegoldprepared by gasdepositionmethod," *Acta Materialia,* vol. 47, pp. 211-217, 1998.
[69] T.-Y. Kim, J. E. Dolbow, and E. Fried, "Numerical study of grain size dependent young's modulus and poisson's ratio of bulk nano crystalline material," *International Journal of Solids and Structures,* vol. 49, pp. 3942-3952, 2012.
[70] E. Fried and M. E. Gurtin, "Gradient nanoscale polycrystalline elasticity: Intergrain interactions and triple-junction conditions," *Journal of Mechanics and Physics of Solids,* vol. 57, pp. 1749-1779, 2009.
[71] B. A. Movchan and A. V. Demchishin, "Study of the structure and properties of thick vacuum condensates of nickel, titanium, tungsten, aluminium oxide and zirconium dioxide," *Phys. Met. Metallogr,* vol. 28, 1969.
[72] A. A. Anders, "Structure zone diagram including plasma-based deposition and ion etching," *Thin Solid Films,* vol. 518, pp. 4087-4090, 2010.

APPENDICES

Appendix 'A' – Fabrication Procedure

Wafer: SOI

Device Layer	20 +/- 5 um	Polished
Box Layer	2 +/- 1% um	
Handling Layer	600 +/-10um	Polished

Alignment Marks Coords
(X = -3.62; Y = -3.14; Z = 30)

HF Cleaning

Process Step	*Tool*	*Program*	*Parameters*		*Comments*
BHF Cleaning	Acid Bench		6:1 BOE	60 sec	6 Pts 40% NH_4F; 1 Pt 49% HF Acid
QDR	Caustic Bench		5 cycles		
Spin Rinse Dryer	Verteq	Program 1	Resistivity DI water: 15 - 18 MΩ		
Dehydration Bake	Hot Plate		230° C, 5 min		

Specimen Pattern **ENSURE WAFER DEVICE LAYER!!**

Process Step	*Tool*	*Program*	*Parameters*		*Comments*
Spin LOR 3B	CEE Coater	Program 4	500 rpm, 3 sec	5000 rpm, 20 s	Double Dispense with repeater setting 10ml
Soft Bake	Hot Plate		230° C, 5 mins		
Spin AZ 1505	CEE Coater	Program 4	500 rpm, 3 sec	5000 rpm, 20 s	Double Dispense with repeater setting 10ml
Soft Bake	Hot Plate		115° C, 90 s		
Expose	Karl Suss	Vacuum Contact	Mask: Actuator, Exp: 2.5 sec		Intensity: @365nm = 4.5mW/cm2; @405nm = 11.15mW/cm^2; @436nm = 9.16mW/cm^2
Develop	Caustic Bench		3min AZ400K; 4:1		No Agitation (~may be last 30sec)
QDR	Caustic Bench		5 cycles		No sprinklers

Spin Rinse Dryer	Verteq	Program 1	Resistivity DI water: 15 - 18 MΩ	
Descumming	RIE	Program 1	Pwr=100W; time=60s; Gas4(O_2) = 90; Pres = 600	
Inspection	Nikon Microscope			

Specimen Evaporation

Parameters	***Titanium (Ti)*** *(adhesion metal)*	***Platinum (Pt)*** *(Test Metal)*			***Comments***
Density	4.5				
Z-Ratio	0.63				
Tooling Factor	77	77			
Base Pressure	2 x 10^{-6} Torr				
Voltage	10KV	10KV			
Filament Current	0.035	0.111 Amp			
Evap Pressure	1.6 x 10^{-6} Torr	2.6 x 10^{-6} Torr			
Evap Rate	0.4 A/s	~0.6 A/s			
Target Thickness	100 A (10nm)	Variable thk			Test metal thickness range 100-500nm

Specimen Lift Off

Process Step	***Tool***	***Program***	***Parameters***		***Comments***
Acetone soak	Ultrasonic agitation		time	1-2 min	until completely clears out
Methanol Rinse	Solvent bench		5 mins		
IPA Soak	Solvent bench		5 Mins		
QDR	Caustic Bench		5 cycles		
LOR removal	Caustic Bench		60 sec AZ400K (4:1)		until completely clears out
QDR	Caustic Bench		5 cycles		
Spin Rinse Dryer	Verteq	Program 1	Resistivity DI water: 15 - 18 MΩ		

Inspection	Nikon Microscope				
Descumming	RIE	Program 1	Pwr=150W; time=60s; Gas4(O_2) = 90; Pres = 600		OPTIONAL -- if required

Bond pad Pattern

Process Step	***Tool***	***Program***	***Parameters***		***Comments***
Dehydrate Bake	Hot Plate		230^{o} C, 5 mins		
HMDS coat	HMDS Oven	F2	preheat 100^{o}C, 60sec coat		
Spin AZ 9260	CEE Coater	Program 3	150 rpm 2sec	1000 rpm, 60 s	Ensure complete coverage by dispensing access PR
Soft Bake	Hot Plate		120^{o} C, 2min		
Align and Expose	Karl Suss	Hard Contact	Mask: Actuator, Exp: 150 sec		Intensity: @365nm = 4.5mW/cm2; @405nm = 11.15mW/cm^2; @436nm = 9.16mW/cm^2
Develop	Caustic Bench		6min AZ400K; 4:1		with slight agitation for last 2 mins
QDR	Caustic Bench		5 cycles		
Spin Rinse Dryer	Verteq	Program 1	Resistivity DI water: 15 - 18 MΩ		
Inspection	Nikon Microscope				
Descumming	RIE	Program 1	Pwr=100W; time=60s; Gas4(O_2) = 90; Pres = 600		

Bond Pad Evaporation

Parameters	***Aluminum (Al)***	***Chromium (Cr)***	***Gold (Au)***		***Comments***
	(Bond Pad)	*(adhesion metal)*	*(Protection metal)*		
Density	2.7	7.2	19.32		
Z-Ratio	1.05	0.31	0.39		
Tooling Factor	77	77	77		
Base Pressure		2 x 10^{-6} Torr			
Voltage	10KV	10KV	10KV		
Filament Current Evap Pressure	0.120 Amp 1.4 x 10^{-6} Torr	0.015 Amp 2.6 x 10^{-6} Torr	0.068 Amp 2.4 x 10^{-6} Torr		

Evap Rate	~12 A/s	1.5 A/s	0.6 A/s		
Target Thickness	10000A (1000nm)	1500 A (15nm)	1000A (100nm)		

Bond Pad Lift Off

Process Step	***Tool***	***Program***	***Parameters***		***Comments***
Acetone soak	Ultrasonic agitation		time	1-2 min	until completely clears out
Methanol Rinse	Solvent bench		5 mins		
IPA Soak	Solvent bench		5 Mins		
QDR	Caustic Bench		5 cycles		
Inspection	Nikon Microscope				

Actuator Pattern

Process Step	***Tool***	***Program***	***Parameters***		***Comments***
Dehydrate Bake	Hot Plate		230^{o} C, 5 mins		
HMDS coat	HMDS Oven	F2	preheat 100^{o}C, 20sec coat		
Spin AZ1518	CEE Coater	Program 4	150 rpm, 2 sec	1500 rpm, 20 s	Double Dispense with repeater setting 10ml
Soft Bake	Hot Plate		115^{o} C, 90 s		
Align and Expose	Karl Suss	Hard Contact	Mask: Actuator, Exp: 12.5 sec		Intensity: @365nm = 4.5mW/cm2; @405nm = 11.15mW/cm^2; @436nm = 9.16mW/cm^2
Develop	Caustic Bench		3min-30 sec AZ400K; 4:1		with slight agitation
QDR	Caustic Bench		5 cycles		
Spin Rinse Dryer	Verteq	Program 1	Resistivity DI water: 15 - 18 MΩ		
Inspection	Nikon Microscope				

Hard Bake	Hot Plate		115^{o} C, 1 min	

DRIE Etch

Tool	***Parameters***		***Comments***
Adixen AMS 100	Process time	25 min	
(ICP Bosch Process)	He Pressure	10 mbar	
	substrate Posn	200mm	
Program Name	Temperature	10 ^{o}C	
(Std Si 25 min)	Load	660	
Temperature 10	Tune	907	
Delay 30	Source Gen	Checked	
Std Si 25 min	SH gen 2	Checked	
	Passivation	**C_4F_8**	
	Inactive State	0 sec	
	Active State	120 sccm	
	Priority	1	
	Duration	2 sec	
	Pressure	-	
	Posn	-	
	Source G	1800 W	
	SH gen	-	
	H Power	50 W	
	H time	20 msec	
	L Power	0 W	
	L Time	80 msec	
	Etchant	**SF_6**	
	Inactive State	0 sec	
	Active State	300 sccm	
	Priority	2	

	Duration	7 sec	
	Pressure	4.5e-2 mbar	
	Posn	20%	
	Source G	1800 W	
	SH gen	-	
	H Power	-	
	H time	-	
	L Power	-	
	L Time	-	

Photoresis and sidewall passivation removal

Process Step	***Tool***	***Program***	***Parameters***		***Comments***
Ashing	*March Plasma*	*Program 0*	Gas 4 ()	95%	
		Custom	Pressure	600-630 MT	
			Power	275 W	
			End Pt	100	
			Time	600 sec	
			Temp	0	
			BP/RP	80	
Rotate wafer 180^{o} and repeat above					
Soak ACT NE 14	Fumes Hood ME		15 min		For sidewall passivation removal
QDR	Caustic Bench		5 cycles		
Spin Rinse Dryer	Verteq	Program 1	Resistivity DI water: 15 - 18 MΩ		
Inspection	Nikon Microscope				
Dehydrate Bake	Hot Plate		230^{o} C, 5 min		

Specimen Opening Pattern

Process Step	*Tool*	*Program*	*Parameters*		*Comments*
Dehydrate Bake	Hot Plate		120^{o} C, 5 mins		
HMDS coat	HMDS Oven	F2	preheat 100^{o}C, 20sec coat		
Spin AZ 9260	CEE Coater	Program 3	Ramp	100 rpm, 20 s	Ensure complete coverage by dispensing access PR
			Spin Coat	1000 rpm, 90 s	
			EBR	2000 rpm,3 s	
Repeat Spin AZ9260	CEE Coater	Program 3	Same as above		Ensure complete coverage by dispensing access PR
Repeat Spin AZ9260	CEE Coater	Program 3	Same as above		Ensure complete coverage by dispensing access PR
Soft Bake	Hot Plate		75^{o} C, 2min		
			110^{o} C, 2min		
			75^{o} C, 2min		
Rehydrate			30 mins atleast		To avoid cracks and bubbles in the photoresist
Align and Expose	Karl Suss	Hard Contact	Mask: Actuator, Exp: 240 sec		Intensity: @365nm = 4.5mW/cm2; @405nm = 11.15mW/cm^{2}; @436nm = 9.16mW/cm^{2}
Develop	Caustic Bench		4min AZ400K; 4:1		with slight agitation
QDR	Caustic Bench		5 cycles		
Spin Rinse Dryer	Verteq	Program 1	Resistivity DI water: 15 - 18 MΩ		
Inspection	Nikon Microscope				

Dice wafer to obtain individual dies before proceeding

Free Standing Beam Release

Gas	*Parameters*		*Comments*
XeF_2	Temperature	Room Temp.	
	Etch chamber Vac.	0.04 Torr	
	Exp Chamber Pres.	0.25 Torr	
	No. of Pulses	15-Jan	
	Pulse Duration	60 sec	

Photoresist removal

Process Step	*Tool*	*Program*	*Parameters*		*Comments*
Ashing	*March Plasma*	*Program 0 mod*	Gas 2 (CF_4)	0%	No CF_4
			Gas 4 (O_2)	95%	
			Pressure	600-630 mT	Higher pressure is prefferable
			Power	300 W	
			End Pt	100	
			Time	600 sec	
			Temp	0	
			BP/RP	80	
Rotate Wafer 180^o					
Repeat Ashing	*March Plasma*	*Program 0 mod*	Same as above		
Rotate Wafer 180^o					
Repeat Ashing	*March Plasma*	*Program 0 mod*	Same as above		

Vapor HF Release

Process	***Parameters***		***Comments***
Pre-Heat	Rhehostat setting	60%	
	Time	1 Hour	
	Temperature	35 ^{o}C	
Load Wafer			
HF Vapor Etch	Time	6-8 Hours	
Remove Wafer			
Inspection			

PROCESS END

Appendix 'B' – Digital image correlation script

```
close all
clear all
clc

hfw = 0.01544;                          %Probe station Magnification 50x+2x
with 10MPx camera (um/px)
%hfw = 41.6e-3;                         %SEM Horizontal field width (um/px)
%hfw = 250/1020;                        %Probe Station Magnification 10x + 2X
(um/px)
%hfw = 150/1220;                        %Probe Station Magnification 20x + 2X
(um/px)
%hfw = .0325;                           %Probe Station Magnification 50x + 1X
(um/px)with 10MPx camera (um/px)
%hfw = 50/1005;                         %Probe Station Magnification 50x + 2X
(um/px)

k = 2;                          %Number of load cell springs
thk = 400e-9;                   %specimen film thickness (m)
w = 1.48e-6;                       %Specimen width (m)
Area = w*thk;                      %Speciment cross section area in m2
xfree_length = 0;                  %Specimen free length in um along x-
direction
yfree_length = 220;                %Specimen free length in um along y-
direction

yield_strain = 0.008;              %Strain indicating the end of elastic
deformation with zero pre-strain
strain_cleanup = 0.000002;           %Strain value up to which the clean
up of data is required -- typically equal to yield strain
modulus_strain_point = 1;            %No of points to be eliminated for
Young Modulus mean i=modulus_strain point : Length(strain)
Fudge_constant = 1;                %A fudge contant for visual correction
of Modulus scope -- Ideally set to 1
Datum_adjustment_points = 0;       %No. of points from the end of the
strain array to be aligned to zero stress for prestress adjustment
Extrapolated_stress = 400;       %Extrapolated stress in MPa
Pre_stress_strain_switch = 1;        %1 for pre-stress and pre-strain
adjustment -- 0 for no adjustment


%%

%---------------- Digital Image Correlation -------------
tic
% filelist_generator;
% image_handling;           %Digital image corelation
toc
close all
%%

%----- Calculations for single and cascaded actuators -----------------
-

[disp] = displacement2(hfw);              %displacements in um
```

```
[F] = force(k,disp(:,2));            %Determining force from the DIC
displacement data in uN
[strain_eng, yfree_length] = strains(xfree_length, yfree_length);
%Calculating Eng strians
stress_eng = F/Area;           %Calculating Engineering Stress

%[stress_eng,strain_eng]=
cleanup2(stress_eng,strain_eng,strain_cleanup);               %Clean up
the data

%Sample_modulus=140e9;
[Sample_modulus] = Fudge_constant*modulus(yield_strain, stress_eng,
strain_eng,modulus_strain_point)

%%

%--------------Pre stress adjustment ---------------

if Pre_stress_strain_switch == 1
[disp,pre_disp] = prestress_adjustment (disp,Datum_adjustment_points);
pre_force = force(k,pre_disp);
F = F + pre_force;
pre_stress = (pre_force/Area);
stress_eng = stress_eng+pre_stress;

%--------------Pre strain adjustment---------------

pre_strain_max = (stress_eng(modulus_strain_point,1)/Sample_modulus);
strain_eng = strain_eng + pre_strain_max;
disp(:,1)=disp(:,1)+ pre_strain_max*yfree_length;
end

%%
% -------------------- Extrapolated values-----------------------
dummy = 1;
for i = 0:25e6:Extrapolated_stress*1e6
%for i = 0:25e6:stress_eng(1,1)
    pre_stress_plot(dummy,1) = i;
    pre_strain_plot(dummy,1) = i/Sample_modulus;
    dummy=dummy+1;
end

% strain_true = log(1+strain_eng);    %Calculating True Strain
% stress_true = stress_eng.*exp(strain_true);          %Calculating true
stress
%
force_plot = stress_eng * Area;
disp_plot = strain_eng * yfree_length;


% ------------------------Saving Files --------------------
Stress_Strain_data(:,1)=strain_eng;
Stress_Strain_data(:,2)=stress_eng;

save ydisp.dat disp -ascii -tabs
save force.dat F -ascii -tabs
save stress_eng.dat stress_eng -ascii -tabs
```

```
save strain_eng.dat strain_eng -ascii -tabs
save Stress_Strain_data.dat Stress_Strain_data -ascii -tabs
%%
%----------------- Plots ----------------------------------------------
--
%[m,n]=size(disp)
figure (1)
h = zeros(1, 2);
colors =colormap(hsv(2));
for i=1:2
   h(i) = plot (disp(:,i),'Color', colors(i, :), ...
'DisplayName', sprintf('Area %d', i+1));
    hold on
end
legend(h)
title('Displacement in y-direction')
xlabel('Image #'), ylabel('Displacement (\mum)'),
grid, shg


figure (2)
plot (strain_eng, stress_eng*1e-6,'.r')
hold on
plot (pre_strain_plot,pre_stress_plot*1e-6,'-.b')
title('Engineering stress vs Engineering Strain')
ylabel('Engineering Stress (MPa)'), xlabel('Engineering Strain'),
grid, shg


function [FileNameBase,PathNameBase,filenamelist]=filelist_generator

% Code to construct a list of 9999 or less filenames
% This function (Automatic filelist generation by Chris Eberl Last
revision: 12/25/06) has been obtained from Matlab central and used in
conjuction with my script.

filenamelistmode = menu(sprintf('How do you want to create the
filenamelist?'),...
    'Manually','Automatically','Cancel');
if filenamelistmode==3
    return
end
if filenamelistmode==2
    [FileNameBase,PathNameBase,filenamelist]=automatically;
end
if filenamelistmode==1
    [FileNameBase,PathNameBase,filenamelist]=manually;
end

[FileNameBase,PathNameBase,filenamelist]=imagetime(FileNameBase,PathNam
eBase,filenamelist);

%  ------------------------------------------------------

function [Firstimagename,ImageFolder,filenamelist]=automatically

[Firstimagename ImageFolder]=uigetfile('*.tif','Open First Image');
```

```
if Firstimagename~~[];
    cd(ImageFolder);
end

if Firstimagename~~[];
    % Get the number of image name
    letters=isletter(Firstimagename);
    Pointposition=findstr(Firstimagename,'.');
    Firstimagenamesize=size(Firstimagename);
    counter=Pointposition-1;
    counterpos=1;
    letterstest=0;
    while letterstest==0
        letterstest=letters(counter);
        if letterstest==1
            break
        end
        Numberpos(counterpos)=counter;
        counter=counter-1;
        counterpos=counterpos+1;
        if counter==0
            break
        end
    end

    Filename_first = Firstimagename(1:min(Numberpos)-1);
    Firstfilenumber=Firstimagename(min(Numberpos):max(Numberpos));
    Lastname_first                                                    =
Firstimagename(max(Numberpos)+1:Firstimagenamesize(1,2));
    Firstfilenumbersize=size(Firstfilenumber);
    onemore=10^(Firstfilenumbersize(1,2));
    filenamelist(1,:)=Firstimagename;

    Firstfilenumber=str2num(Firstfilenumber);
    u=1+onemore+Firstfilenumber;
    ustr=num2str(u);
    filenamelist(2,:)=[Filename_first
ustr(2:Firstfilenumbersize(1,2)+1) Lastname_first];
    numberofimages=2;

    counter=1;

    while exist(filenamelist((counter+1),:),'file') ==2;
        counter=counter+1;
        u=1+u;
        ustr=num2str(u);
        filenamelist(counter+1,:)=[Filename_first
ustr(2:Firstfilenumbersize(1,2)+1) Lastname_first];
        if exist(filenamelist((counter+1),:),'file') ==0;
            warning('Last image detected')
            filenamelist(counter+1,:)=[];
            break
        end
    end
end
[FileNameBase,PathNameBase]   =   uiputfile('filenamelist.mat','Save   as
"filenamelist" in image directory (recommended)');
```

```
cd(PathNameBase)
save(FileNameBase,'filenamelist');

%  ------------------------------------------------------
function [FileNameBase,PathNameBase,filenamelist]=manually;
% Prompt user for images to be used for analysis

prompt = {'Enter number of first image (i.e. "3" for PIC00003):','Enter
number of last image (i.e. "100" for PIC00100):'};
dlg_title = 'Input images to be used for the analysis';
num_lines= 1;
def     = {'1','100'};
answer = inputdlg(prompt,dlg_title,num_lines,def);
F2 = str2num(cell2mat(answer(1,1)));
F = str2num(cell2mat(answer(2,1)));

if F >= 10000
    error0 = menu('!!! ERROR - Code will only work properly for 9999 or
less picture files !!!','Restart');
    return
end

% Choose first name of images
G = 'PIC1';
prompt = {'Enter Image Name (first 4 letters):'};
dlg_title = 'Input images to be used for the analysis';
num_lines= 1;
def     = {'PIC1'};
answer = inputdlg(prompt,dlg_title,num_lines,def);
G = cell2mat(answer(1,1));

E='.tif';

namelist(1:F-F2+1,1)=G(1,1);
namelist(1:F-F2+1,2)=G(1,2);
namelist(1:F-F2+1,3)=G(1,3);
namelist(1:F-F2+1,4)=G(1,4);

% create the numberlist
num=((10000+F2):(10000+F))';

% Creation of final results
filenamelist=namelist;
str=num2str(num);
filenamelist(:,5:8)=str(:,2:5);

filenamelist(1:F-F2+1,9)=E(1,1);
filenamelist(1:F-F2+1,10)=E(1,2);
filenamelist(1:F-F2+1,11)=E(1,3);
filenamelist(1:F-F2+1,12)=E(1,4);


% Save results
[FileNameBase,PathNameBase]   =   uiputfile('filenamelist.mat','Save   as
"filenamelist" in image directory (recommended)');
cd(PathNameBase)
save(FileNameBase,'filenamelist');
```

```
%  ---------------------------------------
% Extract the time from images?

function
[FileNameBase,PathNameBase,filenamelist]=imagetime(FileNameBase,PathNam
eBase,filenamelist)

selection_time_image = menu(sprintf('Do you also want to extract the
time from images to match stress and strain?'),'Yes','No');

if selection_time_image==1

    % Loop through all images in imagetimelist to get all image capture
times

    [ri,ci]=size(filenamelist);

    o=waitbar(0,'Extracting the image capture times...');

    for q=1:ri

        waitbar(q/ri);
        info=imfinfo(filenamelist(q,:));
        time=datevec(info.FileModDate,13);
        seconds(q)=time(1,4)*3600+time(1,5)*60+time(1,6);

    end

    close(o)

    % Configure and then save image number vs. image capture time text
file

    im_num_im_cap_time=[(1:ri)' seconds'];
    save time_image.txt im_num_im_cap_time -ascii -tabs

end
% End of Chris Eberl's script

function image_handling

% Step 1: Read Image
load filenamelist

base_image = imread(filenamelist(1,:));
figure, imshow(base_image)
hold on
 dummy =0;
 areaindex=0;
 while (dummy~=1)
    hold on
     areaselection = menu(sprintf('Select Area?'),'YES','NO');
   if areaselection ==1
    areaindex=areaindex+1
```

```
    [xrect(areaindex,1),     yrect(areaindex,1),     xrect(areaindex,2),
yrect(areaindex,2)]= mouse_input(base_image)
   end

    if areaselection ==2
      dummy=1;
     break
    end

end


 [m,n]=size(xrect);
 for r=1:1:size(filenamelist)
      for i=1:1:m
      width =xrect(i,2)-xrect(i,1);
      height=yrect(i,2)-yrect(i,1);
     rect_image = [xrect(i,1) yrect(i,1) width height];
     base_subimage = imcrop(base_image,rect_image);
     input_image = imread(filenamelist(r,:));
     [xdata(r,i), ydata(r,i)]=location (input_image,base_subimage);

      end
 r
 end
save xdata.dat xdata -ascii -tabs
save ydata.dat ydata -ascii -tabs
%clear all
%close all


function [xoffset, yoffset]= location(peppers, onion);

%Key concepts:      Normalized cross-correlation, transparency
%Key functions:     normxcorr2, max, ind2sub

% Step 1: Read Images
%onion = imread('onion.png');
%peppers = imread('peppers.png');

%imshow(onion)
%figure, imshow(peppers)

%{
Step 2: Choose Subregions of Each Image
It is important to choose regions that are similar.
The image sub_onion will be the template, and must be smaller than the
image sub_peppers.

      sub_onion=onion;
      sub_peppers=peppers;


%{
Step 3: Do Normalized Cross-Correlation and Find Coordinates of Peak
Calculate the normalized cross-correlation and display it as a surface
plot.
```

```
The peak of the cross-correlation matrix occurs where the sub_images
are best correlated.
normxcorr2 only works on grayscale images, so we pass it the red plane
of each sub image.
    %}

    c = normxcorr2(sub_onion(:,:,1),sub_peppers(:,:,1));
    %figure, surf(c), shading flat


%{
Step 4: Find the Total Offset Between the Images
The total offset or translation between images depends on the location
of the peak in the cross-correlation matrix,
and on the size and position of the sub images.
   %}

    % offset found by correlation
     [max_c, imax] = max(abs(c(:)));
     [ypeak, xpeak] = ind2sub(size(c),imax(1));
     corr_offset = [(xpeak-size(sub_onion,2))
                    (ypeak-size(sub_onion,1))];

      offset = corr_offset;
      xoffset = offset(1);
      yoffset = offset(2);

function [ydisp] = displacement2 (scale)

xdata = load ('xdata.dat');
ydata = load ('ydata.dat');


[m, n]=size(xdata);

for i=1:m
    for j=1:n
        xpos(i,j) = (xdata(i,j)-xdata(i,1));
        ypos(i,j) = (ydata(i,j)-ydata(i,1));
    end
end

for i=1:m
    for j=2:n
        xdisp(i,j-1) = scale*abs(-xpos(i,j)+xpos(1,j));
        ydisp(i,j-1) = scale*(-ypos(i,j)+ypos(1,j));
    end
end

%%
save xdisp.dat xdisp -ascii -tabs
save ydisp.dat ydisp -ascii -tabs

function [F]= force (k, disp)

%k = 1;                              %No. of springs
L = 200;                          %Half Length of Spring in um
```

```
w = 5;                                  %Spring Width in um
h = 20;                                 %Height of structure in um
E = 164e3;                                 %Young's Modulus in MPa
I = (h*w^3)/12;                            %Second Moment of Inertia
A = w*h;                                   %Area of Beam

 [n,m] = size (disp);
for i = 1:n

    if disp(i)<=w/4
    % //--------Linear Deflection Model--------//

    F(i,1) = k*(1e-6*24*E*I/L^3)*disp(i);

% //--------Non Linear Deflection Model--------//
    else
    Const1 = 8*E*I/(L^3);                %Equations from "Flexible bars"
by R. Frisch Fay, 1962
    Const2 = sqrt((2*I)/A);

    %for i=1:1:length(disp)
        f       =       @(z)2*Const2*(z-tanh(z)).*(1.5-0.5*(tanh(z).^2)-
1.5*(tanh(z)./z)).^(-0.5)-disp(i,1);
        u = fzero(f,.5);
    %end

    %u = u';

    F(i,1)    =    1e-6*2*k*Const1*Const2*(u.^3).*(1.5-0.5*(tanh(u).^2)-
1.5*(tanh(u)./u)).^(-0.5);
    %dum2=dum2+1
    end

end

function    [strain_eng,yfree_length]    =    strains    (xfree_length,
yfree_length)
 %xfree_length = 0;
 %yfree_length = 310;

xdisp = load ('xdisp.dat');
ydisp = load ('ydisp.dat');
%gap = load('gap.dat');

%yfree_length = yfree_length - gap(1,1);

[m, n]=size(xdisp);

xdef = abs((xdisp(:,1))- (xdisp(:,2)));
ydef = abs((ydisp(:,1))-(ydisp(:,2)));

for i=1:m
    xstrain(i,1) = (xdef(i,1))/(xfree_length);
    ystrain(i,1) = (ydef(i,1))/(yfree_length);
end
strain_eng = ystrain(:,1);
```

Appendix 'C' – Agilent E3634A power supply control script

```
clear all
close all
clc

newobjs = instrfind;  %Find all previously connected instruments
if (length(newobjs)~=0)
    fclose(newobjs);
    delete(newobjs);
end
% Closes connection to all instruments if any exist.
% This is necessary because there might be an instrument index array,
% and your VISA address won't be valid. For example, the address
according
% to MATLAB would be GPIBx::x::x::INSTR (with a secondary address
included)

max_power = 2;   %Max Power Dissipated as heat and work done on the
actuator
rate = 0.01; %Power (W) increment size
t= 0.5; %defines the wait time before the next increment (sec)
i = 0;    %Dummy index

power_supply = visa('agilent', 'GPIB0::5::INSTR'); %Set variable to
instrument

fopen(power_supply);  %Connect to the instrument
fprintf(power_supply,'*IDN?'); %Query instrument using standard SCPI
commands
IDN = fscanf(power_supply) %Read from instrument, print to command
window

fprintf(power_supply,'OUTput:STATe ON');
%fprintf(power_supply,'VOLTage:RANGe {P50V}');
tic
for p=0:rate:max_power
     i=i+1;
    power_data(i,1)=p;   %Saving simulated power
    fprintf(power_supply,'MEASure:VOLTage:DC?'); %Reading voltage from
instrument
    power_data(i,2) = abs(fscanf(power_supply,'%f'));

    fprintf(power_supply,'MEASure:CURRent:DC?');
    power_data(i,3)=abs(fscanf(power_supply,'%f'));

    power_data(i,4)=(power_data(i,2))*(power_data(i,3));    %Calculating
actual power
    power_data(i,5)        =        (power_data(i,2))/(power_data(i,3));
%Calculating Resistance

    power_data(i,6)      =      sqrt((power_data(i,1))*power_data(i,5));
%Calculating New voltage
    fprintf(power_supply,'VOLT %f', power_data(i,6)); %set new voltage
value using standard SCPI commands
    power_data(i,7)=toc;
```

```
    power_data
    pause(t)
end

fprintf(power_supply,'OUTput:STATe OFF');
fprintf(power_supply,'*RST');
fclose(power_supply); %Disconnect from instrument
delete(power_supply); %Remove instrument from memory
clear power_supply newobjs address %Remove variables from memory



save power_data.dat power_data -ascii -tabs

figure
plot(power_data(:,7),power_data(:,1),power_data(:,7),power_data(:,4))
xlabel('Time (Sec)'), ylabel('Power (W)')
legend ('Simulated Power', 'Actual Power')
grid, shg

figure
plot(power_data(:,4),power_data(:,2))
xlabel('Actual Power (W)'), ylabel('Applied Voltage (V)')
grid, shg

figure
plot(power_data(:,4),power_data(:,3))
xlabel('Actual Power (W)'), ylabel('Applied Current (A)')
grid, shg

figure
plot(power_data(:,4),power_data(:,5))
xlabel('Actual Power (W)'), ylabel('Specimen Resistance (Ohms)')
grid, shg
```